

Modelling Curved and Non-Aligned Surfaces using the  
Finite-Difference Time-Domain Method

Samuel Anthony Bourke

PhD

University of York

Electronic Engineering

December 2018



# Abstract

The finite-difference time-domain (FDTD) method is widely used for computational electromagnetic simulations due to its efficiency and ease of implementation. However, due to its reliance on an orthogonal grid, it is difficult to represent curved and non-aligned planar surfaces. A common method of dealing with this is to use stair-cased meshes that align with the stair-cased grid as close as possible to the surface being meshed. This work explores the errors that arise from using stair-cased meshes of cavities for shielding and scattering problems. It is determined that the increased surface area of a stair-cased mesh alters the transmission and reflection of incident waves.

A method of altering the boundary properties is presented to counteract the errors in transmission and reflection. This method is shown to reduce the error in the magnitude of shielding effectiveness (SE) of stair-cased cavities. However, as this method does not change the geometry of the mesh itself, errors in resonant frequency and the presence of spurious resonances is not affected.

A second method is proposed to locally deform FDTD cells to conform to a curved or non-aligned planar surface. This method incorporates a thin layer model to vastly increase the efficiency of the algorithm when compared to bulk material alternatives. The method is shown to improve errors in the magnitude of SE, resonant frequency and spurious resonances when compared to stair-cased models.



# Contents

<b>Abstract</b>	<b>iii</b>
<b>Contents</b>	<b>v</b>
<b>List of Figures</b>	<b>ix</b>
<b>Acknowledgements</b>	<b>xv</b>
<b>Declaration</b>	<b>xvii</b>
<b>1 Introduction</b>	<b>1</b>
1.1 Computational Electromagnetics . . . . .	1
1.2 Hypothesis . . . . .	2
1.3 Thesis Outline . . . . .	3
<b>2 The Finite-Difference Time-Domain Method</b>	<b>5</b>
2.1 Yee's Algorithm . . . . .	5
2.2 Stability . . . . .	8
2.2.1 Aliasing . . . . .	12
2.3 Conductive Media . . . . .	13
2.3.1 Electric Conductivity . . . . .	13
2.4 Thin Layer Models . . . . .	14
2.4.1 Maloney's Thin Layer Model . . . . .	16
2.4.2 A Face Centered Anisotropic SIBC . . . . .	18
2.4.3 Surface edge updates . . . . .	25
2.5 Summary . . . . .	30
<b>3 Errors due to Stair-casing in FDTD</b>	<b>31</b>
3.1 Known Errors due to Stair-casing Meshing . . . . .	32
3.2 Effect of Stair-casing on Shielding . . . . .	33
3.2.1 Spherical Shell Test Case . . . . .	33

3.2.2	Cubic Shell Test Case . . . . .	39
3.3	Effect of Stair-casing on Scattering . . . . .	42
3.3.1	Cubic Shell Test Case . . . . .	42
3.3.2	Spherical Shell Test Case . . . . .	43
3.4	Summary . . . . .	44
<b>4</b>	<b>Correcting the Transmittance of SIBCs</b>	<b>47</b>
4.1	Stair-casing and Sheet Resistance . . . . .	47
4.2	Proposed Algorithm . . . . .	49
4.3	Validation . . . . .	51
4.3.1	Cubic Shell Test Case . . . . .	51
4.3.2	Cylindrical Shell Test Case . . . . .	55
4.4	Two Axes of Rotation . . . . .	58
4.5	Validation of the Correction Factor Method . . . . .	61
4.5.1	Cubic Shell Test Case . . . . .	61
4.5.2	Spherical Shell Test Case . . . . .	63
4.6	Summary . . . . .	66
<b>5</b>	<b>Conformal Boundaries for FDTD</b>	<b>69</b>
5.1	Conformal Algorithms for PEC Boundaries . . . . .	69
5.1.1	The Dey-Mittra (DM) Method . . . . .	70
5.1.2	Variations on the Dey-Mittra Method . . . . .	73
5.2	A Conformal Algorithm for Bulk Materials . . . . .	74
5.3	A Conformal Thin Layer Model . . . . .	76
5.4	Validation of the Conformal SIBC Algorithm . . . . .	78
5.4.1	Shielding Effectiveness of Cavities . . . . .	78
5.4.2	Scattering from Cavities . . . . .	90
5.4.3	Anisotropic Conformal Boundaries . . . . .	93
5.5	Generating Conformal Meshes . . . . .	94
5.6	Instability due to Highly Deformed Cells . . . . .	96
5.7	Summary . . . . .	99
<b>6</b>	<b>Conclusions and Further Work</b>	<b>101</b>
6.1	Original Contributions . . . . .	101
6.1.1	Corrections to a Face Centred SIBC Algorithm . . . . .	101
6.1.2	Investigations into Stair-cased Cavities . . . . .	101
6.1.3	A Correction Factor for Stair-cased Boundaries . . . . .	102

6.1.4	A Conformal Algorithm Incorporating a Thin Boundary Model . . .	102
6.1.5	Potential Applications . . . . .	102
6.2	Recommendations for Further Work . . . . .	103
6.2.1	Incorporating the Correction Factor Method into the Meshing Process	103
6.2.2	Applying the Correction Factor to Frequency Dependent Media . . .	103
6.2.3	Adapting a Pre-existing Stair-cased Mesher to Produce Conformal Meshes . . . . .	104
<b>Appendix I. List of Abbreviations</b>		<b>105</b>
<b>Bibliography</b>		<b>107</b>



# List of Figures

2.1	Grid structure of the Yee Cell. . . . .	7
2.2	Two sinusoidal waves at 30MHz (red) and 300MHz (blue) that align with the same sampling points (crosses) . . . . .	13
2.3	Cell design of a thin sheet implemented using the Maloney method. Arrows represent discrete electric fields and crosses represent discrete magnetic fields. The thin material sheet is denoted by the dark grey area. . . . .	16
2.4	Axes of face centred SIBC [1]. . . . .	18
2.5	Discrete magnetic fields surrounding SIBC surface. . . . .	20
2.6	Discrete fields surrounding multiple panel SIBC surface. . . . .	22
2.7	Set-up of a 1m radius hollow spherical shell made from a material with a conductivity of 200 S/m that is 5mm thick. The shell is illuminated by a $z$ -polarised plane wave. . . . .	23
2.8	Shielding effectiveness at the centre of the hollow spherical shell with $\sigma = 200\text{S/m}$ and thickness $h = 5$ mm comparing the analytic solution to the different FDTD thin layer methods. . . . .	24
2.9	Skin depth $\delta$ as a function of frequency for the problem set up in Figure 2.7	25
2.10	2D section of an FDTD grid. The $z$ -directed E-field is updated using the surrounding $x$ and $y$ directed magnetic fields. . . . .	26
2.11	2D section of an FDTD grid. The SIBC face (solid black line) calculates the E-field on the each side of the surface. The surrounding magnetic fields should be updated using the average of the two surface E-Fields. . . . .	27
2.12	2D section of an FDTD grid. The SIBC faces (solid black lines) form a corner with the E-field calculated for each side of each surface. The surrounding magnetic fields should be updated using the average of the surface E-Fields for the $b$ sides. . . . .	28
2.13	Shielding effectiveness at the centre of the hollow spherical shell with $\sigma = 200\text{S/m}$ and thickness $h = 5$ mm comparing the analytic solution to the original and edge corrected to the face centred SIBC models. . . . .	29

3.1	Stair-cased meshing of a flat surface (a) rotated $45^\circ$ to the Cartesian grid and a curved surface (b). . . . .	31
3.2	Model of a 1m radius hollow spherical shell made from a material with a conductivity of 1 KS/m that is 1mm thick. The shell is illuminated by a $z$ -polarised plane wave. [1] . . . . .	34
3.3	Shielding effectiveness at centre of a spherical cavity. . . . .	35
3.4	Skin depth $\delta$ as a function of frequency for the problem set up in Figure 3.2	36
3.5	Error in resonant frequencies for a stair-cased shell using different mesh sizes.	36
3.6	Planar E-Field plot for a cross section of the inside of the sphere at 237.6 MHz simulated using CONCEPT II MoM software [2]. . . . .	37
3.7	E-field along 1D across the spherical cavity at 237.6MHz. The unstructured mesh using CONCEPT II MoM software [2] . . . . .	38
3.8	Comparison of the effective surface area of the stair-cased spherical shell and the error in magnitude of SE. . . . .	39
3.9	Set-up of a 1 m hollow cubic shell made from a material with a conductivity of 1 kS/m that is 1 mm thick. The shell is illuminated by a polarised plane wave. . . . .	40
3.10	Coarse (Dot Dashed) and fine (Dashed) stair-cased approximations of a straight line (Solid) . . . . .	41
3.11	Scattering from the cubic cavity, rotated $45^\circ$ with respect to the mesh, in the $yz$ -plane comparing non-conformal and conformal meshes to an aligned cube solution. . . . .	43
3.12	Scattering from the spherical cavity in the $yz$ -plane comparing a stair-cased FDTD simulation to an analytic solution. [3] . . . . .	44
4.1	Geometry used to define sheet resistance. The polarisation of the electric field aligns with the axis of the length $L$ . . . . .	48
4.2	Geometry of sheet resistance for different orientations of stair-cased mesh. .	48
4.3	Set-up of a 1 m hollow cubic shell made from a material with a transmission coefficient of 0.004 and a reflection coefficient of 0.99. The shell is illuminated by a polarised plane wave. This is identical to the mesh shown in Figure 3.9	52
4.4	SE at the centre of a stair-cased cubic shell, with and without a correction factor applied compared to a non stair-cased model. . . . .	53
4.5	Q-factor of first four resonances at the centre of a stair-cased cubic shell, with and without a correction factor applied compared to a non stair-cased model. . . . .	54

4.6	Error in the Q-factor of the first resonance of a stair-cased cubic shell with and without a correction factor applied. Error is relative to a non stair-cased model. . . . .	55
4.7	Diagram of a stair-cased cylindrical shell. Each colour represents a different correction factor that has been applied. . . . .	56
4.8	SE at the centre of a stair-cased cylindrical shell, with and without a correction factor applied compared to an analytic model[3]. . . . .	57
4.9	Close up look at the SE at the centre of a stair-cased cylindrical shell, with and without a correction factor applied compared to an analytic model[3]. . . . .	58
4.10	Diagram of a stair-cased planar material that has been rotated around a single axis. . . . .	59
4.11	Diagram of a stair-cased planar material that has been rotated around two axes. . . . .	60
4.12	Set-up of a 1 m hollow cubic shell made from a material with a transmission coefficient of 0.004 and a reflection coefficient of 0.99. The cube has been rotated $45^\circ$ around the $z$ -axis and $30^\circ$ around the $y$ -axis . . . . .	62
4.13	SE at the centre of a stair-cased cubic shell rotated around two axes with and without a correction factor applied. Comparisons are made with a corrected single axes of rotation stair-cased mesh and a non stair-cased mesh. . . . .	63
4.14	Diagram of a stair-cased spherical shell. Each colour represents a different correction factor that has been applied. . . . .	64
4.15	SE at the centre of a stair-cased spherical shell, with and without a correction factor applied compared to an analytic model[3]. . . . .	65
4.16	Scattering from the spherical cavity in the YZ plane, with and without a correction factor applied, compared to an analytic model[3]. $\Theta$ is the angle of scattering. . . . .	66
5.1	Two-dimensional diagram of non orthogonal object on a cubic grid. Arrows represent the electric fields, crosses represent magnetic fields. . . . .	70
5.2	Single cell of FDTD grid partially filled with PEC object . . . . .	71
5.3	Single cell of FDTD grid partially filled with material object . . . . .	75
5.4	Conformal algorithm applied to a single cell. The shaded surface is not parallel to any cell face. . . . .	77
5.5	Gaussian incident wave in the time domain. . . . .	79
5.6	Gaussian incident wave in the frequency domain. . . . .	79

5.7	1D Resonator Diagram. $E_I$ is the incident electric field and $s$ is the direction of propagation. . . . .	80
5.8	E-Field along 1D Cavity at 37MHz. Comparison of analytic solution with conformal and non-conformal meshes. . . . .	82
5.9	Error in resonant frequency for 1D cavities of different widths. The number of cells across the cavity and the mesh size remain constant. . . . .	83
5.10	Stair-cased mesh of cubic shell for FDTD using 100mm grid. PML boundaries are used to terminate the edges of the problem space. The scattering angle $\Theta$ is shown corresponding to Figure 5.17. . . . .	84
5.11	Shielding effectiveness at the centre of a cubic shell rotated $45^\circ$ with respect to the FDTD grid. Comparisons are made with an aligned case. . . . .	85
5.12	Shielding effectiveness at the first resonant frequency of the cubic cavity. . .	86
5.13	Stair-cased mesh of an infinite cylinder for FDTD. Only one layer of cells is required in the $z$ -direction, PMC boundaries emulate an infinite length. .	87
5.14	Shielding effectiveness at the centre of the cylindrical cavity comparing non-conformal and conformal meshes to an analytic solution. . . . .	88
5.15	Example of a stair-cased mesh of a sphere adapted to the conformal algorithm.	89
5.16	Shielding at the centre of the spherical cavity comparing non-conformal and conformal meshes to an analytic solution. . . . .	90
5.17	Scattering from the cubic cavity, rotated $45^\circ$ with respect to the mesh, in the $yz$ -plane comparing non-conformal and conformal meshes to an aligned cube solution. . . . .	92
5.18	Scattering from the spherical cavity in the $yz$ -plane comparing non-conformal and conformal meshes to an analytic solution. . . . .	93
5.19	Shielding effectiveness at the centre of cubic mesh at 100MHz for different E-field polarisations comparing non-conformal and conformal meshes to an aligned mesh. 0 degrees corresponds to a $z$ -polarised E-Field. . . . .	94
5.20	Adaptation of a stair-cased mesh to the conformal algorithm for a single cell.	95
5.21	Adaptation of a stair-cased curve to the conformal algorithm. . . . .	95
5.22	Adaptation of a stair-cased arbitrary surface to the conformal algorithm. . .	96
5.23	3 FDTD cells with SIBC faces, $l_1$ , $l_2$ and $l_3$ are the deformed cell widths with values of $\Delta$ , $0.5\Delta$ and $0.025\Delta$ respectively. . . . .	97
5.24	Conformal algorithm applied to a single cell. The shaded surface violates the 'forbidden zones' that could lead to instability. . . . .	98

5.25 Conformal algorithm applied to a single cell. The shaded surface has been moved so that it no longer violates the 'forbidden zones' to avoid potential instability. . . . . 99



# Acknowledgements

I wish to express my gratitude to my supervisors John Dawson and Martin Robinson for providing me guidance throughout my PhD. I would like to thank Ian Flintoft whose work on the Vulture FDTD software provided a basis for my own work and Stuart Porter, for his advice. I would also like to acknowledge the EPSRC whose funding allowed me to pursue my studies.

Finally, I must thank my wife, Jenny, without whom I would never have done a PhD in the first place.



# Declaration

All work presented in this thesis is original to the best knowledge of the author. References to other researchers have been given as appropriate. This work has not previously been presented for an award at this or any other institution. Some parts of this thesis have been published in journals and conference proceedings; where items were published jointly with collaborators, the author of this thesis is responsible for the material presented here. For each published item the primary author is the first listed author.

## List of Publications

- S. A. Bourke, J. F. Dawson, I. D. Flintoft and M. P. Robinson, “Errors in the shielding effectiveness of cavities due to stair-cased meshing in FDTD: Application of empirical correction factors,” 2017 International Symposium on Electromagnetic Compatibility - EMC EUROPE, Angers, 2017, pp. 1-6.
- I. D. Flintoft, S. A. Bourke, J. F. Dawson, J. Alvarez, M. R. Cabello, M. P. Robinson and S. G. Garcia, “Face-Centered Anisotropic Surface Impedance Boundary Conditions in FDTD,” in IEEE Transactions on Microwave Theory and Techniques, vol. 66, no. 2, pp. 643-650, Feb. 2018.
  - Generation and simulation of spherical mesh problems, substantial contribution to results and conclusion sections.
- M. R. Cabello, L. Diaz Angulo, J. Alvarez, I. D. Flintoft, S. Bourke, J. F. Dawson, R. Gómez Martín, S. G. Garcia, “A Hybrid Crank–Nicolson FDTD Subgridding Boundary Condition for Lossy Thin-Layer Modeling,” in IEEE Transactions on Microwave Theory and Techniques, vol. 65, no. 5, pp. 1397-1406, May 2017.
  - Comparative models using the face-centred thin boundary model presented in this thesis.
- J. F. Dawson, I. D. Flintoft, S. A. Bourke, M. P. Robinson, M. R. Cabello and S. G. Garcia; J. Alvarez, “Face centered anisotropic surface impedance boundary

conditions in FDTD: Improved performance of staircased mesh for shielding problems,” 2017 IEEE MTT-S International Conference on Numerical Electromagnetic and Multiphysics Modeling and Optimization for RF, Microwave, and Terahertz Applications (NEMO), Seville, 2017, pp. 260-262.

- S. Bourke, J. Dawson, M. Robinson and S. Porter, “A Conformal Thin Boundary Model for FDTD,” 2018 IEEE MTT-S International Conference on Numerical Electromagnetic and Multiphysics Modeling and Optimization (NEMO), Reykjavik, Iceland, 2018, pp. 1-4
- S. A. Bourke, J. F. Dawson, M. P. Robinson, S. J. Porter, “A Conformal Anisotropic Thin Boundary Model for the Finite-Difference Time-Domain Method” in IEEE Transactions on Microwave Theory and Techniques (Under Review)

# Chapter 1

## Introduction

This chapter will lay out the motivation for the work carried out for this thesis by describing the role of computational electromagnetics in modern industry and the need for accurate and computationally efficient simulation techniques. The hypothesis underlying this thesis is presented and a breakdown of the thesis structure is given.

### 1.1 Computational Electromagnetics

Computational electromagnetics (CEM) deals with numerical solutions to electromagnetic problems. This is an important field of study for a number of reasons. Firstly it is possible to get closed form analytical solutions only for very simple problems, for most real world applications the model must be solved using numerical methods. CEM also allows for rapid development of models, this is quicker, cheaper and less wasteful than using physical models during the early design process. CEM is used in a wide range of applications, including, but not limited to, the design and study of antennas, electronic components and medical imaging. Most significantly for this work, CEM is used for electromagnetic shielding problems of cavities, this can be applied to models such as vehicles, buildings and equipment casing. Further to shield scattering is also of interest in such cases.

There are numerous CEM techniques available, each with their own benefits and drawbacks. This work will focus on a time domain method. Time domain methods work by iterating a system state over time for a pre-defined geometry using an initial electromagnetic pulse. This allows a broad range of frequencies to be simulated simultaneously, the frequency data can be extracted from the time response by the use of Fourier transforms.

On the other hand, frequency domain methods, such as the Method of Moments (MoM), solve a problem for a single frequency for each simulation, this assumes a static state with respect to time. The advantage of using MoM is that it can be used to model fine featured elements without needing to simulate all of the intervening space, this means that

the MoM technique can be much faster for some problems. However modelling dispersive materials is easier in time domain methods as they can consider multiple frequencies at once.

This work will discuss the Finite-Difference Time-Domain (FDTD) method. As a time domain method, FDTD is good for broadband simulations and is comparatively easy to implement. The technique has been developed for over 50 years, making it a very mature method with a large background of literature and techniques to improve various aspects. The method utilises a cuboid grid of nodes that record the magnitude of the electromagnetic field at discrete points.

An important aspect of developing numerical tools is keeping the solution efficient. As computing power increases, more complex systems can be modelled, however an inefficient algorithm design can still be extremely costly and make such simulations time consuming, sometimes impractically so.

Current work of FDTD often focuses on developing techniques to model structures, such as joints and perforated sheets, without having to generate models with highly resolved detail, in order to maintain efficiency. The challenge is to create techniques that maintain the accuracy of a highly detailed model, the efficiency of a coarsely detailed model and to maintain the stability of the underlying algorithm.

An example of this type of work is thin layer models. These are tools used to represent materials that are much thinner than the spacing between node on the FDTD grid. Thin layer models are useful as they can decrease the amount of computation that is required to solve a given model.

A common use of CEM is modelling vehicles in electromagnetic environments. Such simulations require the modelling of curved surfaces, like the fuselage of an aircraft. Unfortunately the FDTD method utilises a cuboid mesh, this makes it difficult to represent surfaces that do not align with the mesh and often results in an approximation of the surface using an orthogonal or 'stair-cased' mesh. This report will discuss the various errors introduced by inaccurate representations of models due to orthogonal meshing and suggest methods that can be used to improve the accuracy of those models.

## 1.2 Hypothesis

The work presented in this thesis is guided by the hypothesis:

*“The errors that result from stair-cased meshing of curved and non-aligned surfaces for FDTD can be reduced by correcting for the difference between the stair-cased surface and the surface being modelled.”*

### 1.3 Thesis Outline

Chapter 2 introduces the Finite-Difference Time-Domain method, including the underlying Yee cell algorithm, stability conditions, electric and magnetic conductive media. It then introduces the concept of thin layer models to represent thin material sheets in an efficient manner. A widely popular edge centred thin layer model is presented followed by a more recent face centred model including improvements implemented by the author. Validation for the face centred model is provided, including increases in accuracy due to the implemented improvements.

Chapter 3 describes the stair-cased meshing of curved and non-aligned surfaces to conform to the orthogonal FDTD grid. There is a discussion of pre-existing work covering errors caused by stair-cased meshing for 2D planar and curved surfaces. The limits of existing work is identified and the rest of the chapter presents novel work focusing primarily on the effect of stair-casing on the electromagnetic shielding of cavities. Errors in resonant frequencies, shielding magnitude and the appearance of spurious resonances are identified.

Chapter 4 posits that the increase in length of a surface due to stair-casing increases or decreases the sheet resistance of the conductive boundary proportionally to the change in length subsequently affecting the transmission and reflection coefficients of the boundary. A new method of reducing the errors in transmission and reflection from stair-cased boundaries by altering the transmission and reflection coefficients of the boundary is presented and validated using a variety of shielding and scattering problems for cavities.

Chapter 5 describes a number of pre-existing conformal mesh algorithms based on the Dey-Mitra (DM) method to deform the FDTD mesh to better represent curved and non-aligned surfaces. A new conformal algorithm is proposed that incorporates the face centred thin boundary model to combine the efficiency of a thin boundary model with the accuracy of a conformal model. The new algorithm is validated using multiple test cases measuring the shielding and scattering of different cavity models.

Chapter 6 lists the novel contributions made in this thesis. Suggestions for further work are then made focusing on making the methods presented usable for complex problems by automating the meshing process to incorporate either the correction factor from Chapter 4 or the conformal algorithm from Chapter 5.



## Chapter 2

# The Finite-Difference Time-Domain Method

The Finite-Difference Time-Domain method is a numerical analysis technique that has been developed over the past 50 years to solve electromagnetic problems, there are some applications in other fields, for example acoustics has similar physical principles that allows the FDTD method to be used [4]. The method is a time domain technique, allowing a broad range of frequencies to be simulated at the same time, unlike frequency domain solvers. As computational algorithms have been developed the capacity to model more advanced materials and more complex structures has improved. This chapter introduces the Finite-Difference Time-Domain method by deriving the underlying Yee algorithms from Maxwell's equations. The stability of the algorithm is discussed, including consideration of Aliasing. A popular existing method for modelling bulk conductive materials is presented [5–7]. Two thin layer models are described, the first is the widely utilised edge centred Maloney model [8]. The second is a face-centred model[1] developed at the University of York, including validation results and edge corrections by the author.

### 2.1 Yee's Algorithm

The FDTD method can be derived from Maxwell's equations. The scheme, developed by Kane Yee in 1966, utilises a staggered grid to discretise the electric and magnetic fields in space [9]. The E and H fields are updated at alternate discrete steps in time.

Maxwell's equations are used to describe the nature of electric and magnetic fields and can be used to determine how they propagate. Two of these laws are Faraday's Law and Ampere's Law. Shown here are their differential forms in free space:

$$\frac{\partial \mathbf{B}}{\partial t} = -\nabla \times \mathbf{E} \quad (2.1)$$

$$\frac{\partial \mathbf{D}}{\partial t} = \nabla \times \mathbf{H} \quad (2.2)$$

Where  $\mathbf{B}$  is the magnetic flux density,  $\mathbf{D}$  is the electric flux density,  $\mathbf{E}$  is the electric field intensity and  $\mathbf{H}$  is the magnetic field intensity. These are related by:

$$\mathbf{D} = \epsilon_0 \epsilon_r \mathbf{E} = \epsilon \mathbf{E} \quad (2.3)$$

$$\mathbf{B} = \mu_0 \mu_r \mathbf{H} = \mu \mathbf{H} \quad (2.4)$$

Where  $\mu_0$  is the permeability of free space,  $\mu_r$  is the relative permeability,  $\epsilon_0$  is the permittivity of free space,  $\epsilon_r$  is the relative permittivity.  $\mu$  and  $\epsilon$  are the permittivity and permeability of the medium respectively.

Considering the magnetic field only in the  $x$  direction and substituting (2.3) into (2.1), Faraday's law can be written as:

$$\mu \frac{\partial H_x}{\partial t} = \frac{\partial E_y}{\partial z} - \frac{\partial E_z}{\partial y} \quad (2.5)$$

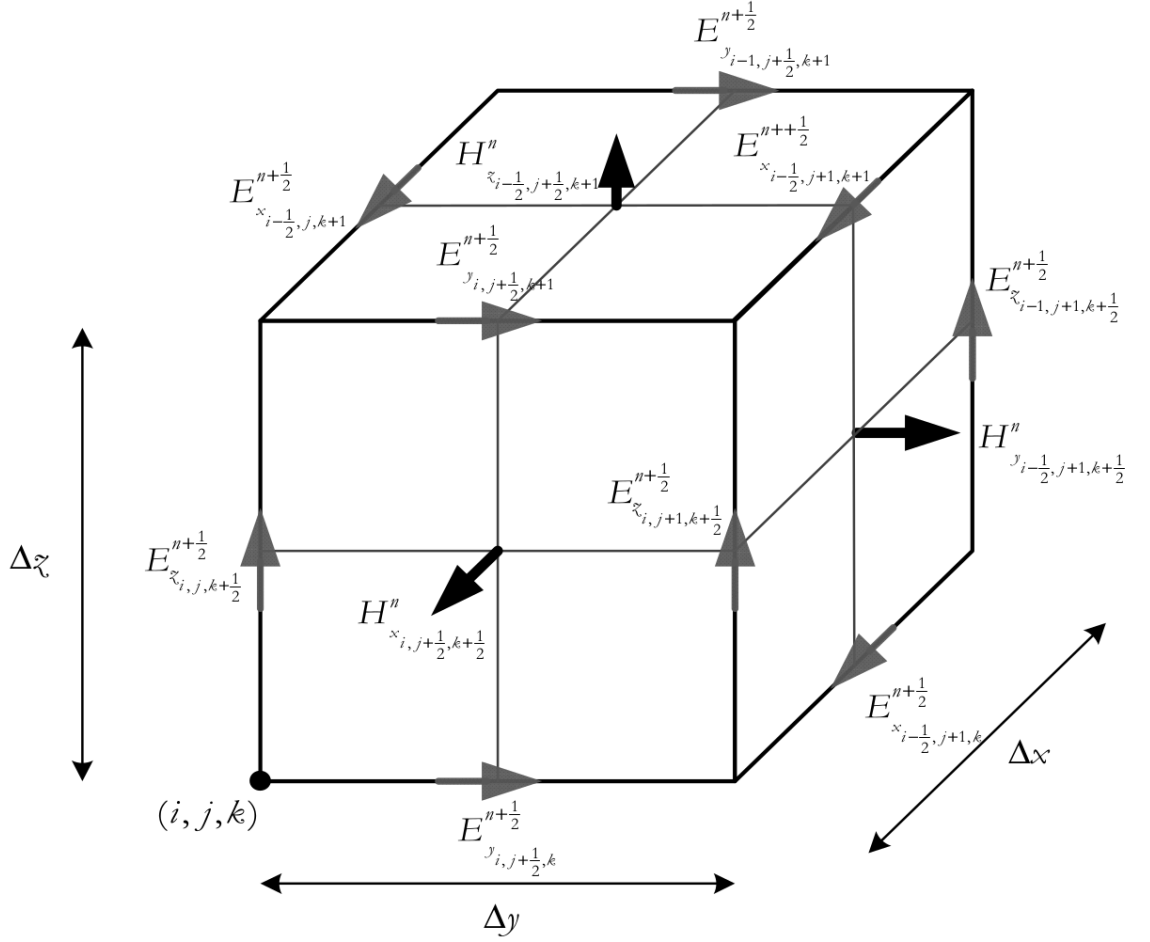


Figure 2.1: Grid structure of the Yee Cell [6]

The Yee cell in Figure 2.1 shows how the electric and magnetic fields are positioned at discrete uniformly spaced points.

Using the discrete electric and magnetic fields (2.5) can be rewritten as:

$$\mu \left( \frac{H_{x_{i,j+\frac{1}{2},k+\frac{1}{2}}}^{n+1} - H_{x_{i,j+\frac{1}{2},k+\frac{1}{2}}}^n}{\Delta t} \right) = \left( \frac{E_{y_{i,j+\frac{1}{2},k+1}}^{n+\frac{1}{2}} - E_{y_{i,j+\frac{1}{2},k}}^{n+\frac{1}{2}}}{\Delta z} \right) - \left( \frac{E_{z_{i,j+1,k+\frac{1}{2}}}^{n+\frac{1}{2}} - E_{z_{i,j,k+\frac{1}{2}}}^{n+\frac{1}{2}}}{\Delta y} \right) \quad (2.6)$$

It can be seen that where the magnetic field is differentiated in *time* in the left hand term, the electric fields are differentiated in *space* in the right hand term. A similar equation can be derived for the electric field by considering (2.2), again in the x direction:

$$\varepsilon \frac{\partial E_x}{\partial t} = \frac{\partial H_z}{\partial y} - \frac{\partial H_y}{\partial z} \quad (2.7)$$

$$\varepsilon \left( \frac{E_{x_{i+\frac{1}{2},j,k+1}}^{n+\frac{1}{2}} - E_{x_{i+\frac{1}{2},j,k+1}}^{n-\frac{1}{2}}}{\Delta t} \right) = \left( \frac{H_{z_{i+\frac{1}{2},j+\frac{1}{2},k}}^n - H_{z_{i+\frac{1}{2},j-\frac{1}{2},k}}^n}{\Delta y} \right) - \left( \frac{H_{y_{i+\frac{1}{2},j,k+\frac{1}{2}}}^n - H_{y_{i+\frac{1}{2},j,k-\frac{1}{2}}}^n}{\Delta z} \right) \quad (2.8)$$

Equations (2.6) and( 2.8) can be rearranged to give the field update equations:

$$H_{x_{i,j+\frac{1}{2},k+\frac{1}{2}}}^{n+1} = H_{x_{i,j+\frac{1}{2},k+\frac{1}{2}}}^n + \frac{\Delta t}{\mu} \left[ \left( \frac{E_{y_{i,j+\frac{1}{2},k+1}}^{n+\frac{1}{2}} - E_{y_{i,j+\frac{1}{2},k}}^{n+\frac{1}{2}}}{\Delta z} \right) - \left( \frac{E_{z_{i,j+1,k+\frac{1}{2}}}^{n+\frac{1}{2}} - E_{z_{i,j,k+\frac{1}{2}}}^{n+\frac{1}{2}}}{\Delta y} \right) \right] \quad (2.9)$$

$$E_{x_{i+\frac{1}{2},j,k}}^{n+\frac{1}{2}} = E_{x_{i+\frac{1}{2},j,k}}^{n-\frac{1}{2}} + \frac{\Delta t}{\varepsilon} \left[ \left( \frac{H_{z_{i+\frac{1}{2},j+\frac{1}{2},k}}^n - H_{z_{i+\frac{1}{2},j-\frac{1}{2},k}}^n}{\Delta y} \right) - \left( \frac{H_{y_{i+\frac{1}{2},j,k+\frac{1}{2}}}^n - H_{y_{i+\frac{1}{2},j,k-\frac{1}{2}}}^n}{\Delta z} \right) \right] \quad (2.10)$$

The update equations for  $H_y$ ,  $H_z$ ,  $E_y$  and  $E_z$  can be derived in a similar fashion and are given here [10]:

$$H_{y_{i+\frac{1}{2},j,k+\frac{1}{2}}}^{n+1} = H_{y_{i+\frac{1}{2},j,k+\frac{1}{2}}}^n + \frac{\Delta t}{\mu} \left[ \left( \frac{E_{z_{i,j,k+\frac{1}{2}}}^{n+\frac{1}{2}} - E_{z_{i+1,j,k+\frac{1}{2}}}^{n+\frac{1}{2}}}{\Delta x} \right) - \left( \frac{E_{x_{i+\frac{1}{2},j,k}}^{n+\frac{1}{2}} - E_{x_{i+\frac{1}{2},j,k+1}}^{n+\frac{1}{2}}}{\Delta z} \right) \right] \quad (2.11)$$

$$H_{z_{i+\frac{1}{2},j+\frac{1}{2},k}}^{n+1} = H_{z_{i+\frac{1}{2},j+\frac{1}{2},k}}^n + \frac{\Delta t}{\mu} \left[ \left( \frac{E_{x_{i+\frac{1}{2},j+1,k}}^{n+\frac{1}{2}} - E_{x_{i+\frac{1}{2},j,k}}^{n+\frac{1}{2}}}{\Delta y} \right) - \left( \frac{E_{y_{i+1,j+\frac{1}{2},j+1,k}}^{n+\frac{1}{2}} - E_{y_{i,j+\frac{1}{2},j+1,k}}^{n+\frac{1}{2}}}{\Delta x} \right) \right] \quad (2.12)$$

$$E_{y_{i,j+\frac{1}{2},k}}^{n+\frac{1}{2}} = E_{y_{i,j+\frac{1}{2},k}}^{n-\frac{1}{2}} + \frac{\Delta t}{\varepsilon} \left[ \left( \frac{H_{x_{i,j+\frac{1}{2},k+\frac{1}{2}}}^n - H_{x_{i,j+\frac{1}{2},k-\frac{1}{2}}}^n}{\Delta z} \right) - \left( \frac{H_{z_{i+\frac{1}{2},j+\frac{1}{2},k}}^n - H_{z_{i-\frac{1}{2},j+\frac{1}{2},k}}^n}{\Delta x} \right) \right] \quad (2.13)$$

$$E_{z_{i,j,k+\frac{1}{2}}}^{n+\frac{1}{2}} = E_{z_{i,j,k+\frac{1}{2}}}^{n-\frac{1}{2}} + \frac{\Delta t}{\varepsilon} \left[ \left( \frac{H_{y_{i+\frac{1}{2},j,k+\frac{1}{2}}}^n - H_{y_{i-\frac{1}{2},j,k+\frac{1}{2}}}^n}{\Delta x} \right) - \left( \frac{H_{x_{i,j+\frac{1}{2},k+\frac{1}{2}}}^n - H_{x_{i,j-\frac{1}{2},k+\frac{1}{2}}}^n}{\Delta y} \right) \right] \quad (2.14)$$

It is often the case the update coefficients  $\frac{\Delta t}{\varepsilon}$  and  $\frac{\Delta t}{\mu}$  for a specific node are represented using the shorthand:

$$C_{i,j,k}^{hx} \quad (2.15)$$

where  $i,j,k$  represent the coordinates of the node and  $hx$  indicates a  $x$ -directed magnetic field, the notations  $hy,hz,ex,ey,ez$  would be used for other field components.

## 2.2 Stability

The FDTD algorithm is required to fulfil some stability restrictions to operate correctly. The system can be considered stable if the energy input into the system is bounded. That

is to say there can only be a finite amount of energy in the system. The maximum time step that can be chosen for a given space step is determined by the Courant-Fredrichs-Lewy (CFL) stability limit [11]. The previously derived update equations (2.9 - 2.14) can be expressed as a system of linear equations:

$$\mathbf{h}^n = \mathbf{h}^{n-1} - \Delta t \mu^{-1} \mathbf{C}_e \mathbf{e}^{n-\frac{1}{2}} \quad (2.16)$$

$$\mathbf{e}^{n+\frac{1}{2}} = \mathbf{e}^{n-\frac{1}{2}} - \Delta t \varepsilon^{-1} \mathbf{C}_h \mathbf{h}^n \quad (2.17)$$

Where  $\mathbf{h}$  is the vector of all discrete magnetic fields and  $\mathbf{e}$  is the vector of all discrete electric fields.  $\mathbf{C}_e$  and  $\mathbf{C}_h$  are matrices representing the curl of the electric and magnetic fields respectively. Substituting (2.16) into (2.17) gives a single first order difference equation:

$$\mathbf{e}^{n+\frac{1}{2}} = \mathbf{e}^{n-\frac{1}{2}} + \Delta t \varepsilon^{-1} \mathbf{C}_h \mathbf{h}^{n-1} - \Delta t^2 \mu^{-1} \varepsilon^{-1} \mathbf{C}_h \mathbf{C}_e \mathbf{e}^{n-\frac{1}{2}} \quad (2.18)$$

Combining (2.16) and (2.18) gives:

$$\begin{bmatrix} \mathbf{h}^n \\ \mathbf{e}^{n+\frac{1}{2}} \end{bmatrix} = \begin{bmatrix} \mathbf{I} & -\Delta t \mu^{-1} \mathbf{C}_e \\ \Delta t \varepsilon^{-1} \mathbf{C}_h & \mathbf{I} - \Delta t^2 \mu^{-1} \varepsilon^{-1} \mathbf{C}_h \mathbf{C}_e \end{bmatrix} \begin{bmatrix} \mathbf{h}^{n-1} \\ \mathbf{e}^{n-\frac{1}{2}} \end{bmatrix} \quad (2.19)$$

This can be written in the simpler form[12]:

$$\mathbf{w}^n = \mathbf{G} \mathbf{w}^{n-1} \quad (2.20)$$

Where:

$$\mathbf{w}^n = \begin{bmatrix} \mathbf{h}^n \\ \mathbf{e}^{n+\frac{1}{2}} \end{bmatrix}, \quad \mathbf{G} = \begin{bmatrix} \mathbf{I} & -\Delta t \mu^{-1} \mathbf{C}_e \\ \Delta t \varepsilon^{-1} \mathbf{C}_h & \mathbf{I} - \Delta t^2 c^2 \mathbf{C}_h \mathbf{C}_e \end{bmatrix} \quad (2.21)$$

Where  $c$  is the speed of light. If the initial state of the system is given by  $\mathbf{w}^0$  then the system at time step  $n$  can be given by:

$$\mathbf{w}^n = \mathbf{G}^n \mathbf{w}^0 \quad (2.22)$$

For (2.22) to be stable it must satisfy this condition:

$$\lim_{n \rightarrow \infty} \frac{|\mathbf{w}^n|}{|\mathbf{w}^0|} \leq C \quad (2.23)$$

Where  $C$  represents a finite constant.

For (2.23) to be fulfilled the eigenvalues of  $\mathbf{G}$  must lie on or within the unit circle of the complex plane so that the magnitude is less than or equal to 1. A magnitude greater than 1 would cause (2.23) to be infinite. The eigenvalues of  $\mathbf{G}$  can be determined by [13]:

$$\mathbf{G}\mathbf{x} = \lambda_G\mathbf{x} \quad (2.24)$$

Where  $\mathbf{x}$  represents the eigenvectors of  $\mathbf{G}$ . The eigenvalues are shifted by:

$$(\mathbf{G} - \mathbf{I})\mathbf{x} = (\lambda_G - 1)\mathbf{x} \mapsto \tilde{\mathbf{G}}\mathbf{x} = \xi\mathbf{x} \quad (2.25)$$

Where  $\xi = \lambda_G - 1$ . Written out fully this is:

$$\begin{bmatrix} 0 & -\Delta t\mu^{-1}\mathbf{C}_e \\ \Delta t\varepsilon^{-1}\mathbf{C}_h & -c^2\Delta t^2\mathbf{C}_e\mathbf{C}_h \end{bmatrix} \begin{bmatrix} \mathbf{x}_1 \\ \mathbf{x}_2 \end{bmatrix} = \xi \begin{bmatrix} \mathbf{x}_1 \\ \mathbf{x}_2 \end{bmatrix} \quad (2.26)$$

The top row from (2.26) is multiplied by  $\Delta t\varepsilon^{-1}\mathbf{C}_h$  giving:

$$-\Delta t^2\mu^{-1}\varepsilon^{-1}\mathbf{C}_h\mathbf{C}_e\mathbf{x}_2 = \xi\Delta t\varepsilon^{-1}\mathbf{C}_h\mathbf{x}_1 \quad (2.27)$$

Substituting 2.27 into the bottom row of 2.26 gives:

$$(\xi^2 + \xi c^2\Delta t^2\mathbf{M} + c^2\Delta t^2\mathbf{M})\mathbf{x}_2 = 0 \quad (2.28)$$

Where  $\mathbf{M}$  is the discrete curl-curl operator:

$$\mathbf{M} = \mathbf{C}_h\mathbf{C}_e \quad (2.29)$$

$\mathbf{M}$  is positive definite and therefore can be diagonalised using a projection matrix  $\mathbf{P}$  such that:

$$\mathbf{P}^{-1}\mathbf{M}\mathbf{P} = \mathbf{D}_m \quad (2.30)$$

Where  $\mathbf{D}_m$  is a diagonal matrix containing the eigenvalues of  $\mathbf{M}$ . Applying (2.30) to 2.28 gives:

$$\mathbf{P}^{-1}(\xi^2 + \xi c^2\Delta t^2\mathbf{M} + c^2\Delta t^2\mathbf{M})\mathbf{P}\mathbf{x}_2 = 0 \quad (2.31)$$

$$(\mathbf{I}\xi^2 + \xi c^2\Delta t^2\mathbf{D}_m + c^2\Delta t^2\mathbf{D}_m)\mathbf{x}_2 = 0 \quad (2.32)$$

For (2.32) to be true then:

$$\xi^2 + \xi c^2\Delta t^2\lambda_m + c^2\Delta t^2\lambda_m = 0 \quad (2.33)$$

Where  $\lambda_m$  represents the eigenvalues of  $\mathbf{M}$ . Rearranging to get  $\xi$  gives:

$$\xi = -\frac{c^2 \Delta t^2}{2} \lambda_m \pm \sqrt{\left(\frac{c^2 \Delta t^2 \lambda_m}{2}\right)^2 - 2\left(\frac{c^2 \Delta t^2 \lambda_m}{2}\right)} \quad (2.34)$$

As noted previously  $\xi = \lambda_G - 1$ , so the eigenvalues of  $\mathbf{G}$  can be given by:

$$\lambda_G = 1 - \frac{c^2 \Delta t^2}{2} \lambda_m \pm \sqrt{\left(\frac{c^2 \Delta t^2 \lambda_m}{2}\right)^2 - 2\left(\frac{c^2 \Delta t^2 \lambda_m}{2}\right)} \quad (2.35)$$

From (2.23) it is known that  $|\lambda_m| \leq 1$  which can only be true if  $\lambda_m$  are real and distinct. It must also be true that:

$$\frac{c^2 \Delta t^2 \lambda_m}{2} \geq 2 \quad (2.36)$$

It can be shown that:

$$\lambda_m \leq 4\left(\frac{1}{\Delta x^2} + \frac{1}{\Delta y^2} + \frac{1}{\Delta z^2}\right) \quad (2.37)$$

Applying (2.37) to (2.36) gives:

$$\Delta t \leq \frac{1}{c} \frac{1}{\sqrt{\frac{1}{\Delta x^2} + \frac{1}{\Delta y^2} + \frac{1}{\Delta z^2}}} \quad (2.38)$$

This is the analytical stability condition for the time step of the FDTD algorithm. However in the case that (2.38) is an equality the possibility of rounding errors within the simulation could cause  $\Delta t$  to be greater than the stability limit. As such the CFL limit is given as:

$$\Delta t < \frac{1}{c} \frac{1}{\sqrt{\frac{1}{\Delta x^2} + \frac{1}{\Delta y^2} + \frac{1}{\Delta z^2}}} \quad (2.39)$$

In the case that the media is inhomogeneous and therefore there are multiple values of  $c$  the highest wave speed is used. Thus, the general solution for determining the time step is given by:

$$\Delta t = \frac{1}{c_{max}} \frac{CFLN}{\sqrt{\frac{1}{\Delta x^2} + \frac{1}{\Delta y^2} + \frac{1}{\Delta z^2}}} \quad (2.40)$$

Where CFLN is the Courant-Fredrichs-Lewy number. From (2.39) it is known that this must be less than 1. To maximise the time step a number as close to one as possible (e.g. 0.99) is usually chosen.

In the case of a cubic grid, that is to say:

$$\Delta x = \Delta y = \Delta z = \Delta \quad (2.41)$$

The stability criteria can be simplified to give a time step of:

$$\Delta t = \frac{\Delta}{c_{max}} \frac{CFLN}{\sqrt{3}} \quad (2.42)$$

### 2.2.1 Aliasing

When selecting a spatial grid size for a FDTD simulation it is necessary to consider the range of frequencies that will be used in the simulation. To accurately represent a wave of a given frequency there must be a suitable number of sample points across its wavelength. [5].

Consider the sinusoidal waves in Figure 2.2. If the 300 MHz wave is sampled at 1 meter intervals it cannot be distinguished from the 30 MHz wave sampled at the same intervals as the magnitude of each wave at the sample points is identical. This is called *aliasing*. Aliasing creates a limit on the frequency of electromagnetic wave that can be represented. A common rule of thumb is to have at least 10 sample points per wavelength. As the spacing between sample points is determined by the FDTD grid, this limits the maximum useable frequency to:

$$f = \frac{c}{10\Delta} \quad (2.43)$$

Where  $f$  is the frequency,  $c$  is the speed of light and  $\Delta$  is the spacing between FDTD field nodes.

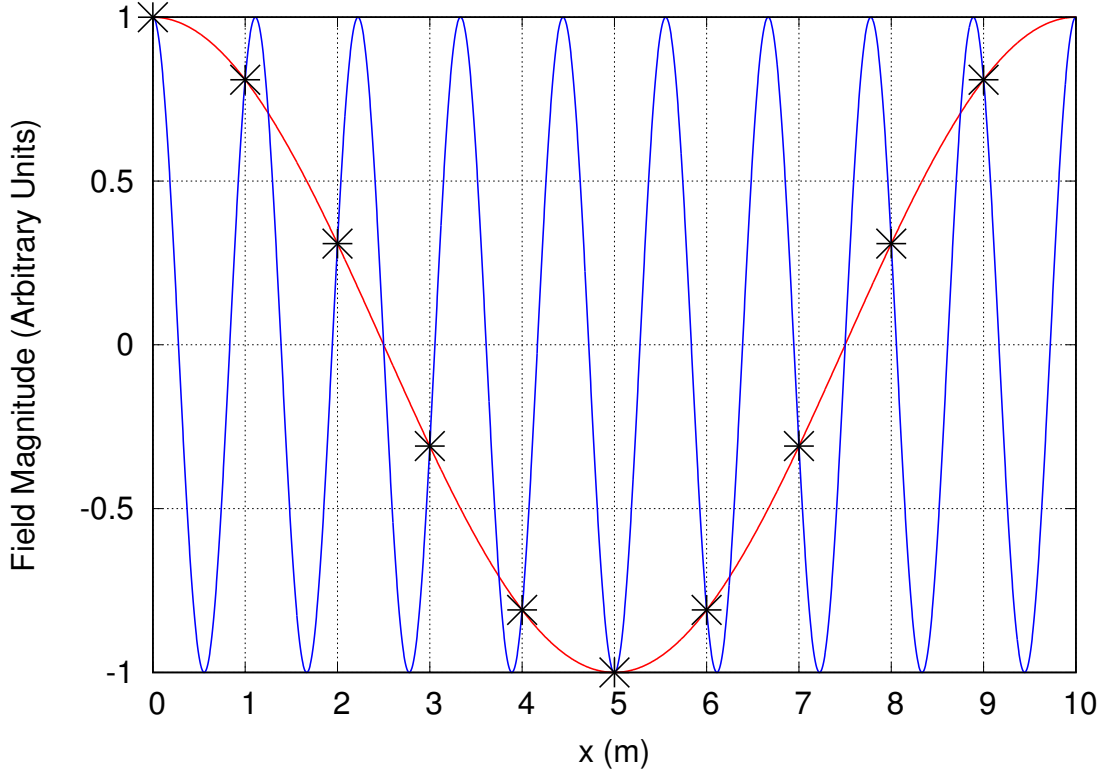


**Figure 2.2:** Two sinusoidal waves at 30MHz (red) and 300MHz (blue) that align with the same sampling points (crosses)

## 2.3 Conductive Media

Lossless media can be simulated by using appropriate values of  $\epsilon$  and  $\mu$ . However, to model conductive materials the conduction term of Maxwell's equations must be considered. [6]

### 2.3.1 Electric Conductivity

For a material with an electric conductivity  $\sigma_e$  Ampere's law can be written as:

$$\frac{\partial \mathbf{D}}{\partial t} + \sigma_e \mathbf{E} = \nabla \times \mathbf{H} \quad (2.44)$$

Discretizing this in the x direction as for (2.8) gives:

$$\begin{aligned} & \epsilon \left( \frac{E_{x_{i+\frac{1}{2},j,k}}^{n+\frac{1}{2}} - E_{x_{i+\frac{1}{2},j,k}}^{n-\frac{1}{2}}}{\Delta t} \right) + \sigma_e \left( \frac{E_{x_{i+\frac{1}{2},j,k}}^{n+\frac{1}{2}} + E_{x_{i+\frac{1}{2},j,k}}^{n-\frac{1}{2}}}{2} \right) \\ & = \left( \frac{H_{z_{i+\frac{1}{2},j+\frac{1}{2},k}}^n - H_{z_{i+\frac{1}{2},j-\frac{1}{2},k}}^n}{\Delta y} \right) - \left( \frac{H_{y_{i+\frac{1}{2},j,k+\frac{1}{2}}}^n - H_{y_{i+\frac{1}{2},j,k-\frac{1}{2}}}^n}{\Delta z} \right) \end{aligned} \quad (2.45)$$

As the update equations are staggered in time the loss cannot be evaluated at  $t = n\Delta t$ . To account for this the lossy term has been averaged in time. Rearranging to get an update equation in the form (2.10) gives:

$$E_{x_{i+\frac{1}{2},j,k}}^{n+\frac{1}{2}} = \frac{\frac{\epsilon}{\Delta t} - \frac{\sigma_e}{2}}{\frac{\epsilon}{\Delta t} + \frac{\sigma_e}{2}} E_{x_{i+\frac{1}{2},j,k}}^{n-\frac{1}{2}} + \frac{1}{\frac{\epsilon}{\Delta t} + \frac{\sigma_e}{2}} \left[ \left( \frac{H_{z_{i+\frac{1}{2},j+\frac{1}{2},k}}^n - H_{x_{i+\frac{1}{2},j-\frac{1}{2},k}}^n}{\Delta y} \right) - \left( \frac{H_{y_{i+\frac{1}{2},j,k+\frac{1}{2}}}^n - H_{y_{i+\frac{1}{2},j,k-\frac{1}{2}}}^n}{\Delta z} \right) \right] \quad (2.46)$$

Update equations for  $E_y$  and  $E_z$  can be similarly derived. These equations fulfil the CFL stability condition (2.39) assuming:

$$\frac{\frac{\epsilon}{\Delta t} - \frac{\sigma_e}{2}}{\frac{\epsilon}{\Delta t} + \frac{\sigma_e}{2}} \leq 1 \quad (2.47)$$

Which is true as long as the conductivity  $\sigma_e$  is real and positive.

## 2.4 Thin Layer Models

The speed of an electromagnetic wave in a conductive material is given by:

$$v = \frac{1}{\sqrt{\sigma \mu_r}} \quad (2.48)$$

Where  $\mu_r$  and  $\sigma$  are the relative permeability and conductivity of the medium through which the wave is propagating. The wavelength of the wave is given by:

$$\lambda = \frac{v}{f} \quad (2.49)$$

When transitioning from one medium to another, the speed of the wave changes. The frequency of the wave will remain constant so as to conserve energy, as such it is necessary that the wavelength changes proportionally to the wave's speed so as to satisfy (2.49). The change in wavelength must be considered when choosing a mesh size based on the aliasing criteria in Section 2.2.1. Combining (2.49) and the aliasing mesh size restriction (Fig 2.2) gives a mesh size restriction that is based on the maximum frequency of interest and the material with the lowest propagation speed:

$$\Delta x \leq \frac{v_{min}}{10f_{max}} \quad (2.50)$$

When modelling a material sheet it is often necessary to have multiple cells across the width of the material to accurately model waves propagating through the sheet including internal reflections and resonances. For lossy materials it is necessary to have multiple cells to correctly model the attenuation of the wave.

When creating a model it is desirable to try to use as coarse a mesh as possible to reduce the runtime and memory. However, it is also desirable to have multiple cells across

the width of the sheet for the reasons given above, this limits the chosen cell size to a fraction of the sheet width which limits how coarse the mesh can be. To overcome this limitation techniques have been developed to model thin material sheets, where the thickness of the sheet is much smaller than the mesh cell size. Thin layer models are used to provide improvements to efficiency in multi-scale simulations such as microwave devices[14], electromagnetic aircraft response assessment[15, 16] and thin material surfaces such as carbon fibre composites (CFC)[17], wire meshes[18] or graphene [19] etc.

Whilst the work presented here focuses primarily on the FDTD method, early development of thin layer models was carried out using TLM (Transmission-Line Matrix)[20, 21] with the underlying concepts informing later work in FDTD. Early FDTD thin boundary techniques were used to model dielectric slabs [22, 23]. While these techniques could be used to reduce simulation costs for some specific cases they were unable to represent lossy, conductive materials. It was not until the introduction of conductive thin boundaries [8, 24] that the method found wide practical use. A sheet with a thickness that is small compared to the wavelength of the highest frequency of interest will be effectively frequency independent and therefore an approximation of a conductive sheet is adequate. But there are also applications where thin boundaries that can accurately represent frequency dependent media are beneficial, such as Carbon Fibre Composite (CFC)[25]. The development of early surface impedance boundary conditions (SIBC) that used a materials impedance ( $Z$ ) or admittance ( $Y$ ) parameters to determine the frequency dependent *reflection* from such boundaries expanded further the utility of thin boundaries [26–33]. However it was not until several years later that thin boundary models of transmission through conductors were introduced [17, 31, 34, 35]. For an SIBC to work they must make use of a convolution, this can be computationally taxing if not handled correctly and much work has been done recently that attempts to tackle the problem with efficient discrete convolution algorithms [36–38]. A different approach to the problem is to use a 1D sub-grid, simulating the field inside the boundary separately from the main grid [39].

Another area of the development of thin boundary methods focuses on the development of conformal techniques. The previously discussed advancements all use thin sheets that must be aligned to the orthogonal Yee cell grid. However, the development of methods to deform thin sheets to conform to non-aligned and curved thin surfaces is ongoing [40–42].

There has also been work developing anisotropic thin boundaries. That is to say boundaries representing materials whose properties are dependent on its orientation in relation to the polarisation of an incident field. An example of a materials that displays such behaviour are carbon fibre composites (CFC)[43], these materials are used extensively in automotive and aeronautical engineering and are mostly used for components that are

thin in comparison to the whole device (i.e. wings on an aeroplane), this makes them an ideal candidate for thin boundary modelling [44]. Anisotropic thin boundaries have been implemented in FDTD using the face-centred model described in Section 2.4.2. Such boundaries have also been implemented using the unstructured (non-orthogonal) TLM method [16, 21, 45, 46], this has the advantage of not having to conform to a grid and therefore more complex geometries can be modelled without introducing errors such as those discussed in Section 3.

### 2.4.1 Maloney's Thin Layer Model

The Maloney method [8, 47] represents a thin sheet boundary with a given conductivity  $\sigma_s$  and permittivity  $\varepsilon_s$  with a thickness  $d$  much smaller than the mesh size as shown in Figure 2.3. The thickness should also be much smaller than the skin depth and wavelength of the highest frequency of interest. The electric and magnetic fields normal to the thin sheet ( $E_{y_{i,j+\frac{1}{2},k}}^{n-\frac{1}{2}}$  and  $E_{y_{i+1,j+\frac{1}{2},k}}^{n-\frac{1}{2}}$ ) are split into internal  $E_{in}$  and external  $E_{out}$  fields.

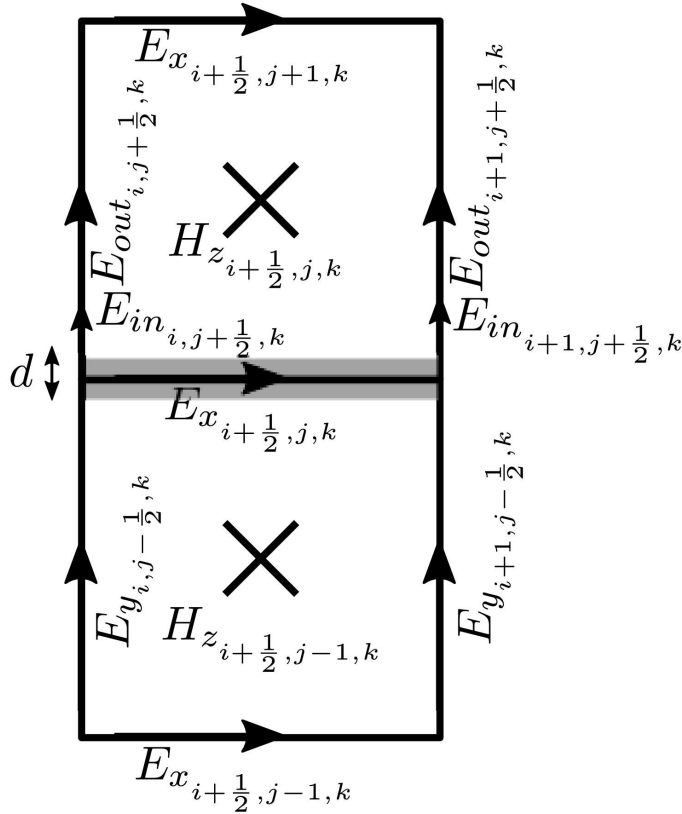


**Figure 2.3:** Cell design of a thin sheet implemented using the Maloney method. Arrows represent discrete electric fields and crosses represent discrete magnetic fields. The thin material sheet is denoted by the dark grey area.

The external electric field is updated as normal:

$$E_{out_{i,j+\frac{1}{2},k}}^{n+\frac{1}{2}} = E_{out_{i,j+\frac{1}{2},k}}^{n-\frac{1}{2}} + \frac{\Delta t}{\varepsilon_{x_{i,j+\frac{1}{2},k}}} \left[ \left( \frac{H_{x_{i,j+\frac{1}{2},k+\frac{1}{2}}}^n - H_{x_{i,j+\frac{1}{2},k-\frac{1}{2}}}^n}{\Delta z} \right) - \left( \frac{H_{z_{i+\frac{1}{2},j+\frac{1}{2},k}}^n - H_{z_{i+\frac{1}{2},j-\frac{1}{2},k}}^n}{\Delta x} \right) \right] \quad (2.51)$$

However the update for the internal field is modified by the material's electric properties similar to (2.46):

$$E_{in_{i,j+\frac{1}{2},k}}^{n+\frac{1}{2}} = \frac{\frac{\varepsilon_s}{\Delta t} - \frac{\sigma_s}{2}}{\frac{\varepsilon_s}{\Delta t} + \frac{\sigma_s}{2}} E_{in_{i,j+\frac{1}{2},k}}^{n-\frac{1}{2}} + \frac{1}{\frac{\varepsilon_s}{\Delta t} + \frac{\sigma_s}{2}} \left[ \left( \frac{H_{x_{i,j+\frac{1}{2},k+\frac{1}{2}}}^n - H_{x_{i,j+\frac{1}{2},k-\frac{1}{2}}}^n}{\Delta z} \right) - \left( \frac{H_{z_{i+\frac{1}{2},j+\frac{1}{2},k}}^n - H_{z_{i+\frac{1}{2},j-\frac{1}{2},k}}^n}{\Delta x} \right) \right] \quad (2.52)$$

Next the tangential electric fields ( $E_{x_{i+\frac{1}{2},j,k}}^{n+\frac{1}{2}}$  and  $E_{z_{i,j,k+\frac{1}{2}}}^{n+\frac{1}{2}}$ ) must be updated:

$$E_{x_{i+\frac{1}{2},j,k}}^{n+\frac{1}{2}} = \frac{\frac{\varepsilon_{ave}}{\Delta t} - \frac{\sigma_{ave}}{2}}{\frac{\varepsilon_{ave}}{\Delta t} + \frac{\sigma_{ave}}{2}} E_{x_{i+\frac{1}{2},j,k}}^{n-\frac{1}{2}} + \frac{1}{\frac{\varepsilon_{ave}}{\Delta t} + \frac{\sigma_{ave}}{2}} \left[ \left( \frac{H_{z_{i+\frac{1}{2},j+\frac{1}{2},k}}^n - H_{z_{i+\frac{1}{2},j-\frac{1}{2},k}}^n}{\Delta y} \right) - \left( \frac{H_{y_{i+\frac{1}{2},j,k+\frac{1}{2}}}^n - H_{y_{i+\frac{1}{2},j,k-\frac{1}{2}}}^n}{\Delta z} \right) \right] \quad (2.53)$$

Where  $d$  is the thickness of the thin boundary. This time a proportional average of the material electric properties and the surrounding media's electric properties is used given by:

$$\varepsilon_{ave} = \left(1 - \frac{d}{\Delta z}\right)\varepsilon + \frac{d}{\Delta z}\varepsilon_s \quad , \quad \sigma_{ave} = \frac{d}{\Delta z}\sigma_s \quad (2.54)$$

Finally, the tangential magnetic fields must be updated, these will rely on the internal and external electric fields of the thin sheet

$$H_{x_{i+\frac{1}{2},j,k}}^{n+1} = H_{x_{i+\frac{1}{2},j,k}}^{n-1} + \frac{\Delta t}{\mu} \left[ \frac{\Delta y - d}{\Delta y} \left( \frac{E_{out_{i,j+\frac{1}{2},k}}^n - E_{out_{i,j-\frac{1}{2},k}}^n}{\Delta z} \right) + \frac{d}{\Delta y} \left( \frac{E_{in_{i,j+\frac{1}{2},k}}^n - E_{in_{i,j-\frac{1}{2},k}}^n}{\Delta z} \right) + \left( \frac{E_{z_{i+1,j+\frac{1}{2},k}}^n - E_{z_{i,j+\frac{1}{2},k}}^n}{\Delta y} \right) \right] \quad (2.55)$$

$$H_{z_{i+\frac{1}{2},j,k}}^{n+1} = H_{z_{i+\frac{1}{2},j,k}}^{n-1} + \frac{\Delta t}{\mu} \left[ \frac{\Delta y - d}{\Delta y} \left( \frac{E_{out_{i,j+\frac{1}{2},k}}^n - E_{out_{i,j-\frac{1}{2},k}}^n}{\Delta x} \right) + \frac{d}{\Delta y} \left( \frac{E_{in_{i,j+\frac{1}{2},k}}^n - E_{in_{i,j-\frac{1}{2},k}}^n}{\Delta x} \right) - \left( \frac{E_{x_{i+\frac{1}{2},j+1,k}}^n - E_{x_{i+\frac{1}{2},j,k}}^n}{\Delta y} \right) \right] \quad (2.56)$$

Note that for the tangential magnetic fields the electric field used for the thin sheet is an average of the internal and external electric fields weighted by the thickness of the sheet. This method is stable within the normal stability conditions of the Yee scheme and requires the storage of only the internal fields as an additional memory resource. Compared to other edge based thin boundaries the Maloney algorithm has gained popularity due to its usability for both dielectric and resistive sheets, its stability for both types of material and accurate handling of both tangential and normal fields of the sheet [48].

### 2.4.2 A Face Centered Anisotropic SIBC

The Maloney method relies on collocating the fields on the *edge* of the Yee cell (Figure 2.1), the method detailed here collocates the field at the centre of the *face* of the cell. This method implements a surface impedance boundary condition to allow frequency dependent materials to be simulated [1]. It also allows the implementation of anisotropic thin boundaries, that is to say boundaries whose properties are dependent on the polarisation of the incident field. To do this the tangential electromagnetic fields on the surface of the material must be resolved into orthogonal polarisation components along a plane of incidence as shown in Figure 2.4.

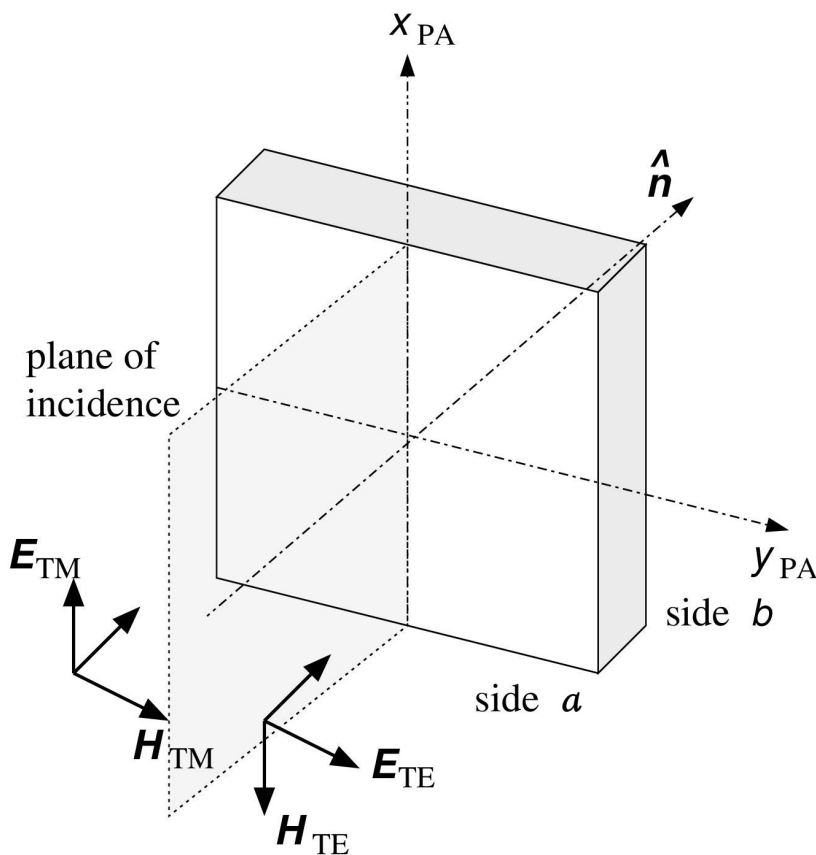


Figure 2.4: Axes of face centred SIBC [1].

The discrete fields are considered on the surface of the face on each side of the boundary denoted as side “a” and side “b”. The relationship in the frequency domain between the fields on each side of the boundary is determined by the surface impedance matrix  $\mathbf{Z}(\omega)$  where omega is the angular frequency of the field:

$$\begin{bmatrix} E_{TM}^a \\ E_{TM}^b \\ E_{TE}^a \\ E_{TE}^b \end{bmatrix} = \mathbf{Z}(\omega) \begin{bmatrix} H_{TM}^a \\ -H_{TM}^b \\ H_{TE}^a \\ -H_{TE}^b \end{bmatrix} \quad (2.57)$$

Where the surface impedance matrix is given by:

$$\mathbf{Z}(\omega) = \begin{bmatrix} Z_{11}^{TM} & Z_{12}^{TM} & 0 & 0 \\ Z_{21}^{TM} & Z_{22}^{TM} & 0 & 0 \\ 0 & 0 & Z_{11}^{TE} & Z_{12}^{TE} \\ 0 & 0 & Z_{21}^{TE} & Z_{22}^{TE} \end{bmatrix} \quad (2.58)$$

In the case that the material is isotropic the following would be true:

$$Z_{pq}^{TM}(\omega) = Z_{pq}^{TE}(\omega) \quad (2.59)$$

The TM and TE components in Figure 2.4 are defined with reference to the local principal axis of the surface of the material. This is not necessarily the same axis of the FDTD grid. Therefore the input magnetic fields must be rotated to align with the grid by using:

$$\begin{bmatrix} E_x^a \\ E_x^b \\ E_y^a \\ E_y^b \end{bmatrix} = \mathbf{B}(\alpha) \mathbf{Z} \mathbf{A}(\alpha) \begin{bmatrix} H_x^a \\ H_x^b \\ H_y^a \\ H_y^b \end{bmatrix} \quad (2.60)$$

Where  $\mathbf{A}(\alpha)$  and  $\mathbf{B}(\alpha)$  are rotation matrices as a function of  $\alpha$  which is the angle between the local principal axis  $E_{TM}$  and the global grids  $x$ -axis:

$$\mathbf{A}^\pm(\alpha) = \mathbf{A}_c^\pm \cos(\alpha) + \mathbf{A}_s^\pm \sin(\alpha) \quad (2.61)$$

$$\mathbf{B}^\pm(\alpha) = \mathbf{B}_c^\pm \cos(\alpha) + \mathbf{B}_s^\pm \sin(\alpha) \quad (2.62)$$

Where the  $\pm$  symbol denotes which side of the material is facing the positive  $z$ -axis and  $\mathbf{A}_c^\pm, \mathbf{A}_s^\pm, \mathbf{B}_c^\pm$  and  $\mathbf{B}_s^\pm$  are constant matrices containing zeros and  $\pm 1$ . In an example of a clockwise rotation of  $90^\circ$  the rotation matrices would be:

$$\mathbf{A}^+ = \begin{bmatrix} 1 & 0 & 0 & 0 \\ 0 & -1 & 0 & 0 \\ 0 & 0 & 1 & 0 \\ 0 & 0 & 0 & -1 \end{bmatrix}, \mathbf{A}^- = \begin{bmatrix} 0 & -1 & 0 & 0 \\ 1 & 0 & 0 & 0 \\ 0 & 0 & 0 & -1 \\ 0 & 0 & 1 & 0 \end{bmatrix} \quad (2.63)$$

The tangential electric and magnetic field components on either side of the SIBC boundary are related by convolutions of the form:

$$E_p(t) = \sum_q^4 \int_0^t z_{pq}(t-\tau) H_q(\tau) d\tau \quad (2.64)$$

Where  $z_{pq}$  is the Inverse Fourier Transform of  $Z(\omega)$ .  $Z(\omega)$  can be determined through an analytical or numerical model, or from physical measurement. The impedance matrix is then fitted to a partial-fraction expansion (PFE) given by:

$$Z_{pq}(s) = Z_{pq}^\infty + \sum_{m=1}^{N_{pq}} \frac{r_{pq}^m}{j\omega - p_{pq}^m} \quad (2.65)$$

Where  $r_{pq}^m$  and  $p_{pq}^m$  are residues and poles (real or complex conjugate pairs) respectively,  $Z_{pq}^\infty$  are the asymptotic high frequency response and  $N_{pq}$  is the number of residue, pole pairs.

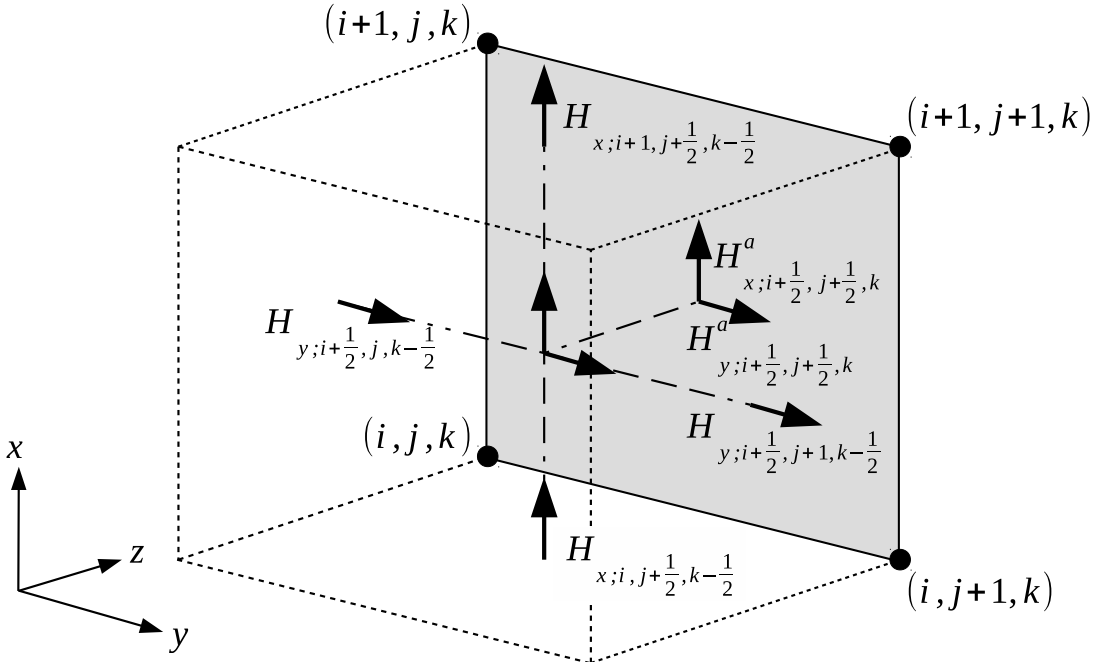


**Figure 2.5:** Discrete magnetic fields surrounding SIBC surface.

Taking the example of a  $z$ -normal face as shown in Figure 2.5 the electric components on at the centre of the face are given by:

$$\begin{bmatrix} E_x^a \\ E_x^b \\ E_y^a \\ E_y^b \end{bmatrix}_{i+\frac{1}{2},j+\frac{1}{2},k}^n = \mathbf{B}(\alpha) \mathbf{Z}_{a,b}^{TM,TE} \mathbf{A}(\alpha) \begin{bmatrix} H_x^a \\ H_x^b \\ H_y^a \\ H_y^b \end{bmatrix}_{i+\frac{1}{2},j+\frac{1}{2},k}^n \quad (2.66)$$

Therefore it is necessary to evaluate the tangential H fields at the centre of the face. Firstly the H fields are linearly interpolated to get the tangential magnetic fields half a cell away from the centre of the face along the normal (z in this case) axis:

$$\begin{aligned} H_{x_{i+\frac{1}{2},j+\frac{1}{2},k-\frac{1}{2}}}^n &= \frac{1}{2} \left[ H_{x_{i,j+\frac{1}{2},k-\frac{1}{2}}}^n + H_{x_{i+1,j+\frac{1}{2},k-\frac{1}{2}}}^n \right] \\ H_{x_{i+\frac{1}{2},j+\frac{1}{2},k+\frac{1}{2}}}^n &= \frac{1}{2} \left[ H_{x_{i,j+\frac{1}{2},k+\frac{1}{2}}}^n + H_{x_{i+1,j+\frac{1}{2},k+\frac{1}{2}}}^n \right] \\ H_{y_{i+\frac{1}{2},j+\frac{1}{2},k-\frac{1}{2}}}^n &= \frac{1}{2} \left[ H_{y_{i+\frac{1}{2},j,k-\frac{1}{2}}}^n + H_{y_{i+\frac{1}{2},j+1,k-\frac{1}{2}}}^n \right] \\ H_{y_{i+\frac{1}{2},j+\frac{1}{2},k+\frac{1}{2}}}^n &= \frac{1}{2} \left[ H_{y_{i+\frac{1}{2},j,k+\frac{1}{2}}}^n + H_{y_{i+\frac{1}{2},j+1,k+\frac{1}{2}}}^n \right] \end{aligned} \quad (2.67)$$

This is a low order approximation that has been considered as a possible cause of instability when implementing collocated SIBC's [49], however the method presenting has been demonstrated to be late stage stable for a number of test cases. It should be noted that there is only empirical evidence of stability and no mathematical proof of such is given.

To collocate the discrete electric and magnetic fields in both time and space the tangential magnetic fields at the centre of the face are approximated from (2.67) to give:

$$\begin{aligned} H_{x_{i+\frac{1}{2},j+\frac{1}{2},k}}^{a+\frac{1}{2}} &\approx H_{x_{i+\frac{1}{2},j+\frac{1}{2},k-\frac{1}{2}}}^n \\ H_{x_{i+\frac{1}{2},j+\frac{1}{2},k}}^{b+\frac{1}{2}} &\approx H_{x_{i+\frac{1}{2},j+\frac{1}{2},k+\frac{1}{2}}}^n \\ H_{y_{i+\frac{1}{2},j+\frac{1}{2},k}}^{a+\frac{1}{2}} &\approx H_{y_{i+\frac{1}{2},j+\frac{1}{2},k-\frac{1}{2}}}^n \\ H_{y_{i+\frac{1}{2},j+\frac{1}{2},k}}^{b+\frac{1}{2}} &\approx H_{y_{i+\frac{1}{2},j+\frac{1}{2},k+\frac{1}{2}}}^n \end{aligned} \quad (2.68)$$

Where 'a' and 'b' denote which side of the face the magnetic component represents. Combining (2.67) with (2.68) and substituting into (2.66) give the tangential electric fields update as:

$$\begin{bmatrix} E_x^a \\ E_x^b \\ E_y^a \\ E_y^b \end{bmatrix}_{i+\frac{1}{2},j+\frac{1}{2},k}^n = \mathbf{B}(\alpha) \mathbf{Z}_{a,b}^{TM,TE} \mathbf{A} \frac{1}{2}(\alpha) \begin{bmatrix} H_{x_{i,j+\frac{1}{2},k-\frac{1}{2}}}^{n-\frac{1}{2}} + H_{x_{i+1,j+\frac{1}{2},k-\frac{1}{2}}}^{n-\frac{1}{2}} \\ H_{x_{i,j+\frac{1}{2},k+\frac{1}{2}}}^{n-\frac{1}{2}} + H_{x_{i+1,j+\frac{1}{2},k+\frac{1}{2}}}^{n-\frac{1}{2}} \\ H_{y_{i+\frac{1}{2},j,k-\frac{1}{2}}}^{n-\frac{1}{2}} + H_{y_{i+\frac{1}{2},j+1,k-\frac{1}{2}}}^{n-\frac{1}{2}} \\ H_{y_{i+\frac{1}{2},j,k+\frac{1}{2}}}^{n-\frac{1}{2}} + H_{y_{i+\frac{1}{2},j+1,k+\frac{1}{2}}}^{n-\frac{1}{2}} \end{bmatrix} \quad (2.69)$$

Where  $\mathbf{Z}_{a,b}^{TM,TE}$  is a convolution operator corresponding to (2.64).

The tangential magnetic field components adjacent to the face are updated as in (2.9) with the electric field at the centre of the face replaced by the appropriate tangential electric field calculated by (2.69). For example:

$$H_{x;i,j+\frac{1}{2},k+\frac{1}{2}}^{n+1} = H_{x;i,j+\frac{1}{2},k+\frac{1}{2}}^n + \frac{\Delta t}{\mu} \left[ \left( \frac{E_{y;i,j+\frac{1}{2},k+1}^{n+\frac{1}{2}} - E_{y;i,j+\frac{1}{2},k}^{b^{n+\frac{1}{2}}}}{\Delta z} \right) - \left( \frac{E_{z;i,j+1,k+\frac{1}{2}}^{n+\frac{1}{2}} - E_{z;i,j,k+\frac{1}{2}}^{n+\frac{1}{2}}}{\Delta y} \right) \right] \quad (2.70)$$

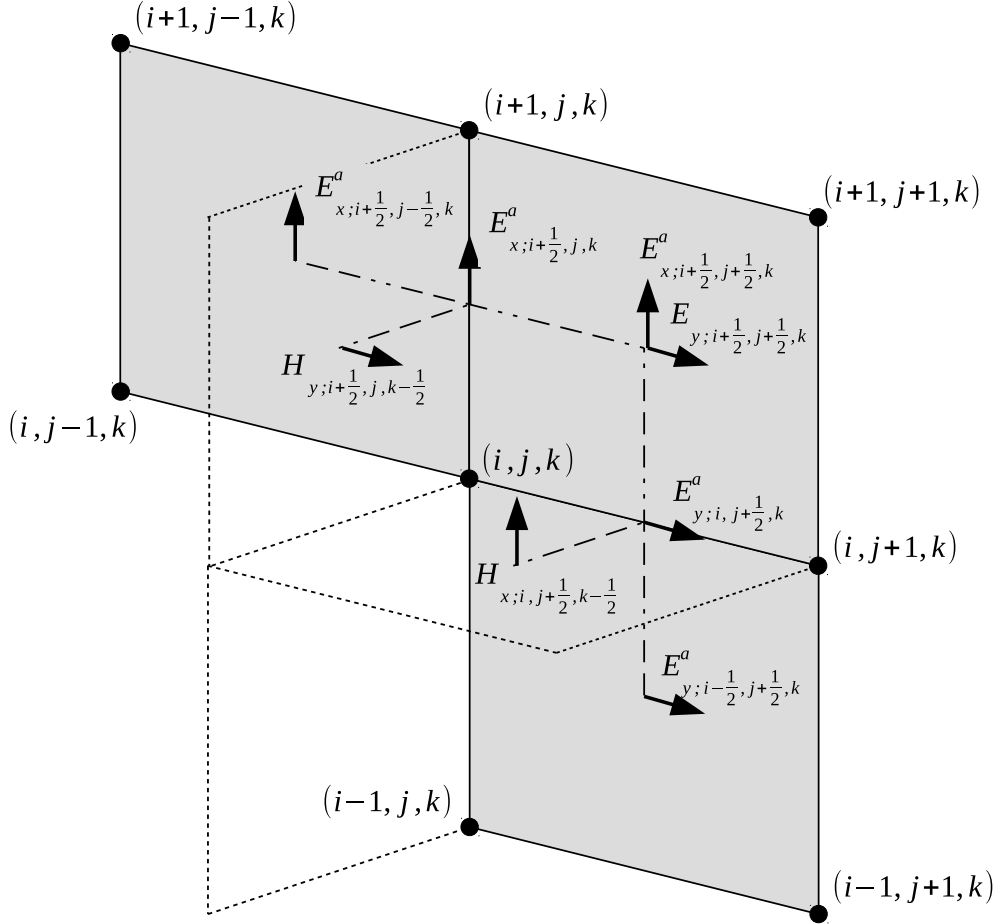


**Figure 2.6:** Discrete fields surrounding multiple panel SIBC surface.

The electric field components at the edge of a face are determined by averaging the fields at the centre of adjacent faces as shown in Figure 2.6:

$$E_{y;i,j+\frac{1}{2},k}^{b^{n+\frac{1}{2}}} = \frac{1}{2} \left[ E_{y;i-\frac{1}{2},j+\frac{1}{2},k}^{b^{n+\frac{1}{2}}} + E_{y;i+\frac{1}{2},j+\frac{1}{2},k}^{b^{n+\frac{1}{2}}} \right] \quad (2.71)$$

To validate the face centred model a test case[1] was used that consists of a 1m radius hollow spherical shell made from conductive material. The material of the shell was 5mm

thick with a conductivity of 200 S/m. As the structure is doubly curved the mesh is significantly stair-cased, as shown in Figure 2.7, which makes it ideal for measuring the limits of the face centred model.

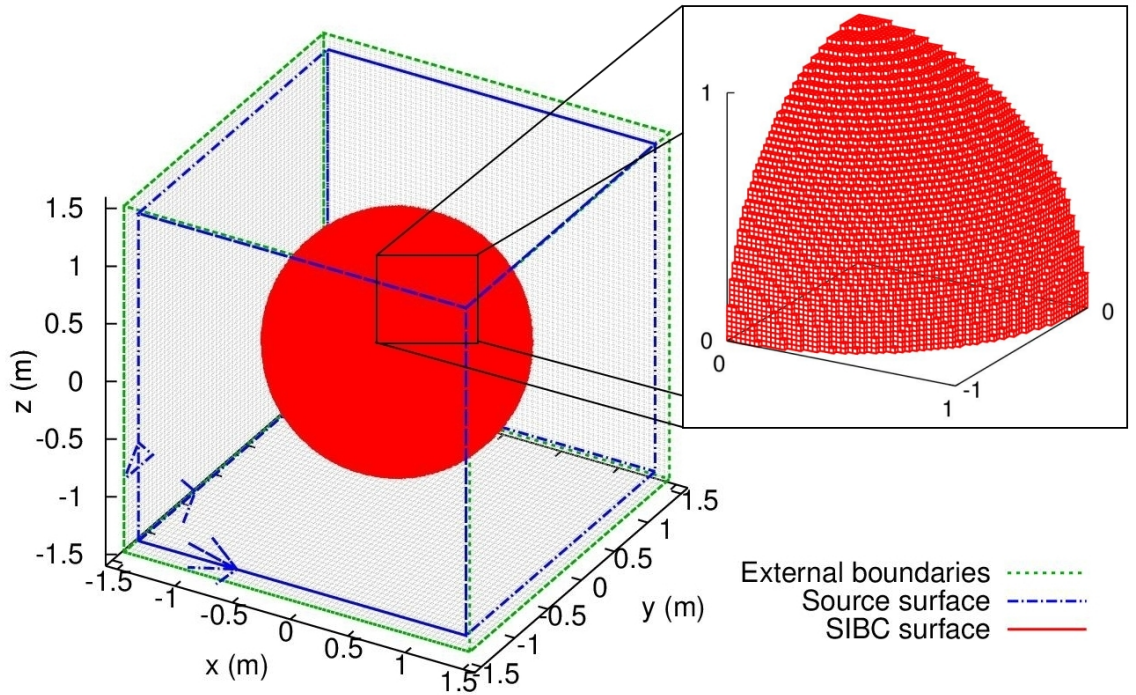


**Figure 2.7:** Set-up of a 1m radius hollow spherical shell made from a material with a conductivity of 200 S/m that is 5mm thick. The shell is illuminated by a  $z$ -polarised plane wave.

The sphere was illuminated by a  $z$ -polarised plane-wave propagating along the  $y$ -axis. The shielding effectiveness (SE) of the material was measured at the centre of the sphere. SE is the ratio of the internal to incident electric field strength. SE is usually quoted in decibels and is given by:

$$SE = 20\log_{10}\left(\frac{E_{inc}}{E_{int}}\right) \quad (2.72)$$

The frequency response of the SE is shown in Figure 2.8. Around the first resonance it can be seen that the error in SE is approximately 6 dB for the edge-centred case and around 3dB for the face-centred case compared to an analytic solution[3]. There are also noticeable reductions in the spurious resonances following the first resonance for the face centred case when compared to the edge centred model. The cause of these resonances is discussed in Chapter 3. Using Feature Selective Validation [50], the Amplitude Difference Measure and Feature Difference Measure, in comparison to the analytic solution, for the face centred method were 0.13, 0.61 compared to 0.19, 0.71 for the edge centred method. The error in both methods for the low frequency can be attributed to the breakdown of the FDTD method for low frequencies [51].

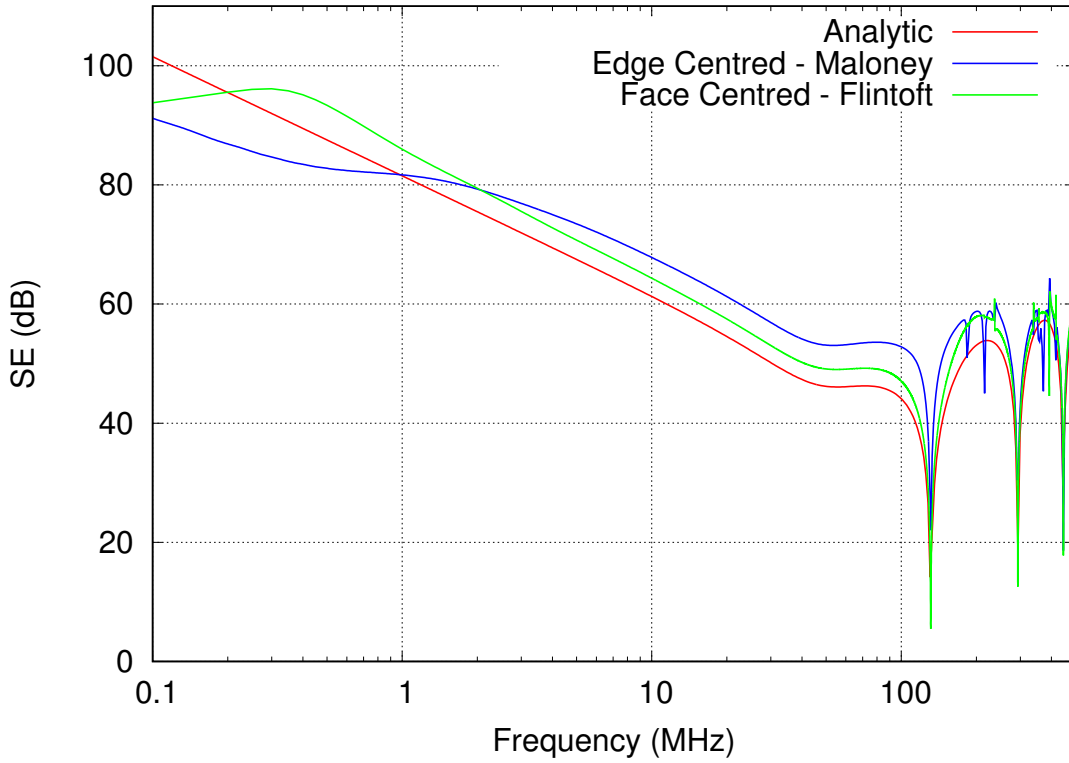


**Figure 2.8:** Shielding effectiveness at the centre of the hollow spherical shell with  $\sigma = 200\text{S/m}$  and thickness  $h = 5\text{ mm}$  comparing the analytic solution to the different FDTD thin layer methods.

It can be seen that the magnitude of the resonant spikes increase with frequency, this can be attributed to the decreasing skin depth of the conductive shell material. The skin depth is the distance a wave must travel to be attenuated by a factor of  $\frac{1}{e}$ . Figure 2.9 shows skin depth as a function of frequency, the shell is 5mm thick and it can be seen that that, for the frequency range of interest, the shell is between 1 and 5 skin depths thick.

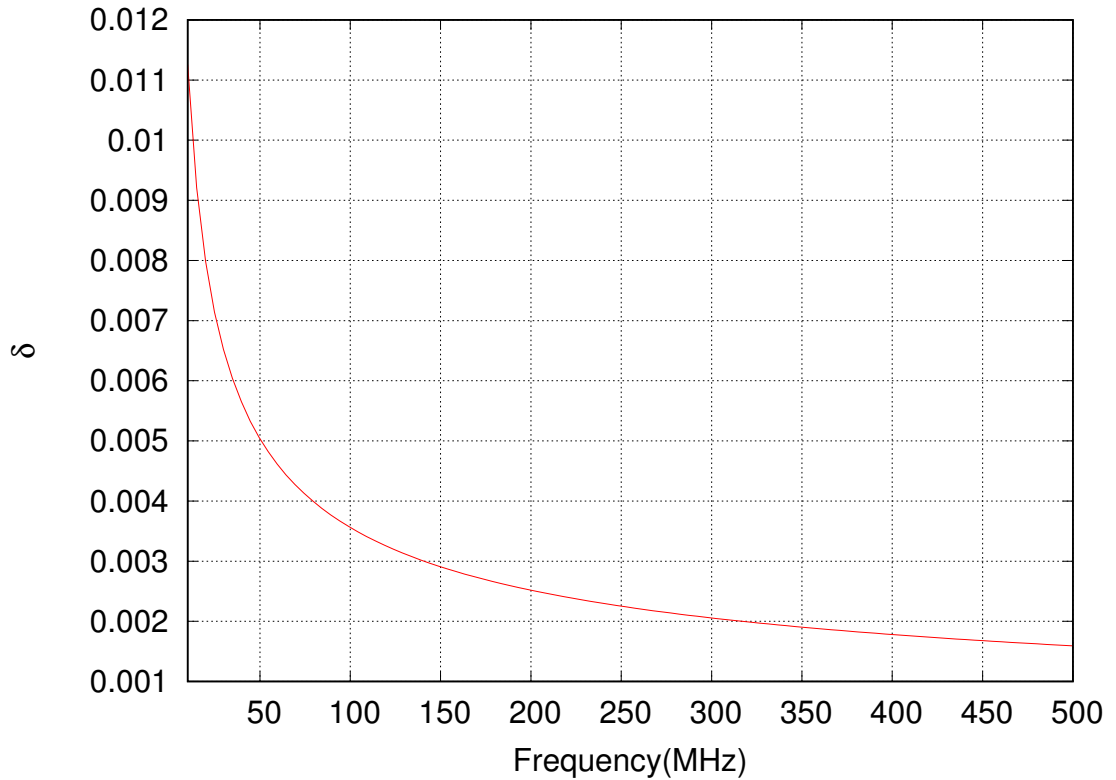


**Figure 2.9:** Skin depth  $\delta$  as a function of frequency for the problem set up in Figure 2.7

The improvement seen using the face centred method can be attributed to the more accurate handling of corners. In the Maloney method a corner must be represented by two parallel thin boundary edges. However this means that for some field polarisations the thin boundary model will be applied twice, effectively modelling a material of twice the required thickness. The face centred model calculates these parallel edges in a single calculation, averaging the calculated field on each edge.

### 2.4.3 Surface edge updates

In this section an update to the face centred SIBC is proposed to better account for the treatment of fields at edges of surfaces comprised of thin layer faces. The work in this section ((2.4.3) was carried out solely by the author as an addition to the Face-Centred method.

The implementation of the face centred SIBC detailed above assumes that each face is adjacent to another coplanar face on each edge. However, further consideration must be given to cases where the edge of an SIBC is at a corner or terminates in empty space.

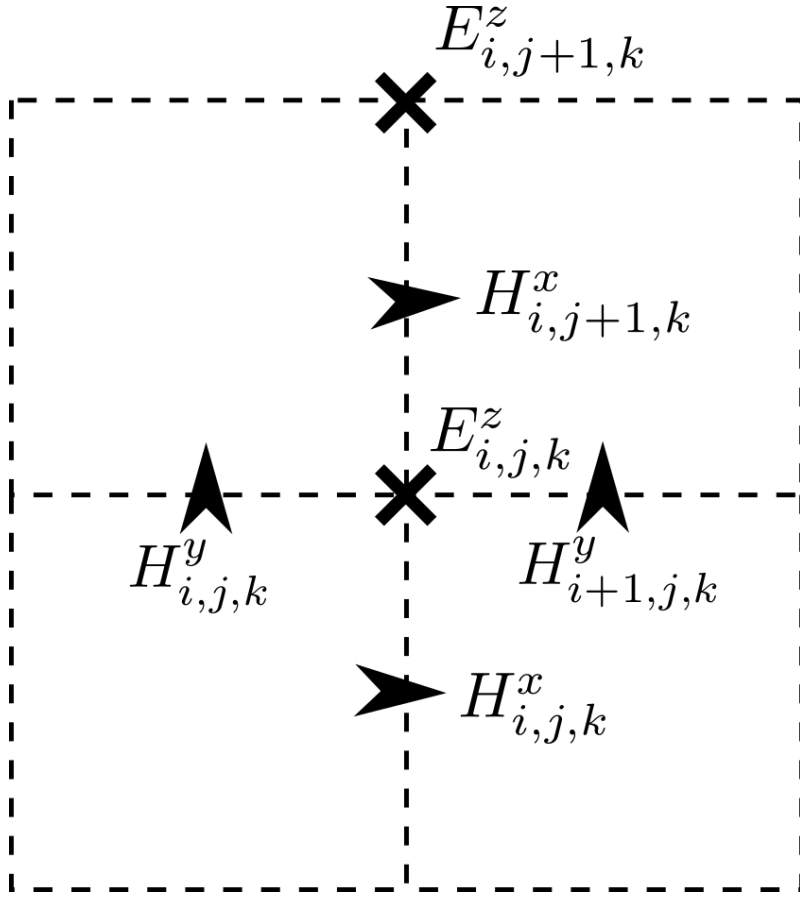


**Figure 2.10:** 2D section of an FDTD grid. The  $z$ -directed E-field is updated using the surrounding  $x$  and  $y$  directed magnetic fields.

Consider Figure 2.10 that depicts the update of magnetic field nodes using the curl of the surrounding magnetic fields according to the equations:

$$H_{i+\frac{1}{2},j+1,k}^{x;n} = H_{+\frac{1}{2},j+1,k}^{x;n-1} + \frac{\Delta t}{\mu} \left( \frac{E_{i,j,k+1}^y - E_{i,j,k}^y}{\Delta z} + \frac{E_{i,j,k}^z - E_{i,j+1,k}^z}{\Delta y} \right) \quad (2.73)$$

$$H_{i+1,j+\frac{1}{2},k}^{y;n} = H_{i+1,j+\frac{1}{2},k}^{y;n-1} + \frac{\Delta t}{\mu} \left( \frac{E_{i,j,k}^x - E_{i,j,k+1}^x}{\Delta z} + \frac{E_{i+1,j,k}^z - E_{i,j,k}^z}{\Delta x} \right) \quad (2.74)$$

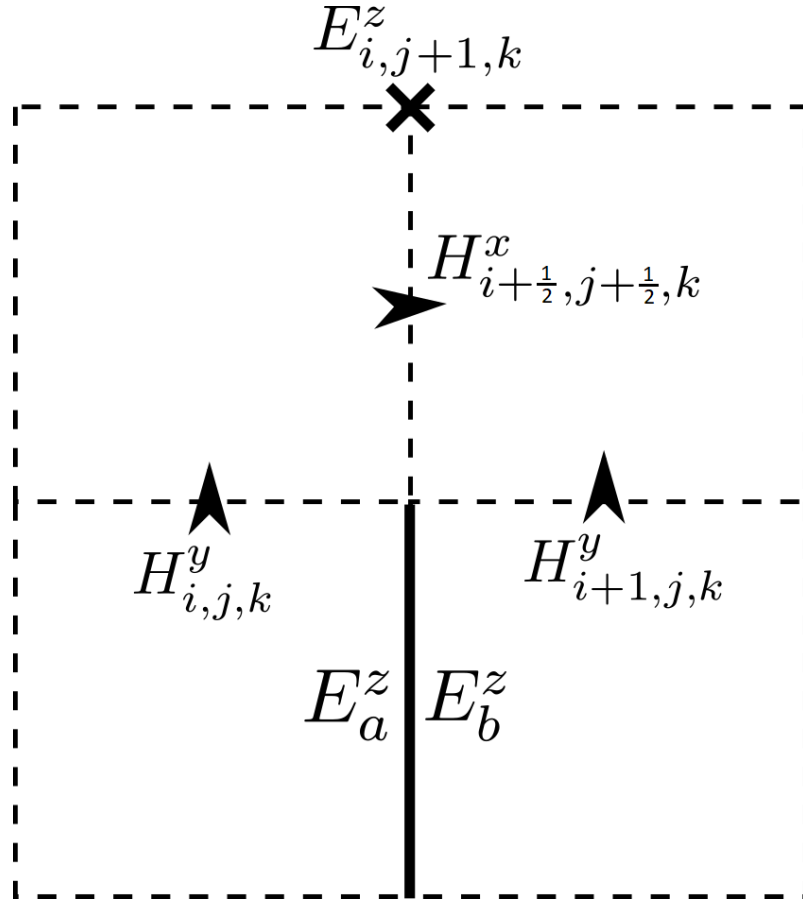


**Figure 2.11:** 2D section of an FDTD grid. The SIBC face (solid black line) calculates the E-field on the each side of the surface. The surrounding magnetic fields should be updated using the average of the two surface E-Fields.

$$H_{i+\frac{1}{2},j+1,k}^{x;n} = H_{i+\frac{1}{2},j+1,k}^{x;n-1} + \frac{\Delta t}{\mu} \left( \frac{E_{i,j,k+1}^y - E_{i,j,k}^y}{\Delta z} + \frac{E_{i,j,k}^z - 0}{\Delta y} \right) \quad (2.75)$$

$$H_{i+1,j+\frac{1}{2},k}^{y;n} = H_{i+1,j+\frac{1}{2},k}^{y;n-1} + \frac{\Delta t}{\mu} \left( \frac{E_{i,j,k}^x - E_{i,j,k+1}^x}{\Delta z} + \frac{0 - E_{i,j,k}^z}{\Delta x} \right) \quad (2.76)$$

When using the face centred SIBC, the electric field nodes on the edges of the face are set to 0, as is the magnetic field node at the centre of the face. The update equations for the surrounding magnetic fields have a 0 term in that case, (2.75) and (2.76) reflect this for Figure 2.11. When updating the electric field nodes surrounding the SIBC face. The E-field at the centre of the face is used to calculate the E field at the edges of the face, where the edge field is half of the centre field value. So, in the case of adjoining faces, the E-field on the shared edge is the average of the field calculated at the centre of each face. This edge field is then added to the magnetic field nodes perpendicular to the SIBC as it would be in the main update equation, shown here:

$$H_{i+1,j+\frac{1}{2},k}^{y;n} = H_{i+1,j+\frac{1}{2},k}^{y;n-1} + \frac{\Delta t}{\mu} \frac{E_b^z}{2\Delta x} \quad (2.77)$$

However the  $H_{i,j+1,k}^x$  node in Figure 2.11 is *not* updated to include the SIBC edge fields. If the SIBC edge fields were to be used to update the parallel  $H_x$  node, the following update equation would be used:

$$H_{i+\frac{1}{2},j+1,k}^{x;n} = H_{i+\frac{1}{2},j+1,k}^{x;n-1} + \frac{\Delta t}{\mu} \frac{E_a^z + E_b^z}{2\Delta y} \quad (2.78)$$

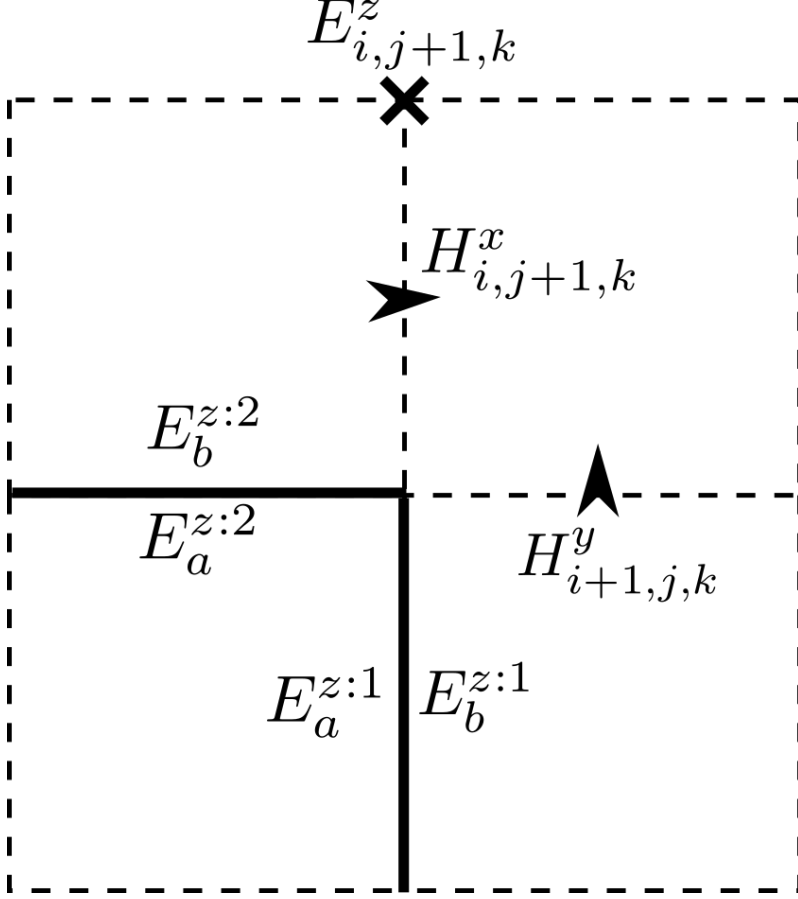


**Figure 2.12:** 2D section of an FDTD grid. The SIBC faces (solid black lines) form a corner with the E-field calculated for each side of each surface. The surrounding magnetic fields should be updated using the average of the surface E-Fields for the  $b$  sides.

In the original implementation described earlier, at an orthogonal intersection of two SIBC faces the adjacent magnetic fields are updated with the edge fields on the appropriate side. In this case the  $a$  side of the SIBC is not used to update the H nodes shown in Figure 2.12 as they are the wrong side of the surface. The SIBC update equations for this case are:

$$H_{i+\frac{1}{2},j+1,k}^{x;n'} = H_{i+\frac{1}{2},j+1,k}^{x;n-1} + \frac{\Delta t}{\mu} \frac{E_b^{z:2}}{2\Delta y} \quad (2.79)$$

$$H_{i+1,j+\frac{1}{2},k}^{y;n'} = H_{i+1,j+\frac{1}{2},k}^{y;n-1} + \frac{\Delta t}{\mu} \frac{E_b^{z:1}}{2\Delta x} \quad (2.80)$$

Further edge corrections based on (2.77) should be included:

$$H_{i+\frac{1}{2},j+1,k}^{x;n} = H_{i+\frac{1}{2},j+1,k}^{x;n'} + \frac{\Delta t E_b^{z:1}}{\mu 2\Delta y} \quad (2.81)$$

$$H_{i+1,j+\frac{1}{2},k}^{y;n} = H_{i+1,j+\frac{1}{2},k}^{y;n'} + \frac{\Delta t E_b^{z:2}}{\mu 2\Delta x} \quad (2.82)$$

To generalise the update equations to include the edge corrections a statement must be added to each SIBC H-field update to include the contribution to adjacent cell faces parallel to the SIBC. For  $H_{i,j+1,k}^x$  due to SIBC 1 in Figure 2.12 the general update equation would be:

$$H_{i+\frac{1}{2},j+1,k}^{x;n} = H_{i+\frac{1}{2},j+1,k}^{x;n-1} + \frac{\Delta t \text{!isAdj}(a)E_a^{z:1} + \text{!isAdj}(b)E_b^{z:1}}{\mu 2\Delta y} \quad (2.83)$$

Where the `!isAdj()` function determines if there is a corner formed with another SIBC face. In the case of Figure 2.12, `!isAdj(a)` would return a value of zero, as there is a SIBC intersecting on the *a* side of the SIBC, meaning there will be no contribution to  $H_{i,j+1,k}^x$  from the *a* side of the SIBC. `!isAdj(b)` would return a value of one as there is not an intersection on the *b* side, therefore the *b* side will contribute.

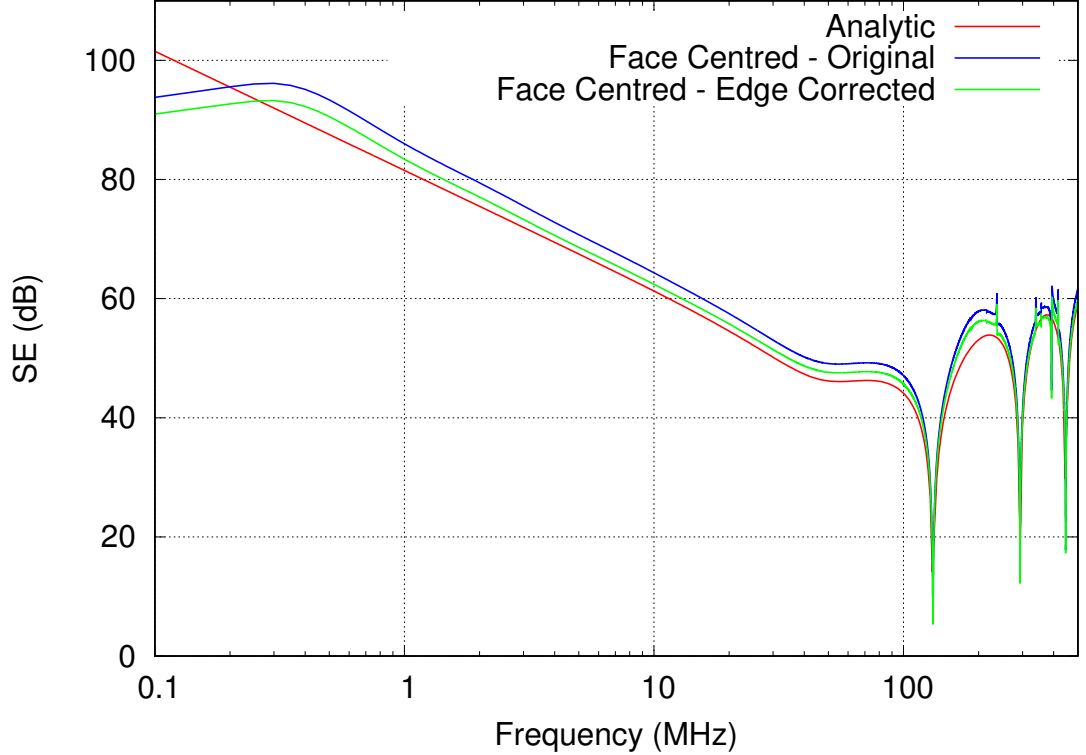


**Figure 2.13:** Shielding effectiveness at the centre of the hollow spherical shell with  $\sigma = 200S/m$  and thickness  $h = 5$  mm comparing the analytic solution to the original and edge corrected to the face centred SIBC models.

The spherical shell model from Figure 2.7 that was used to validate the original face centred algorithm was used to validate the edge corrections. Figure 2.13 shows the SE recorded at the centre of the spherical shell. It can be seen that the error in SE around the first resonance has been reduced from 3 dB to approximately 1.5 dB. The magnitude of the spurious resonances have also been reduced slightly.

## 2.5 Summary

In this chapter the Finite-Difference Time-Domain algorithm has been derived from Maxwell's equations demonstrating its simplicity and ease of implementation. A discussion has been made of the stability and the associated CFLN criterion. The development and benefits of thin layer models has been discussed, the efficiency provided by these models by eliminating the need to simulate the field inside material sheets has made previously unreasonably costly simulations viable. The popular edge based Maloney thin boundary has been presented and compared to the Flintoft face centred method using a spherical validation case produced by the author. The face centred method has been shown to increase the accuracy of magnitude of SE for the test case and reduced the presence of spurious resonances. The author has also proposed corrections to the face centred model to better simulate the field at the edges of surfaces consisting of SIBCs. These corrections have been shown to further improve on the accuracy of the spherical shell test case and a generic algorithm for dealing with different edge cases has been presented to allow for easy implementation.

## Chapter 3

# Errors due to Stair-casing in FDTD

A drawback of the basic Yee scheme is the difficulty in modelling structures that do not conform to the Cartesian grid. Curved surfaces, or flat surfaces that do not align to the grid, can be represented by a stepped surface as shown in Fig 3.1. This method is variously called stair-casing, saw-toothed, stepped or orthogonal meshing. Stair-cased meshing can be the cause of significant errors in FDTD simulation, however it is still a commonly used method due to its efficiency and straightforward implementation.

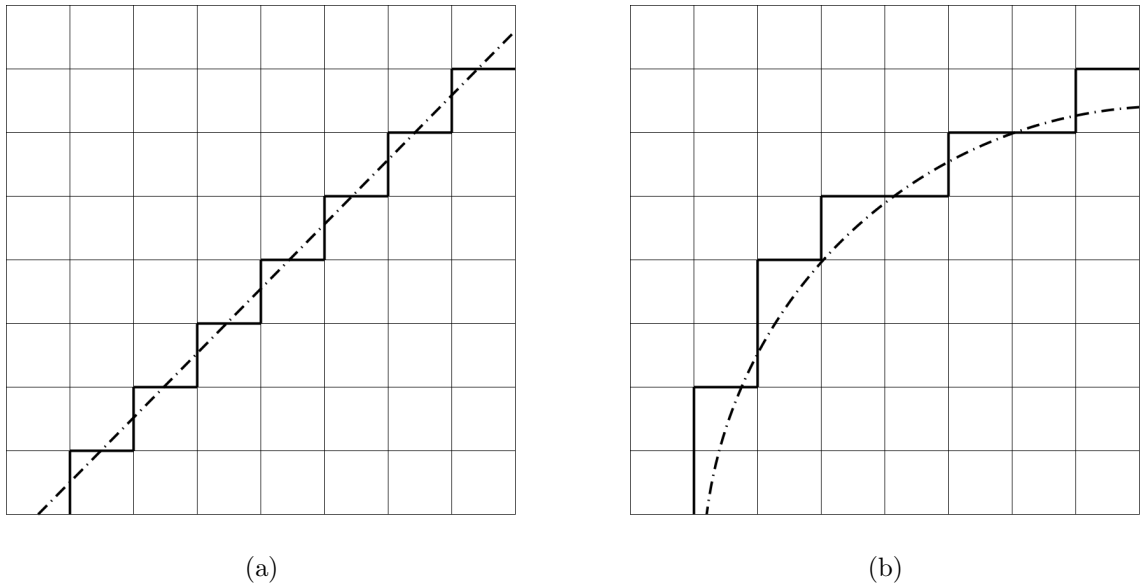


**Figure 3.1:** Stair-cased meshing of a flat surface (a) rotated  $45^\circ$  to the Cartesian grid and a curved surface (b).

### 3.1 Known Errors due to Stair-casing Meshing

Stair-casing has long been an issue for FDTD simulations as the errors are often poorly defined and in many publications stair-casing is noted as a generic source of error without in depth consideration. However, there have been some attempts to quantify errors due to stair-casing.

It has been determined [52] that numerical dispersion is introduced from the irregular surface by reducing the speed of the wave propagating along the 2D stair-cased meshes of straight Perfect Electric Conductor (PEC) walls. This delay is increased for coarser mesh sizes and higher frequencies. This is of particular concern for waveguide problems that are often used to simulate material sheets as they rely on straight PEC and Perfect Magnetic Conductor (PMC) walls. Further work considering dielectric materials[53] showed that increasing the permittivity of a stair-cased dielectric slab increases the error in reflection from a planar air-dielectric interface and that attenuation error converges to the air-PEC case as the relative permittivity is increased, making the air-PEC case a worst case scenarios.

A more advanced 2D PEC cylinder model has been used to demonstrate the effect of stair-cased meshing on scattering from curved surfaces [4]. It has been noted that the E-field closest to the surface of the boundary showed significant errors in magnitude. However, it was also noted that these errors were localised spatially and for cells at a distance from the surface the error was reduced significantly. The more commonly cited issue is that the errors in resonant frequencies of scattering from such a cylinder are exacerbated by stair-cased meshing. Although this error can be reduced by using a finer mesh, it has been concluded that the computational cost to achieve useful improvements in accuracy can be unreasonably computationally expensive[54].

A model of an conducting 2D cylinder has also been examined [55]. The intent of the work was to determine how the resonant frequency of the cylinder converged with respect to the size of the mesh. It was determined that for a stair-cased approximation the error in resonant frequency was proportional to the mesh size. However there were few data points provided in that paper and as such the results provided gave the impression of an *exact* proportional relationship between mesh size and error without consideration of errors introduced by differences in the staircase's mesh geometry caused by re-meshing for different mesh sizes.

Most existent work discussing stair-cased meshing and the associated errors use PEC material boundaries, this limits the range of scenarios that can be considered, mostly being scattering problems. There is also a focus on errors in resonant frequency, and it

is frequently noted that such errors can be accurately modelled using a stair-cased mesh with a suitably high resolution, little consideration is given to the frequency independent variation in the magnitude of reflection and transmission due to stair-cased meshing.

While much work on stair-casing focuses on the limitations of stair-cased meshing, there have been some attempts to provide corrections for the errors for specific problems such as TEM horn antennas [56, 57] and more generally by selective mesh generation [58]

There is a gap in the literature that discusses the effect of stair-casing on shielding problems. The rest of this chapter will explore the issue of stair-cased shielding cavities using the face centered SIBC model presented in Section 2.4.2.

## 3.2 Effect of Stair-casing on Shielding

This section will consider the effect of stair-casing on the shielding effectiveness (SE) of hollow cavities. Here, the SE of a cavity is defined as the ratio between the incident external electric field,  $E_{inc}$ , and the electric field,  $E_{int}$  at a point inside the cavity. SE is usually quoted in decibels and is given by (2.72).

### 3.2.1 Spherical Shell Test Case

Initially a spherical shell is considered as an analytic solution for the SE is available [3]. The curved surface of the shell requires a significant amount of stair-casing to represent on an orthogonal grid as can be seen in Fig 3.2. The mesh shown has been generated using an automated structured mesh generator [59].

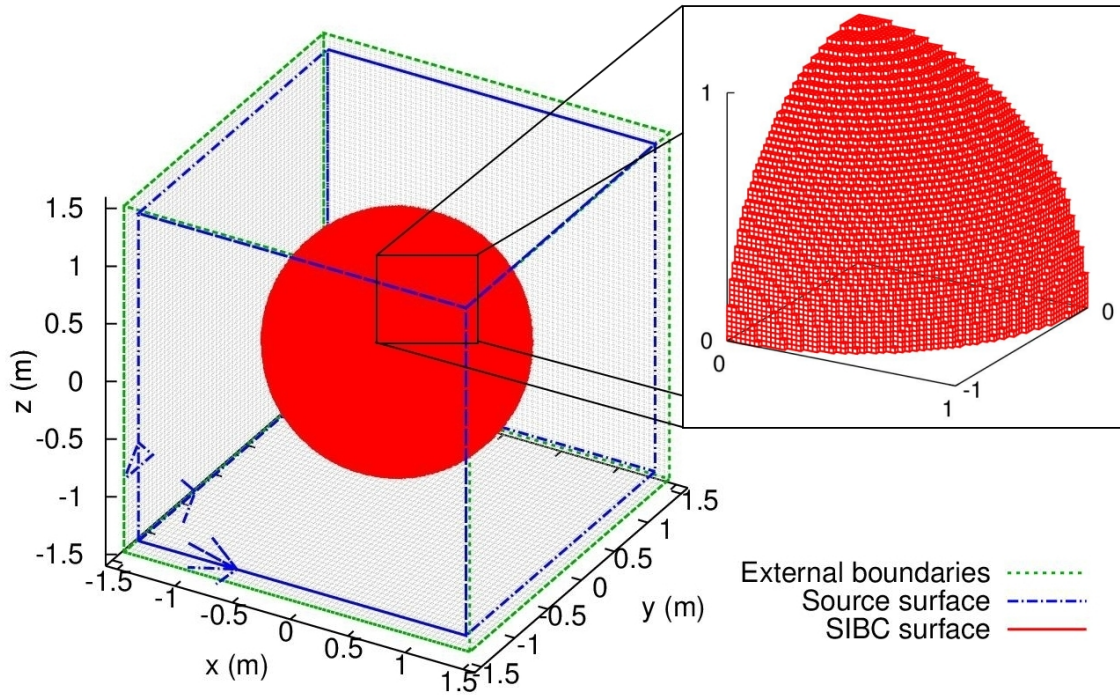


**Figure 3.2:** Model of a 1m radius hollow spherical shell made from a material with a conductivity of 1 KS/m that is 1mm thick. The shell is illuminated by a  $z$ -polarised plane wave. [1]

The spherical shell has a radius of 1m and a material thickness of 1mm. The shell is made from an isotropic material with a conductivity of 1 kS/m. The face centred thin layer model presented in Section 2.4.2 is used to represent the thin shell material for this model. The mesh size for this model is 20mm. The structure is illuminated by a linearly  $z$ -polarised plane-wave and the electric field at the centre of the sphere is recorded in order to determine the SE of the shell.

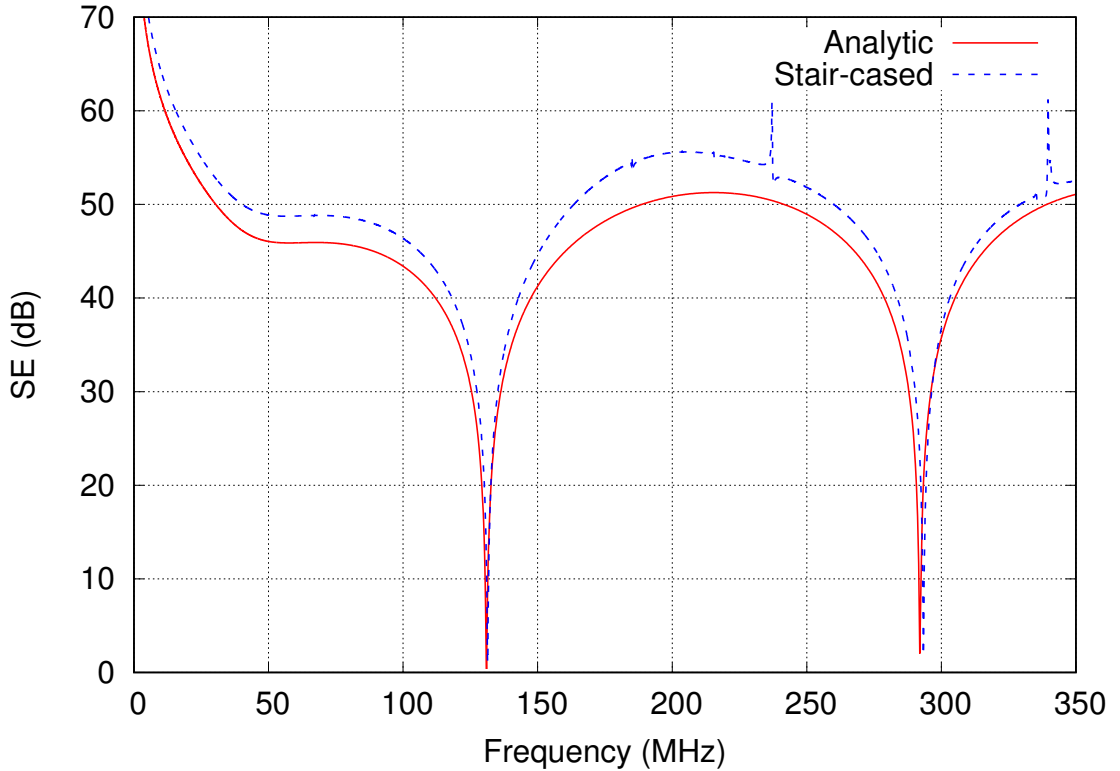


**Figure 3.3:** Shielding effectiveness at centre of a spherical cavity.

Figure 3.3 shows the results of the simulation in comparison to the analytic solution. There are a number of discrepancies between the simulated result and the analytic solution. The most commonly documented [60–62] error is in the value of the resonant frequencies. In Figure 3.3 the frequency of each resonance is approximately 0.5% too high; this error can be reduced by decreasing the mesh size; the effect of doing so is shown in Figure 3.5. However, reducing the mesh size will also increase the number of updates required for the simulation such that:

$$u \propto \frac{1}{\Delta x \Delta y \Delta z \Delta t} \quad (3.1)$$

where  $n$  is the number of iterations,  $\Delta x, \Delta y, \Delta z$  are the cell sizes in each Cartesian direction,  $u$  is the number of updates and  $\Delta t$  is the time step. Assuming a uniform grid, this means that halving the mesh size increases the number of updates (and hence the runtime of the simulation) by a factor of 16.

Unlike the thicker shell shown in Figure 2.7 the magnitude of the resonant spikes does not appear to change with frequency, this due to the fact that the skin depth for the frequency range of interest is greater than the thickness of the shell. Figure 2.9 shows skin depth as a function of frequency, the shell is 1mm thick.

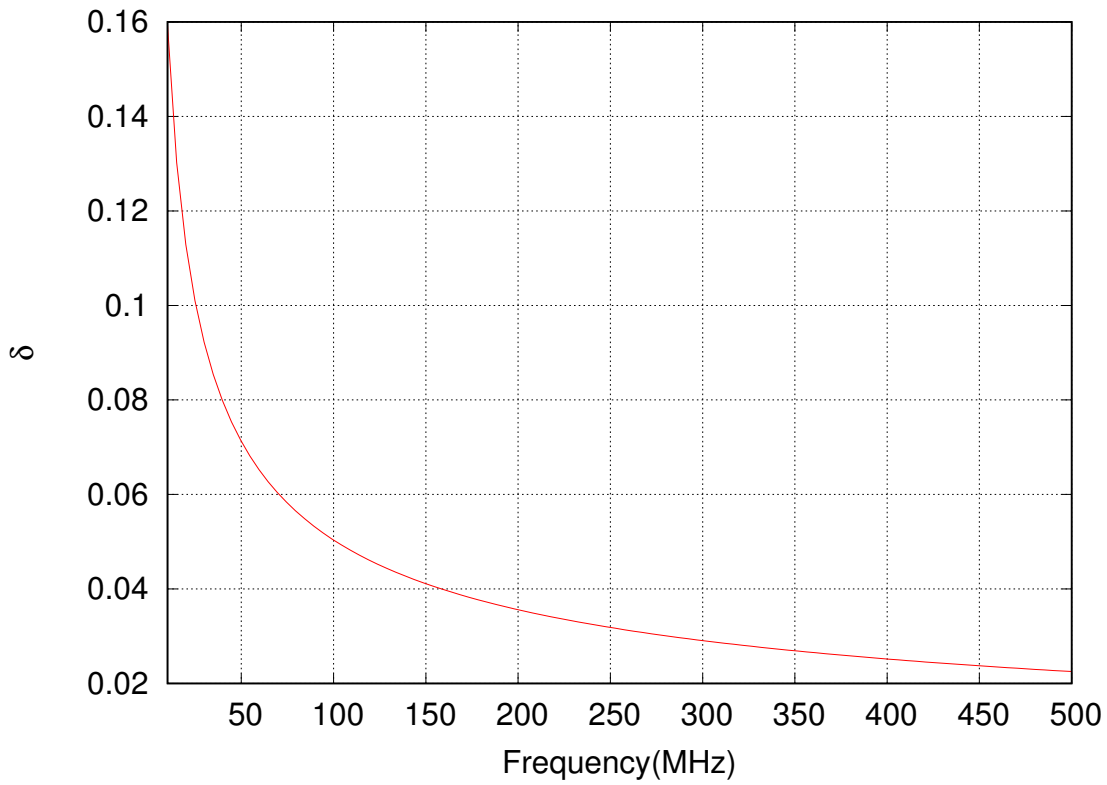


Figure 3.4: Skin depth  $\delta$  as a function of frequency for the problem set up in Figure 3.2

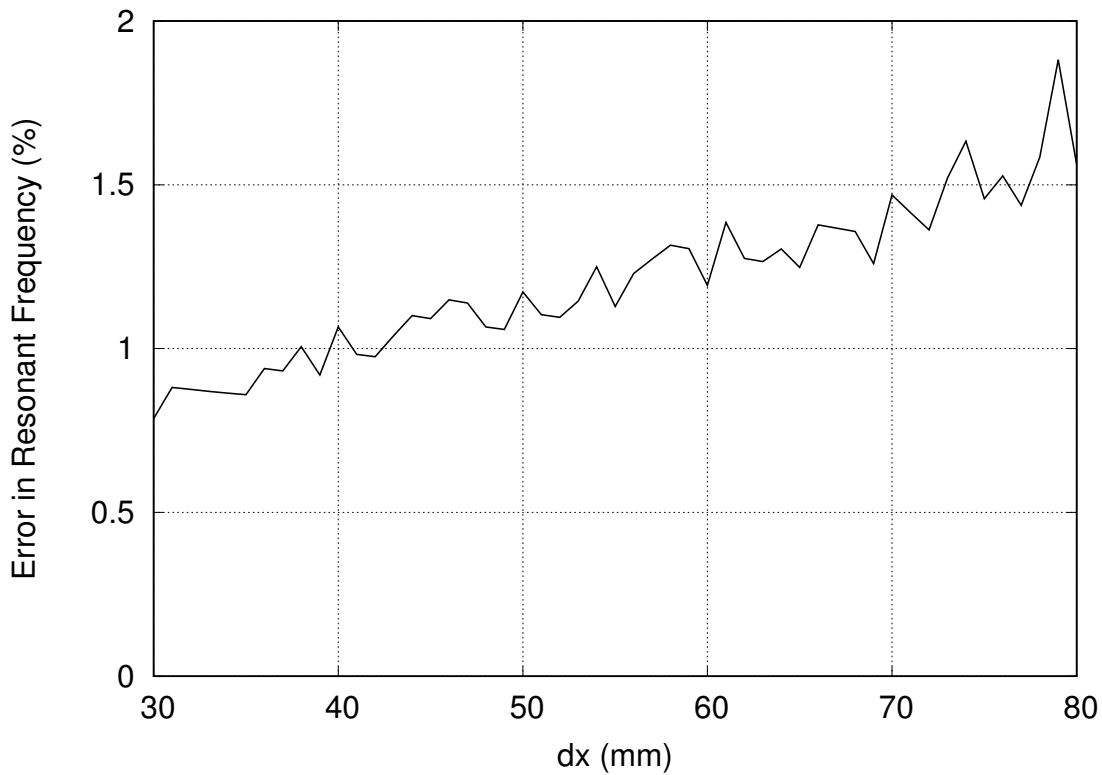
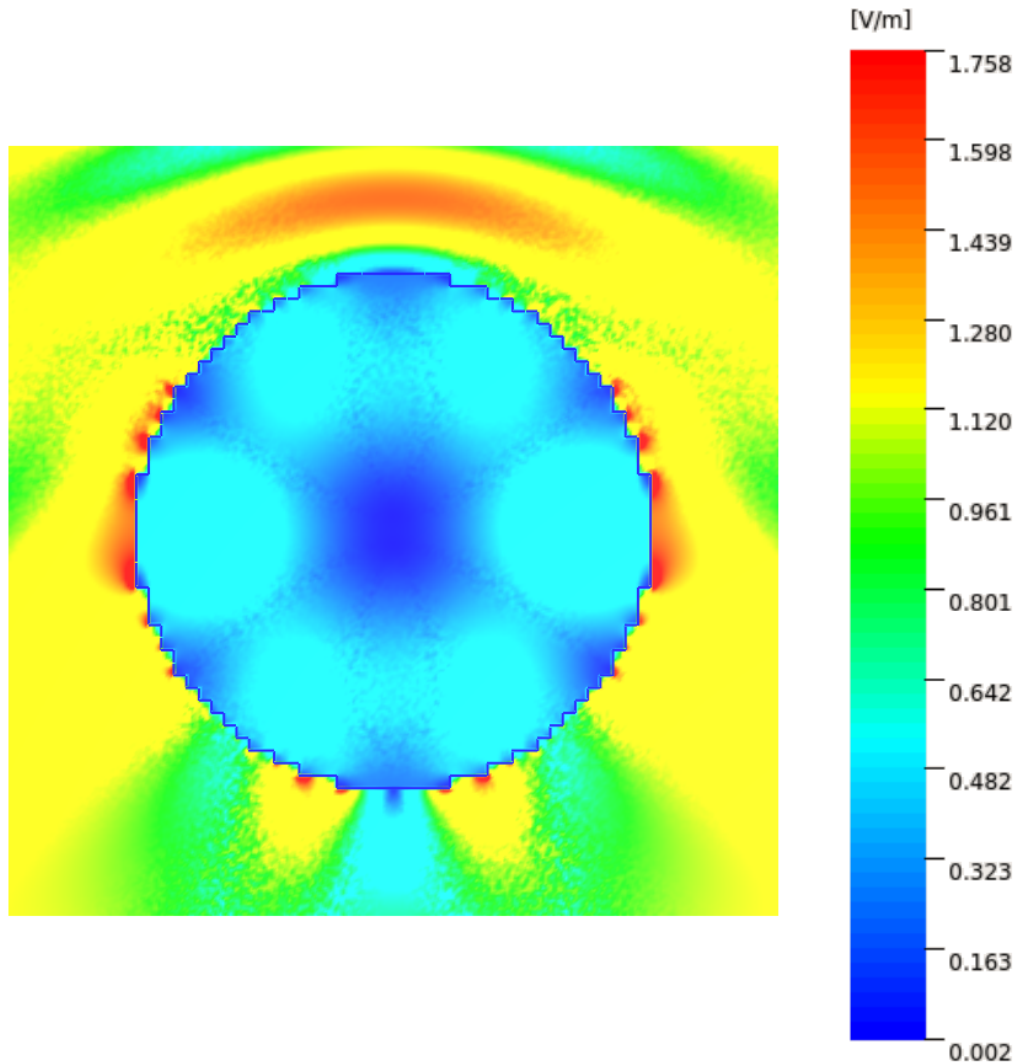


Figure 3.5: Error in resonant frequencies for a stair-cased shell using different mesh sizes.

It can also be seen in Figure 3.3 that there are resonances in the simulated results

that are not present in the analytic solution. These extra features correspond to those resonances that have a node at the centre of the sphere (i.e on the observation point). Figure 3.6 shows a cross section of the E-field across the sphere at 237.6MHz generated by the CONCEPT II, Method of Moments (MoM) based code [2] using a stair-cased mesh. This frequency matches the frequency of an unexpected resonant peak in Fig 3.3. The light areas correspond to field maxima inside the shell and the dark areas to low field values. At this frequency it can be seen that there is a node at the centre of the spherical shell.



**Figure 3.6:** Planar E-Field plot for a cross section of the inside of the sphere at 237.6 MHz simulated using CONCEPT II MoM software [2].

Figure 3.7 shows the magnitude of the electric field across the cavity, also at 327.6MHz. It can be seen that the electric field is greatly reduced near the centre, as would be expected at a node. However at the exact centre there is an increase in magnitude in both lines; in the FDTD case the increase is larger than in the MoM solution. The analytical solution

assumes a mathematically perfect sphere, which has a node at the centre. However, for both the structured and unstructured meshes a numerical approximation of a sphere is used; the field at the centre of the sphere is highly sensitive to changes in the structure of the sphere.

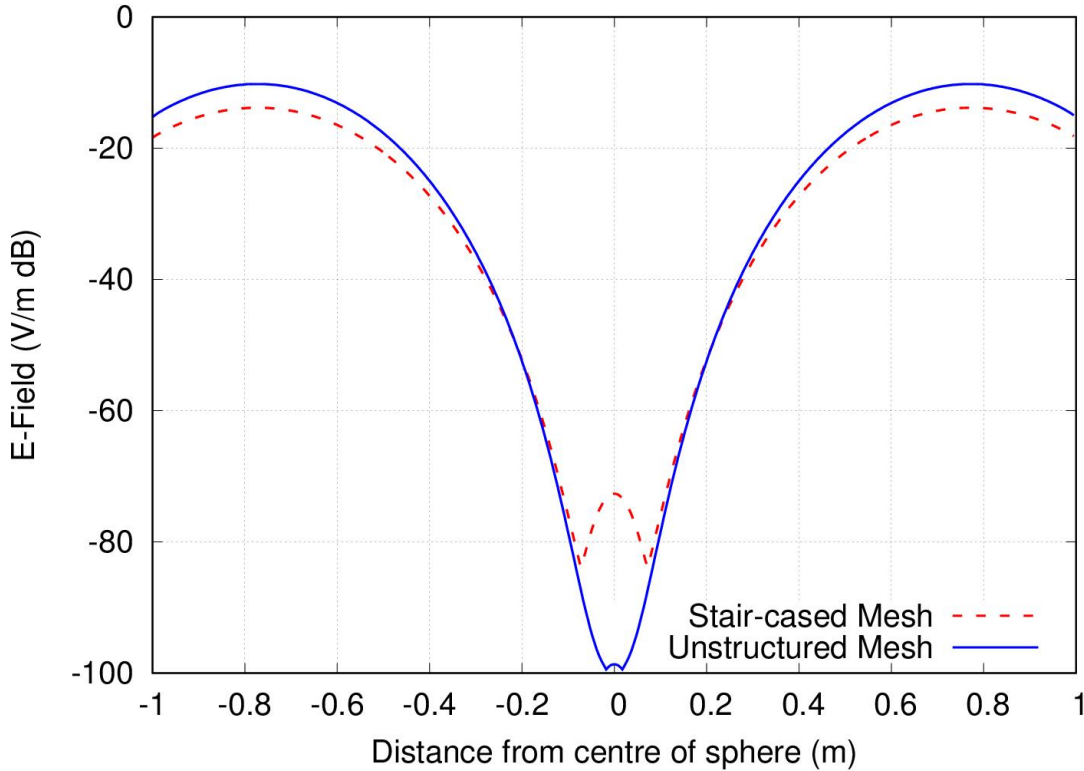


**Figure 3.7:** E-field along 1D across the spherical cavity at 237.6MHz. The unstructured mesh using CONCEPT II MoM software [2]

The last obvious error in Figure 3.3 is that the magnitude of the simulated SE is consistently about 3 dB higher than the analytic solution. As a result of using a stair-cased approximation to represent the sphere, the effective surface area of the shell is higher than the surface area of the analytic sphere. It was suspected that the error in SE was related to the error in surface area, which depends on the mesh size used. The simulation was repeated using different mesh sizes and compared the error in surface area of the shell to the error in magnitude of the SE as shown in Fig 3.8. It is apparent that the two errors are correlated.

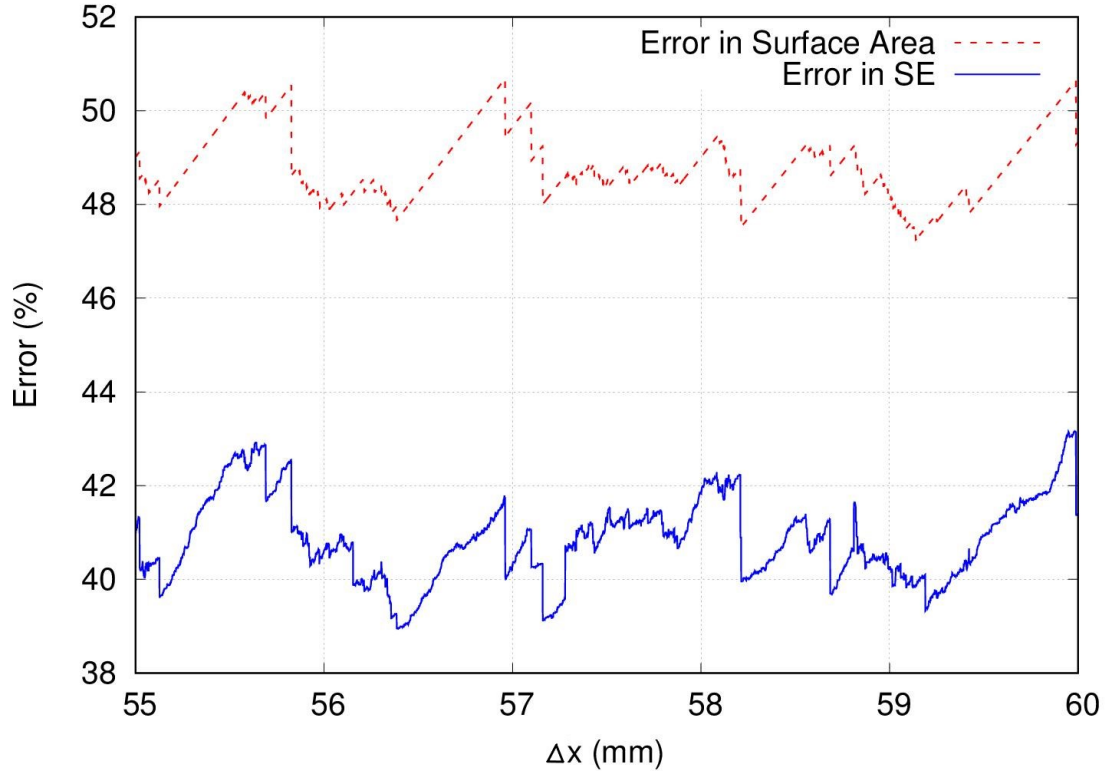


**Figure 3.8:** Comparison of the effective surface area of the stair-cased spherical shell and the error in magnitude of SE.

Unlike the error in the resonant frequency, the error in surface area cannot be improved by reducing the mesh size. The error in surface area is consistently around 49 % regardless of the mesh size used. As a result of this the error in magnitude of SE cannot be improved by reducing the mesh size.

### 3.2.2 Cubic Shell Test Case

The spherical shell is highly stair-cased, but it is also rotationally invariant. This means that the meshing of the sphere is not affected by its orientation in relation to the FDTD grid. To further test the use of a correction factor, a cubic cavity is investigated. Ordinarily a single cuboid structure could be made to align with the FDTD grid, in this case there would be no stair-casing errors. However if the cube is rotated with respect to the grid, as shown in Figure 3.9, then stair-casing is required to represent those surfaces that are no longer aligned. The shell of the cube is constructed of the same conductive material as in the spherical test case and has the same thickness.

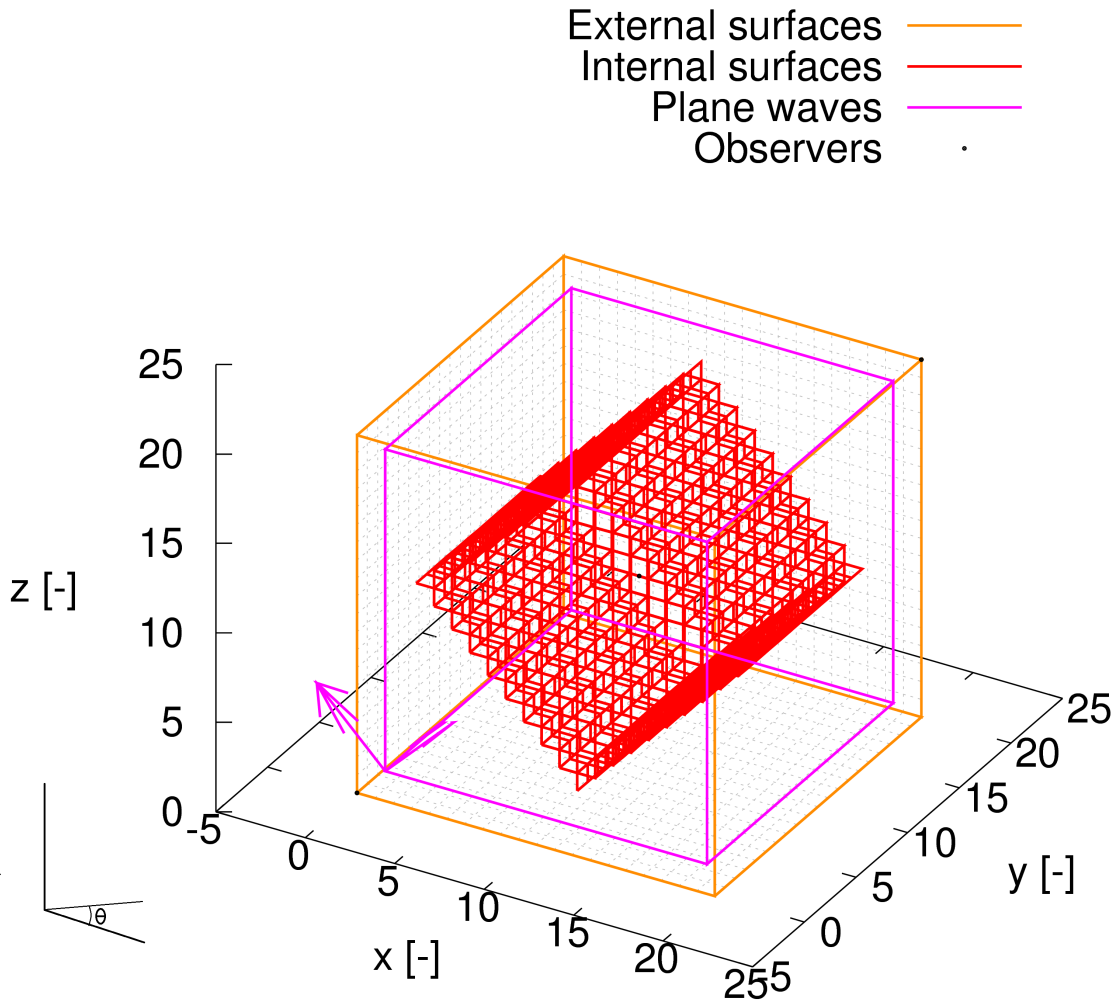


**Figure 3.9:** Set-up of a 1 m hollow cubic shell made from a material with a conductivity of 1 kS/m that is 1 mm thick. The shell is illuminated by a polarised plane wave.

The cube is rotated around a single axis, this causes four of the faces to no longer be aligned with the grid and require a stair-cased approximation. The extra surface area for a stair-cased face can be determined by considering the coarse and fine stair-cased approximations of a line as shown in Figure 3.10.

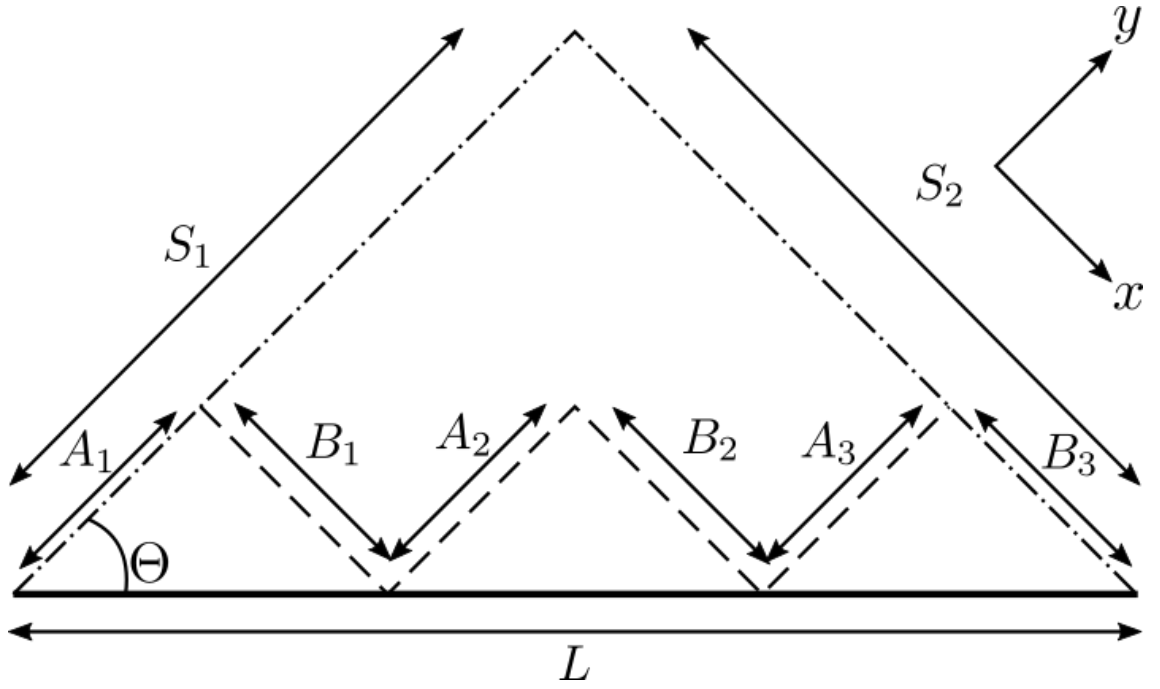


**Figure 3.10:** Coarse (Dot Dashed) and fine (Dashed) stair-cased approximations of a straight line (Solid)

The length of the coarse stair-cased approximation is the same as the length of the fine stair-cased approximation and is given by:

$$S_1 = \sum_{i=1}^n A_i, \quad S_2 = \sum_{i=1}^n B_i \quad (3.2)$$

Where  $S_1$  and  $S_2$  are the lengths of the  $y$ - and  $x$ -orientated sides of the coarse approximation respectively.  $a_i$  and  $b_i$  are the lengths of the  $y$  and  $x$  orientated sides of the fine approximation respectively. The two sides of the coarse stair-cased approximation can be related to the length of the original line  $L$  by:

$$S_1 = L \cos \Theta, \quad S_2 = L \sin \Theta \quad (3.3)$$

Where  $\Theta$  is the angle of rotation of the line to the orthogonal grid. And therefore the length of a stair-cased approximation of a flat surface in 2D is given by:

$$S = S_1 + S_2 = L(\cos \Theta + \sin \Theta) \quad (3.4)$$

The total error ( $\epsilon$ ) in surface area of the meshed cube due to the stair-cased faces is therefore given by:

$$\epsilon = L(\cos \Theta + \sin \Theta - 1) \quad (3.5)$$

It is worth noting that (3.4) does not depend on the cell size and therefore the error in surface area cannot be improved by using a higher resolution mesh.

### 3.3 Effect of Stair-casing on Scattering

Where the previous example considers the effect of stair-casing on shielding problems, scattering from stair-cased surfaces is also of interest. This section details two scattering cases, the first is a cubic shell to demonstrate scattering from planar surfaces and sharp corners. The second case is a spherical shell with a doubly curved symmetrical surface. To measure the scattering from the shells the field is recorded on a cubic surface near the boundaries of the problem space. A far field transformation is then applied to the field to determine the field at a distant point from the cavity.

#### 3.3.1 Cubic Shell Test Case

The first scattering test case is a hollow cubic shell. This is identical to the cube shielding test case in Section 3.2.2. In this case the scattering from the shell was recorded and Figure 3.11 shows the far field E-Field in the YZ plane centred at the centre of the cube. Comparisons are made between a cube rotated  $45^\circ$  to the grid using both a stair-cased and conformal mesh with a cube aligned to the grid. The angle  $\Theta$  refers to the angle of scattering where  $180^\circ$  is a reflection along the normal to the angle of incidence. It can be seen that the stair-cased mesh produces a result with significant variation in comparison to the aligned case, this is most apparent near the resonances where the sharp spike of the resonance is no longer present. It is possible that this is due to reflections from the stair-cased sides of the cube the would be otherwise parallel to the propagation vector and therefore have minimal reflection.

Away from the resonance there is a clear magnitude error of 2 dB at  $\Theta = 180$  and -2.6 dB at  $\Theta = 0, 360$ . Unlike for the shielding problems, this is not a case of the magnitude being shifted uniformly in one direction as the error is negative when  $\Theta = 0, 360$  and positive when  $\Theta = 180$

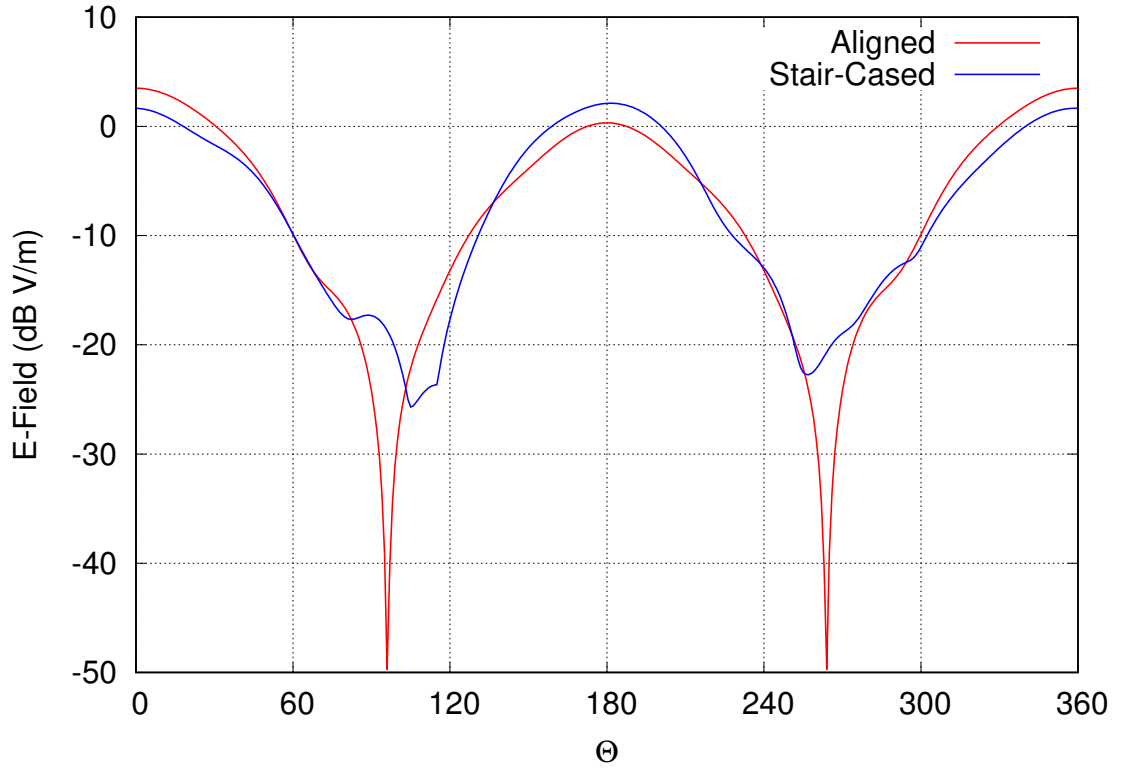


**Figure 3.11:** Scattering from the cubic cavity, rotated  $45^\circ$  with respect to the mesh, in the  $yz$ -plane comparing non-conformal and conformal meshes to an aligned cube solution.

### 3.3.2 Spherical Shell Test Case

The spherical test case used for the scattering analysis is the same as the one used for the shielding problem in Section 3.2.1. Figure 3.12 shows the recorded far field scattering of the E-field in the YZ plane from the sphere. Again at  $\Theta = 180$  the angle of scattering is directly back along the direction of propagation for the incident wave. It can be seen in Figure 3.12 that the magnitude of the scattered field for the main peak is too high with an error of approximately 2 dB. It also appears that the subsidiary peaks are greatly magnified causing significant errors that exceed 5 dB in some cases.

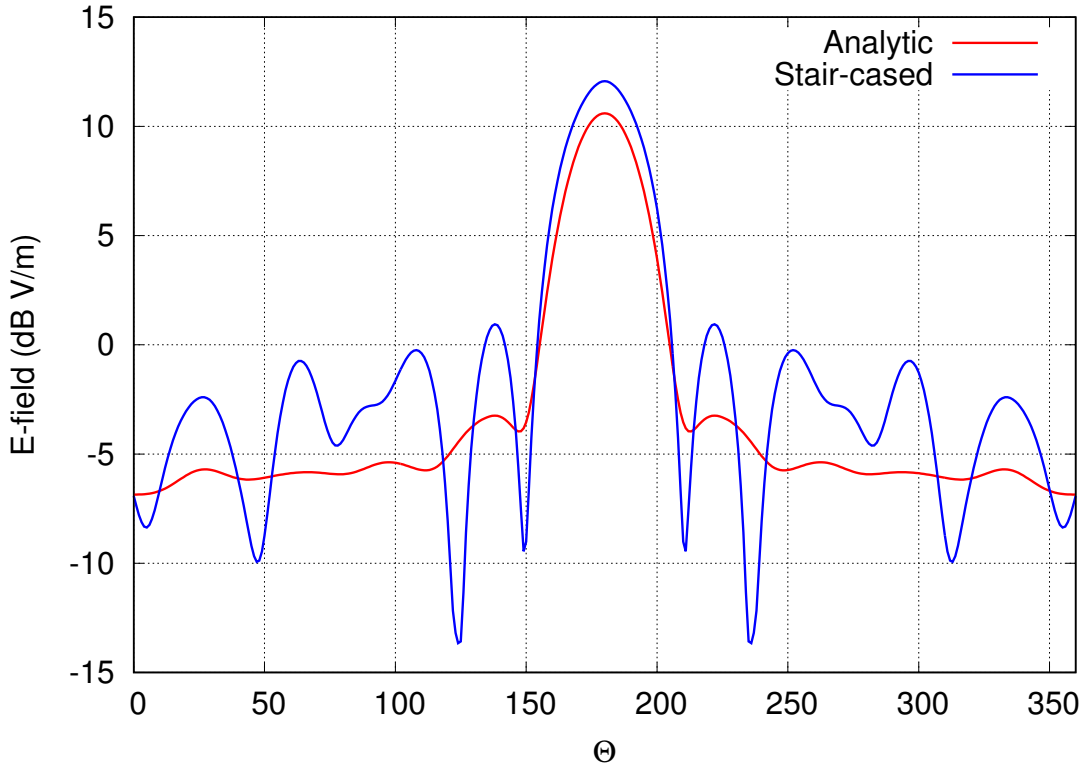


**Figure 3.12:** Scattering from the spherical cavity in the  $yz$ -plane comparing a stair-cased FDTD simulation to an analytic solution. [3]

### 3.4 Summary

Stair-casing is a recognised and widely known source of error in FDTD simulations. A brief discussion of previous work on stair-casing errors has been made. However, these studies are mostly limited to PEC materials and scattering problems.

New work has been presented that examines the effects of stair-cased meshing on shielding problems for cavities. Errors in the resonant frequency of cavities have been associated with inaccuracies in the physical position of boundary nodes relative to the analytic surface. Similarly, the presence of apparently spurious resonances have been identified as being caused by resonant nodes being shifted spatially due to the inaccurate boundary positioning. Both the error in resonant frequency and spurious resonances can be reduced by using a finer mesh as the error in boundary positioning will be reduced.

Errors in the magnitude of SE has been linked directly to the increase in surface area caused by stair-casing, the error in surface area is prone to only minor variations due to changes in mesh size and otherwise the error in area is constant, therefore the error in the magnitude of SE cannot be improved by using a finer resolution mesh.

There has also been testing of the effect of stair-casing on scattering problems. These tests have focused on the magnitude of scattering rather than frequency shifting as has

been examined in previous works. Two cases were presented, a cube and a sphere. For the cube case, sharp resonances have been shown to become ill defined using a stair-cased mesh, this has been attributed to reflections from a stair-cased surface that would be otherwise orthogonal to the plane wave and therefore have minimum reflection. The second case was of a spherical shell. In this case there is a more complex scattering structure that is replicated by the stair-cased result, but has significant errors in magnitude.



## Chapter 4

# Correcting the Transmittance of SIBCs

In Chapter 3 it is shown that the length of a stair-cased surface is given by:

$$A = L(\cos\Theta + \sin\Theta) \quad (4.1)$$

where  $L$  is the length of the surface being meshed,  $\Theta$  is the angle of the surface to the mesh and  $A$  is the length of the stair-cased surface. This chapter shows how the length of the stair-cased surface affects the sheet resistance of a material and subsequently the magnitude of the transmission and reflection of incident waves upon the surface. The magnitude of the error is determined and a correction factor is proposed to alter the transmission and reflection coefficients of stair-cased boundaries to cancel out the errors caused by the stair-cased mesh.

### 4.1 Stair-casing and Sheet Resistance

Sheet resistance is an electrical property used to describe the resistivity of thin materials of uniform thickness. Consider Figure 4.1, the sheet resistance is a measure of the resistivity across the thickness  $t$  of the material.

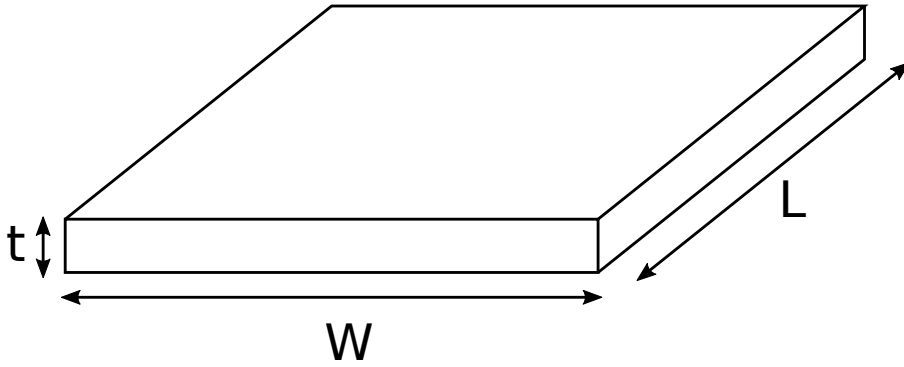


**Figure 4.1:** Geometry used to define sheet resistance. The polarisation of the electric field aligns with the axis of the length  $L$ .

The sheet resistance is given by:

$$R = \psi \frac{L}{Wt} \quad (4.2)$$

where  $\psi$  is the material resistivity,  $L$  is the length of the sheet along the same axis as the E-field polarisation of an incident field,  $t$  is the thickness of the sheet and  $W$  is the width of the sheet.

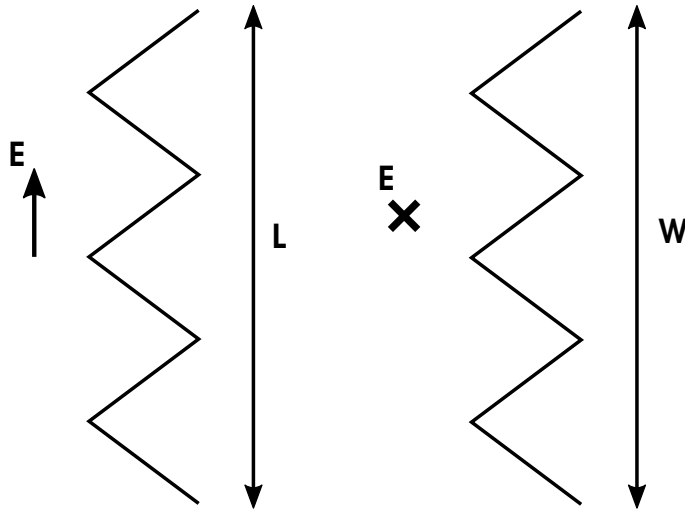


**Figure 4.2:** Geometry of sheet resistance for different orientations of stair-cased mesh.

In the case that a surface such as that shown in Figure 4.1 is modelled using a stair-cased mesh, either the effective width or effective length will be increased depending on the polarisation of the incident electric field. Figure 4.2 shows the effect of stair-casing for different polarisations, In the case that the stair-casing increases the distance along the electric field axis the effective length, according to (4.1), will be increased by a factor of:

$$\cos \Theta + \sin \Theta \quad (4.3)$$

where  $\Theta$  is the angle between the surface and the mesh. This would make the sheet

resistance equation (4.2) become:

$$R = \psi \frac{L(\cos \Theta + \sin \Theta)}{Wt} \quad (4.4)$$

therefore increasing the sheet resistance. A higher sheet resistance means that the reflection coefficient for an incident electromagnetic wave from the surface of the sheet will be increased and the transmission through the sheet will be decreased.

Similarly, if the stair-casing increases the sheet length perpendicular to the incident electric field the width will increase leading to a sheet resistance equation of:

$$R = \psi \frac{L}{Wt(\cos \Theta + \sin \Theta)} \quad (4.5)$$

leading to a reduced sheet resistance. A reduced sheet resistance will cause a lower reflection coefficient and a higher transmission coefficient.

## 4.2 Proposed Algorithm

Here it is proposed that, once it is known by how much the transmission and reflection coefficients of a stair-cased sheet have been altered, the error can be corrected by adjusting the coefficients of the sheet to compensate.

For the polarisation where the stair-casing increases the sheet resistance of the boundary the transmission factor is too high so that the effective transmission factor  $\tau_e$  is given by:

$$\tau_e = \tau_o(\cos \Theta + \sin \Theta) \quad (4.6)$$

where  $\tau_o$  is the transmission coefficient of the non stair-cased material. By changing the coefficient  $\tau_o$  to a corrected coefficient  $\tau_c$  calculated by:

$$\tau_c = \frac{\tau_o}{(\cos \Theta + \sin \Theta)} \quad (4.7)$$

The effective transmission due to stair-casing would be given by:

$$\tau_e = \tau_c(\cos \Theta + \sin \Theta) = \frac{\tau_o(\cos \Theta + \sin \Theta)}{(\cos \Theta + \sin \Theta)} = \tau_o \quad (4.8)$$

This makes the effective transmission equal to the non-stair-cased transmission removing the error in transmission due to the stair-cased mesh. For the polarisation where the stair-casing reduces the sheet resistance a similar process can be carried out. Where the effective transmission coefficient  $\tau_e$  is given by:

$$\tau_e = \frac{\tau_o}{(\cos \Theta + \sin \Theta)} \quad (4.9)$$

So by applying a corrected transmission coefficient  $\tau_c$ :

$$\tau_c = \tau_o(\cos \Theta + \sin \Theta) \quad (4.10)$$

the effective transmission coefficient becomes:

$$\tau_e = \frac{\tau_c}{(\cos \Theta + \sin \Theta)} = \frac{\tau_o(\cos \Theta + \sin \Theta)}{(\cos \Theta + \sin \Theta)} = \tau_o \quad (4.11)$$

Once again the effective transmission is equal to the non-stair-cased transmission removing the error due to the stair-cased mesh.

As mentioned earlier, the reflection coefficient of the material sheet is also affected by the changes in the sheet resistance due to the stair-cased meshing. It was determined empirically that the total magnitude of the transmitted and reflected waves remained constant such that:

$$\tau_o + \rho_o = \tau_e + \rho_e \quad (4.12)$$

Substituting (4.6) gives:

$$\tau_o + \rho_o = \tau_o(\cos \Theta + \sin \Theta) + \rho_e \quad (4.13)$$

Which can be rearranged to:

$$\tau_o + \rho_o = \tau_o + \tau_o(\cos \Theta + \sin \Theta - 1) + \rho_e \quad (4.14)$$

Therefore the effective reflection coefficient must be given by:

$$\rho_e = \rho_o - \tau_o(\cos \Theta + \sin \Theta - 1) \quad (4.15)$$

To correct the effective reflection coefficient it must be made equal to the reflection coefficient of the non stair-cased material, such that:

$$\rho_c = \rho_o - \tau_o(\cos \Theta + \sin \Theta - 1) + \tau_o(\cos \Theta + \sin \Theta - 1) \quad (4.16)$$

or:

$$\rho_c = \rho_e + \tau_o(\cos \Theta + \sin \Theta - 1) \quad (4.17)$$

Similarly, in this form the corrected transmission coefficient is given by:

$$\tau_c = \tau_e - \tau_o(\cos \Theta + \sin \Theta - 1) \quad (4.18)$$

Rearranging (4.17) and (4.18) to get the effective values and substituting into (4.12) into it can be shown that:

$$\tau_o + \rho_o = \tau_c + \tau_o(\cos \Theta + \sin \Theta - 1) + \rho_c - \tau_o(\cos \Theta + \sin \Theta - 1) \quad (4.19)$$

Which can be reduced to:

$$\tau_o + \rho_o = \tau_c + \rho_c \quad (4.20)$$

Where  $\rho_o$  is the reflection coefficient on the non stair-cased material and  $\rho_c$  is the corrected reflection coefficient. By substituting the corrected transmission factors (4.7) and (4.10) into (4.20) the corrected reflection coefficients for higher sheet resistance can be determined by:

$$\rho_c = \rho_o + \tau_o \left(1 - \frac{1}{\cos \Theta + \sin \Theta}\right) \quad (4.21)$$

and lower sheet resistance:

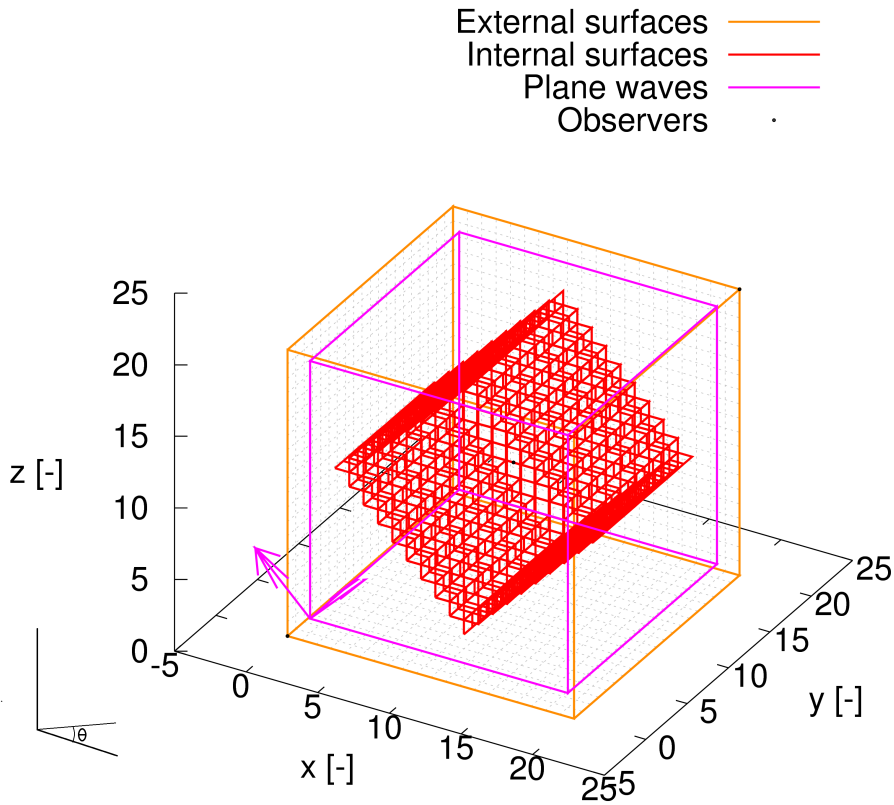
$$\rho_c = \rho_o + \tau_o (1 - (\cos \Theta + \sin \Theta)) \quad (4.22)$$

### 4.3 Validation

In this section two test cases are presented. The first uses a cubic hollow shell to test the correction factor method for planar surfaces rotated around a single axis. The second test case is an infinite cylindrical shell using multiple correction factors to represent a singly curved surface.

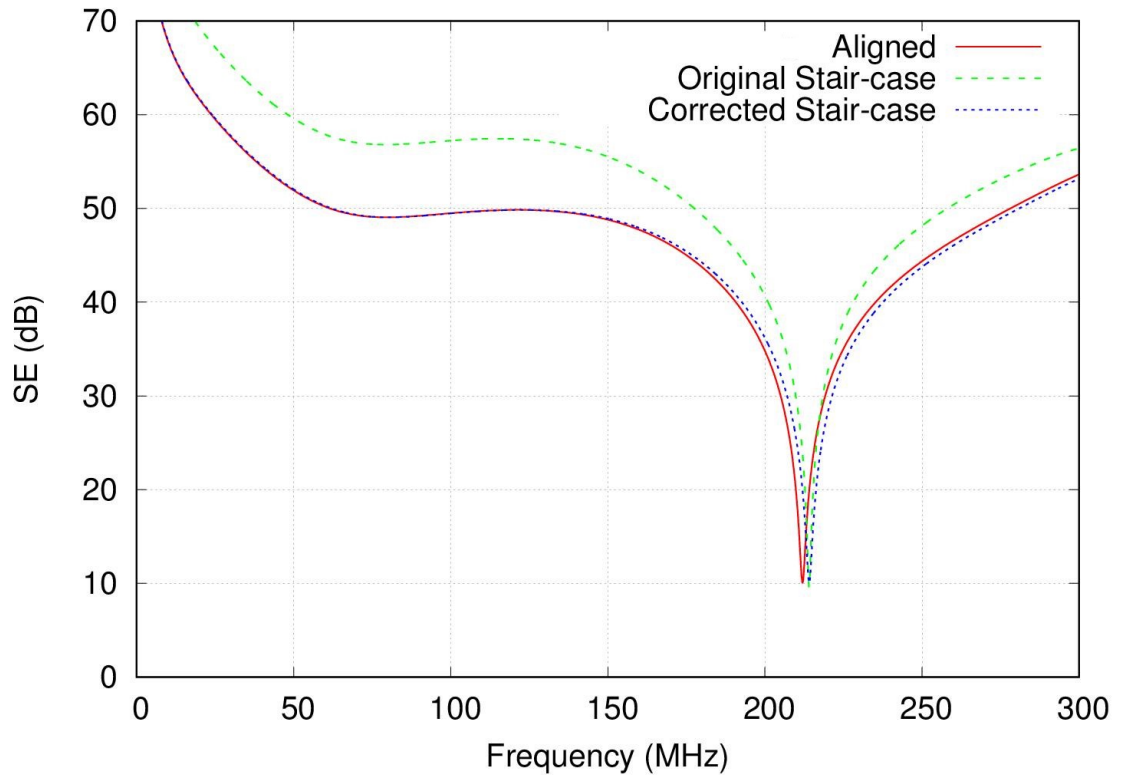
#### 4.3.1 Cubic Shell Test Case

Figure 4.3 shows the stair-cased mesh of hollow 1 m cubic shell that has been rotated  $45^\circ$  around the  $y$ -axis. This material of the shell is represented using an SIBC with a frequency independent transmission coefficient of 0.004 and a reflection coefficient of 0.99. The cube is illuminated by a  $y$ -polarised plane wave. It is possible to mesh the cube so that it is aligned to the axes of the simulation grid and this would remove the need for stair-cased mesh. For this case there is no analytic solution to the shielding effectiveness of the cube so the result from the aligned case is used for comparison.



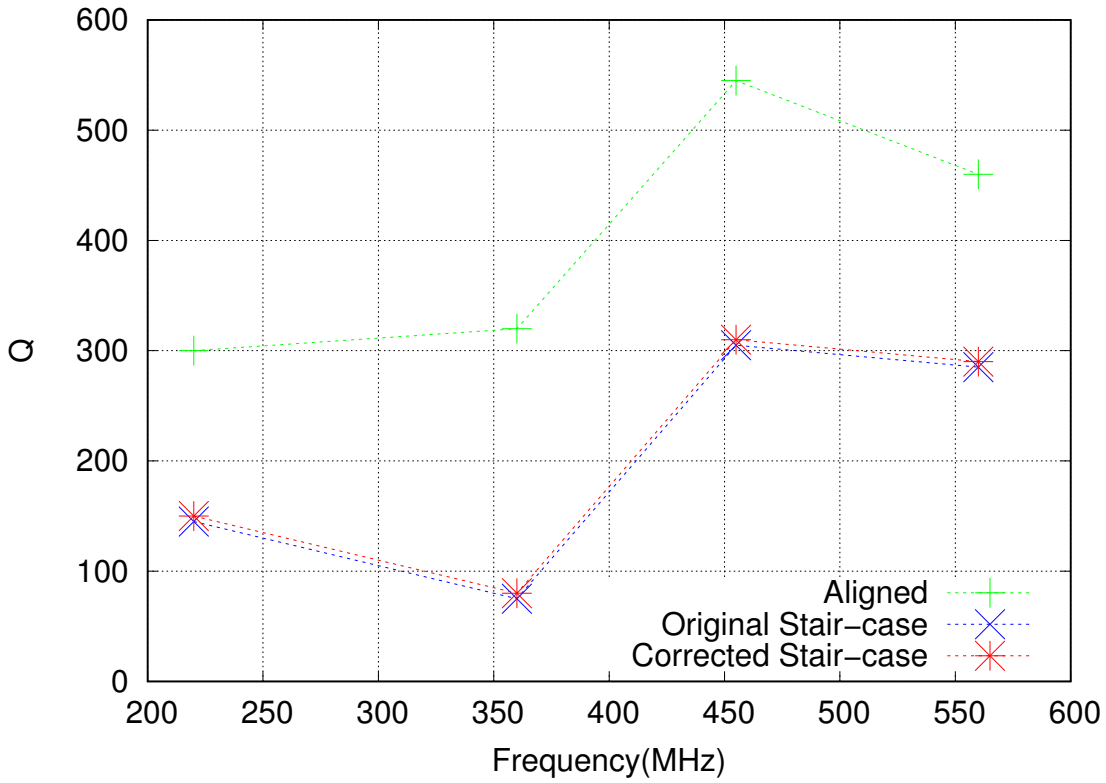
**Figure 4.3:** Set-up of a 1 m hollow cubic shell made from a material with a transmission coefficient of 0.004 and a reflection coefficient of 0.99. The shell is illuminated by a polarised plane wave. This is identical to the mesh shown in Figure 3.9

Figure 4.4 shows the SE at the centre of the simulated cube. It can be seen that when using the proposed corrected transmission and reflection coefficients the magnitude of the shielding that is recorded is significantly closer to the aligned case than when using the original coefficients. The error at 100MHz is approximately 7 dB for the original mesh, this has been reduced to less than 0.1dB for the corrected mesh. This frequency was chosen to be away from a resonance so as to minimise the effect of frequency shift. It should be noted here that the geometry of the mesh has not changed in any way and as a result the shift in frequency that occurs as a result of stair-cased meshing is not altered using the correction factor, this can be seen in Figure 4.3 around the resonant frequency.



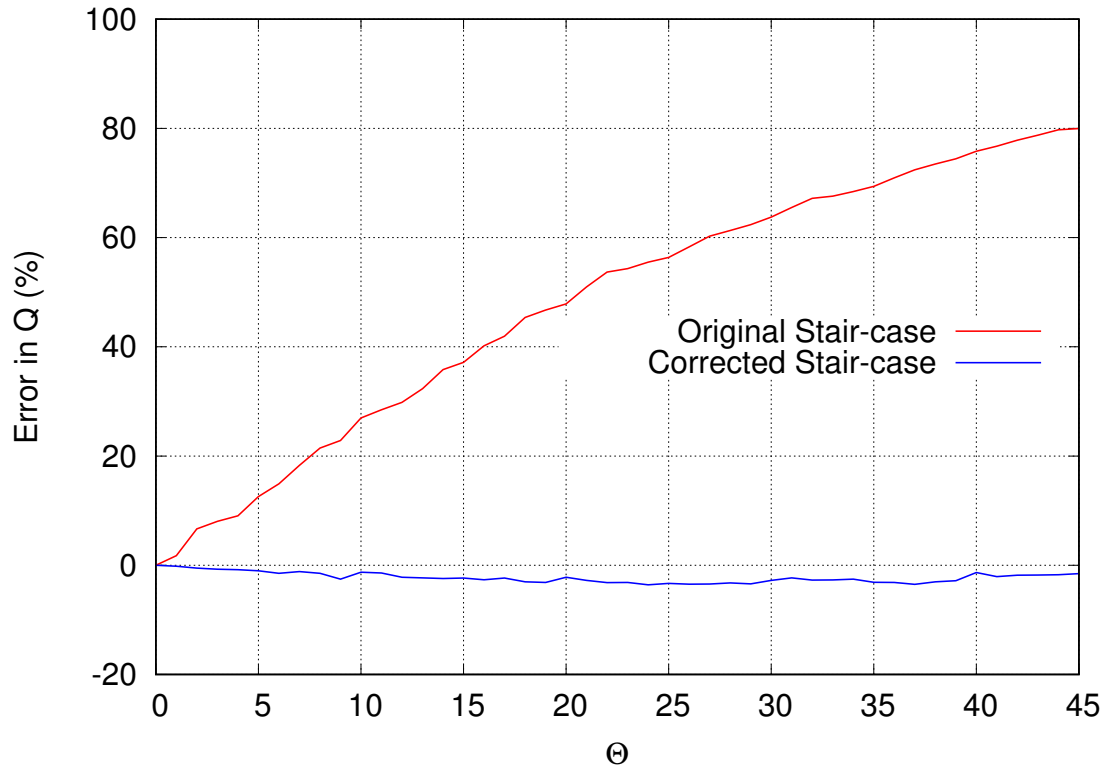
**Figure 4.4:** SE at the centre of a stair-cased cubic shell, with and without a correction factor applied compared to a non stair-cased model.

To further validate the correction factor method the Q-factor for each of the first four resonant frequencies was calculated from the shape of the resonant peaks of the E-field at the centre of the cube. Figure 4.5 shows the calculated Q-factors. It can be seen that for the original stair-cased mesh the Q-factor is too high, using the corrected coefficients has reduced this error significantly.



**Figure 4.5:** Q-factor of first four resonances at the centre of a stair-cased cubic shell, with and without a correction factor applied compared to a non stair-cased model.

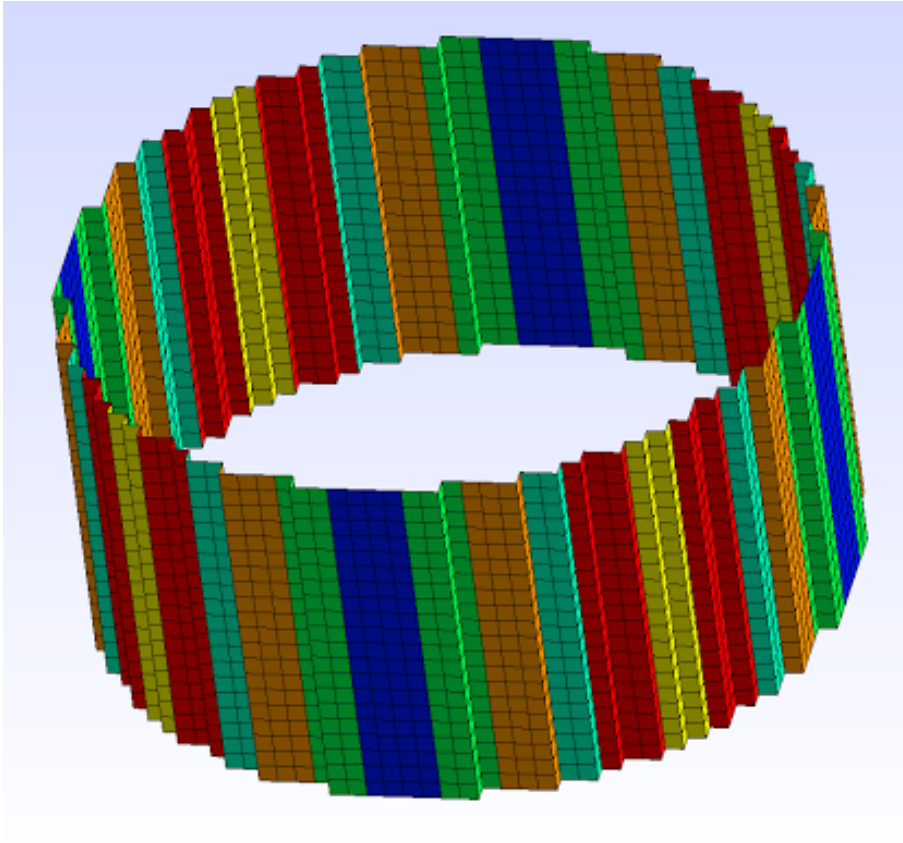
The proposed correction should work at any angle of rotation. Figure 4.6 shows the error in the Q of the first resonant frequency using the original stair-cased mesh for different angles of rotation. As expected, the error is highest for rotations of  $45^\circ$  as this involves the largest difference in effective edge length. Using the correction factor has reduced the error from as high as 85% to less than 5%. For all angles the error is smaller when using the correction factor.



**Figure 4.6:** Error in the Q-factor of the first resonance of a stair-cased cubic shell with and without a correction factor applied. Error is relative to a non stair-cased model.

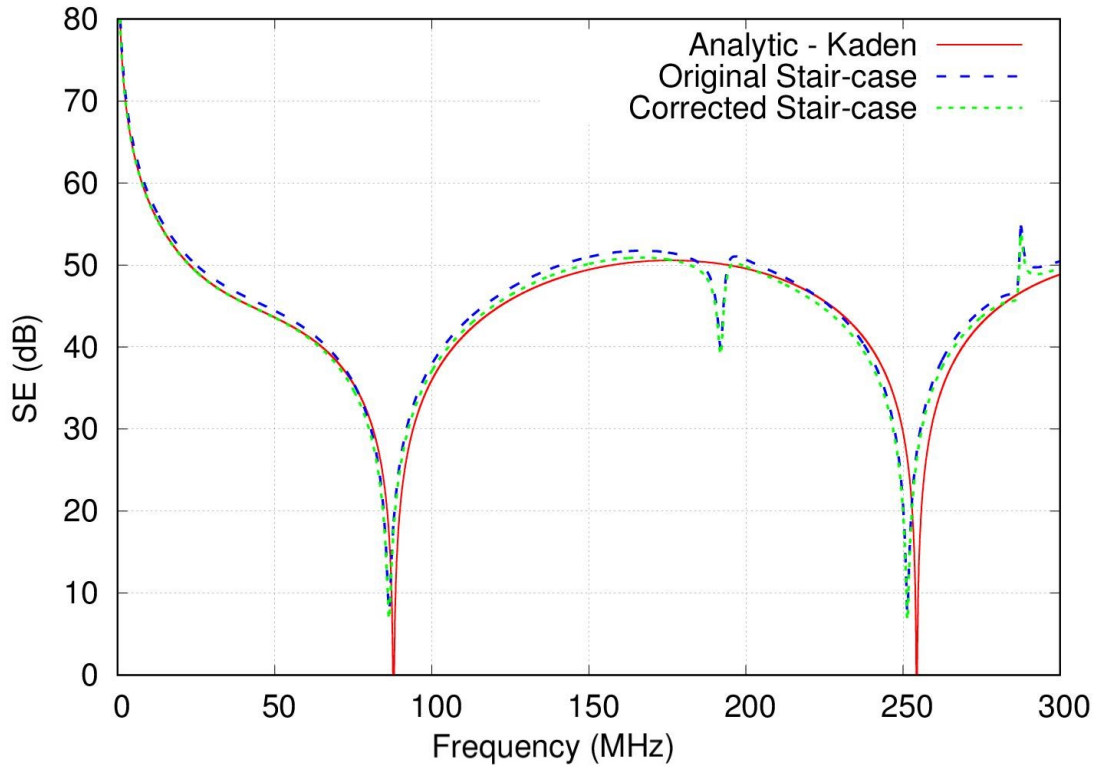
### 4.3.2 Cylindrical Shell Test Case

The second test case is an infinite cylindrical shell. This case is used to demonstrate that applying different correction factors on a curved stair-cased surface can be used to correct the error in transmission and reflection.



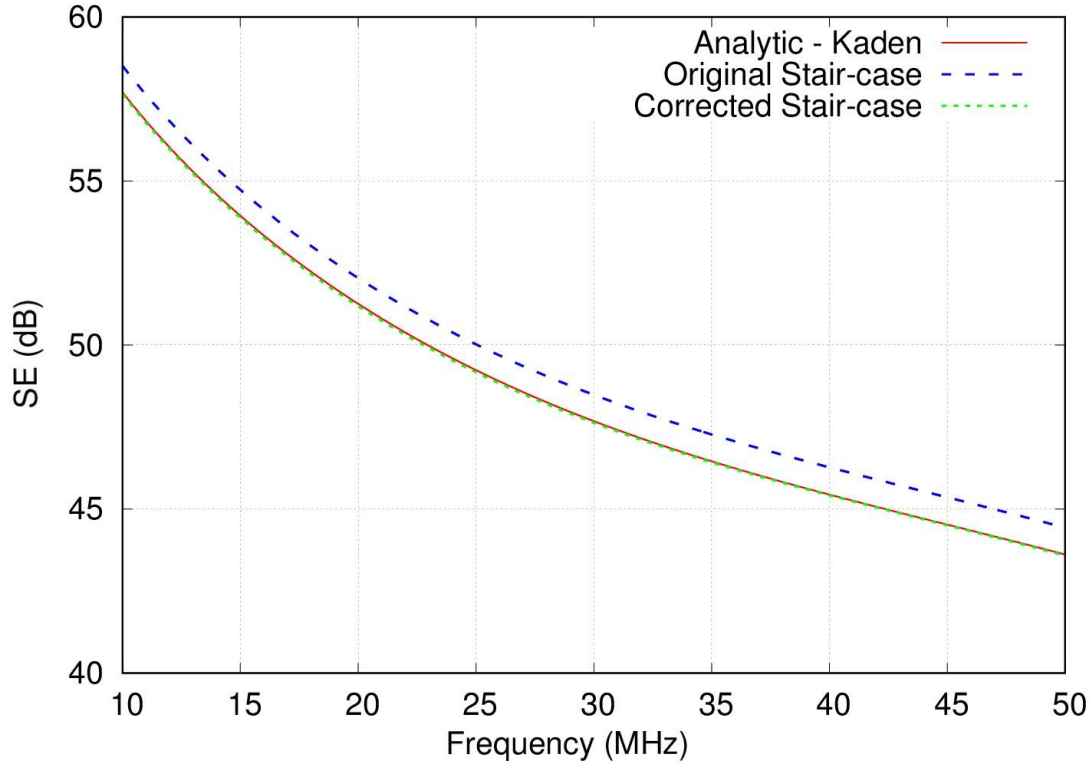
**Figure 4.7:** Diagram of a stair-cased cylindrical shell. Each colour represents a different correction factor that has been applied.

Figure 4.7 shows the stair-cased mesh of a section of a 1 m radius infinitely long cylinder. The surface of the cylinder has been divided into 40 segments. The transmission coefficient for each segment has been determined using the correction factor described above using a value of  $\Theta$  equal to the angle of the tangent of the segment with respect to the mesh. In Figure 4.7 each colour represents a different correction factor. The original transmission and reflection coefficients of the cylinder are 0.004 and 0.99 respectively.



**Figure 4.8:** SE at the centre of a stair-cased cylindrical shell, with and without a correction factor applied compared to an analytic model[3].

Figure 4.8 shows the SE recorded at the centre of the cylindrical shell. For this case the error in SE of the stair-cased model is smaller than that of the cube making it hard to see the effect of the correction factor. It can be seen in Figure 4.8 that the spurious resonance around 185 MHz is not affected, nor is the error in resonant frequency for the main resonances as the mesh itself has not changed.



**Figure 4.9:** Close up look at the SE at the centre of a stair-cased cylindrical shell, with and without a correction factor applied compared to an analytic model[3].

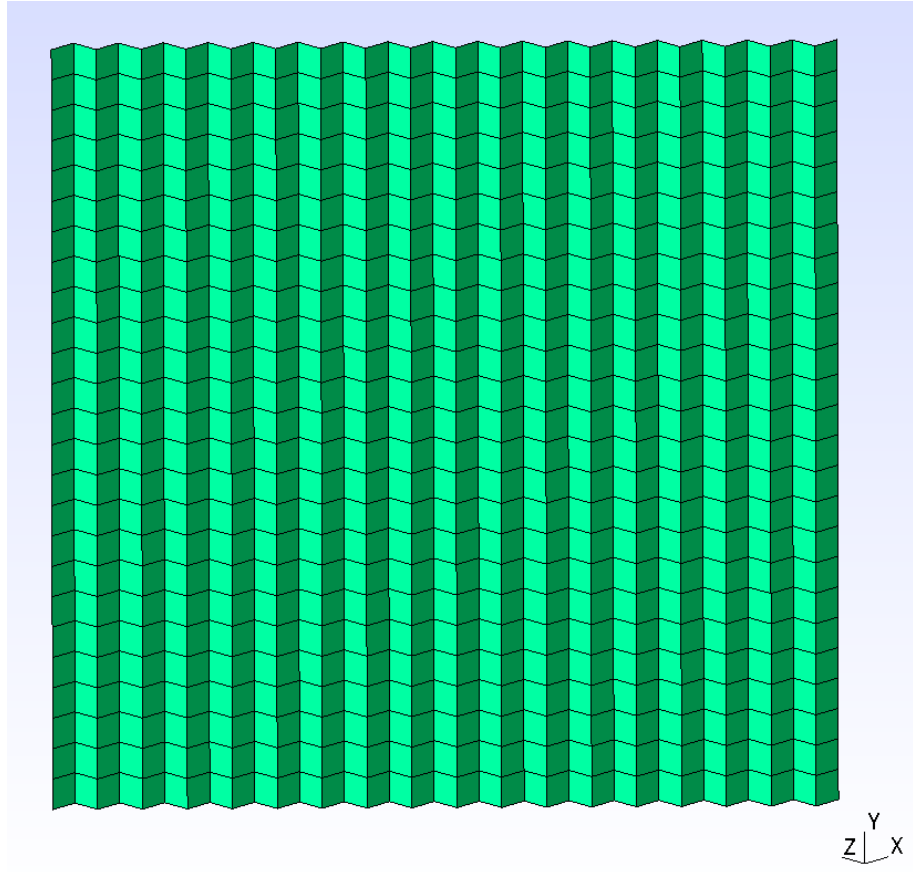
Figure 4.9 shows a closer look at the SE between 10 and 50 MHz. Here it can be seen that the correction factor has reduced the error significantly, from approximately 0.8 dB to <0.1 dB.

#### 4.4 Two Axes of Rotation

The correction factor proposed above has been shown to work for surfaces rotated around a single axis with respect to the mesh. Here, a new correction factor is proposed that can account for rotation around 2 axes. Figure 4.10 shows a planar surface that has been rotated  $45^\circ$  around the  $y$ -axis. In this case the effective length ( $L_e$ ) of the surface edge is:

$$L_e = L(\cos(\Theta) + \sin(\Theta)) \quad (4.23)$$

when considering the  $x$  and  $z$  directed edges of the SIBC faces, where  $L$  is the original length of the surface and  $\Theta$  is the angle of rotation, in this case  $45^\circ$ . The length of the surface along the  $y$ -axis is unchanged.



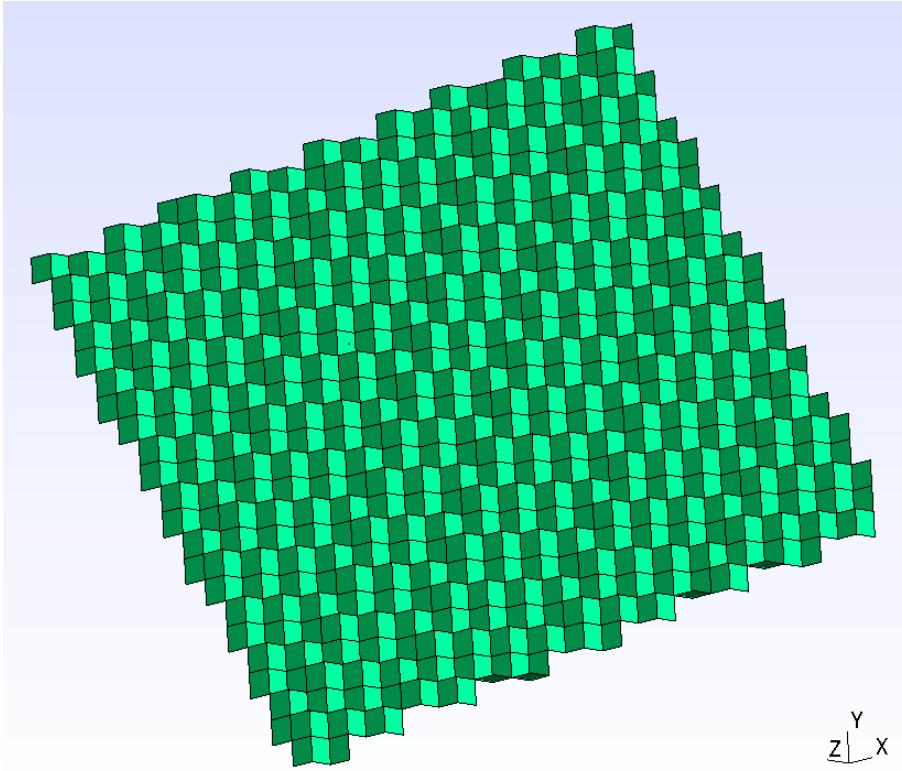
**Figure 4.10:** Diagram of a stair-cased planar material that has been rotated around a single axis.

Figure 4.11 shows the same surface, but it has now been rotated  $30^\circ$  around the  $z$ -axis after being rotated around the  $y$ -axis. The effective length of the surface following the  $x$  and  $z$  directed edges of the SIBC faces is again given by 4.23. However, the length of the surface following the  $x$  and  $y$  directed edges of the SIBC faces is now:

$$L_e = L(\cos(\phi) + \sin(\phi)) \quad (4.24)$$

Where  $\phi$  is the second angle of rotation, in this case  $30^\circ$ . Finally the length of the surface following the  $y$  and  $z$  directed edges of the SIBC faces is:

$$L_e = L(\cos(\Theta) + \sin(\Theta))(\cos(\phi) + \sin(\phi)) \quad (4.25)$$



**Figure 4.11:** Diagram of a stair-cased planar material that has been rotated around two axes.

Once the effective length along each axis pairing is known, the effective transmission for each E-field polarisation can be calculated. Consider the field polarised along the  $x$ -axis. For the 1D rotation case the transmission through the sheet was increased by a factor equal to the effective length coefficient for the  $xz$  pairing. i.e  $\cos(\Theta) + \sin(\Theta)$ . If rotated around the  $x$ -axis the effective transmission would be *reduced* by the length along the  $yz$  pairing i.e  $\cos(\phi) + \sin(\phi)$ . Multiplying these together gives the effective transmission through a sheet rotated around 2 axis:

$$\tau_e^{E_x} = \tau_o^{E_x} \frac{\tau_{yRot}^{E_x}}{\tau_{xRot}^{E_x}} = \tau_o^{E_x} \frac{\cos(\Theta) + \sin(\Theta)}{\cos(\phi) + \sin(\phi)} \quad (4.26)$$

where  $\tau_{xRot}^{E_x}$  and  $\tau_{yRot}^{E_x}$  are the effective transmission coefficients for  $x$ -polarised E-fields due to the  $x$ -axis and  $y$ -axis rotations respectively. To correct the effective transmission the sheet can be given a corrected transmission of:

$$\tau_c^{E_x} = \tau_o^{E_x} \frac{\cos(\phi) + \sin(\phi)}{\cos(\Theta) + \sin(\Theta)} \quad (4.27)$$

Similarly for incident waves with a  $y$ -polarised E-field the corrected transmission factor is:

$$\tau_c^{E_y} = \tau_o^{E_y} \frac{\cos(\Theta) + \sin(\Theta)}{\cos(\phi) + \sin(\phi)} \quad (4.28)$$

For the  $z$ -polarised E-field case the effective transmission is reduced by the rotation

for both the  $x$  and  $y$  axes such that the effective transmission is

$$\tau_e^{Ez} = \tau_o^{Ez} \frac{1}{(\cos(\Theta) + \sin(\Theta))(\cos(\phi) + \sin(\phi))} \quad (4.29)$$

So that the corrected transmission factor is given by:

$$\tau_c^{Ez} = \tau_o^{Ez} (\cos(\Theta) + \sin(\Theta)) (\cos(\phi) + \sin(\phi)) \quad (4.30)$$

Maintaining the principle from (4.20) the reflection coefficients for each polarisation of E-Field can be determined by:

$$\rho_c^{Ex} = \rho_o^{Ex} + \tau_o^{Ex} \left(1 - \frac{\cos(\phi) + \sin(\phi)}{\cos(\Theta) + \sin(\Theta)}\right) \quad (4.31)$$

$$\rho_c^{Ey} = \rho_o^{Ey} + \tau_o^{Ey} \left(1 - \frac{\cos(\Theta) + \sin(\Theta)}{\cos(\phi) + \sin(\phi)}\right) \quad (4.32)$$

$$\rho_c^{Ez} = \rho_o^{Ez} + \tau_o^{Ez} (1 - (\cos(\phi) + \sin(\phi))(\cos(\Theta) + \sin(\Theta))) \quad (4.33)$$

The corrected coefficient presented above assume that the surface has been rotated around the  $x$ -axis by  $\phi$  degrees and around the  $y$ -axis by  $\Theta$  degrees. Rotations on other pairs of axis can be determined accordingly. In all cases when either  $\Theta$  or  $\phi$  is equal to zero, i.e there is only one axis of rotation, the correction factors is reduced to the single axis of rotation form.

## 4.5 Validation of the Correction Factor Method

In this section two further test cases are used to validate the two axes correction factor. The first is the cube case from before, this time rotated around two axes. The second is a spherical shell, this case shows how the correction factor can be used to represent doubly curved surfaces.

### 4.5.1 Cubic Shell Test Case

Again the cubic shell is 1m on each side with transmission and reflection coefficients of 0.004 and 0.99 respectively. The cube has been rotated  $45^\circ$  around its  $z$ -axis and  $30^\circ$  around its  $y$ -axis. The two axes correction factor has been applied to the faces that originally were perpendicular to the  $x$  and  $y$  axes where  $\Theta = 45^\circ$  and  $\phi = 30^\circ$ . The faces that were originally perpendicular to the  $z$ -axis only have a correction factor applied according to a single rotation of  $30^\circ$  as the initial rotation of  $45^\circ$  around the  $z$ -axis does not require a stair-cased mesh and so no stair-casing occurs until the second rotation. The mesh of the cube following the rotations is shown in Figure 4.12.

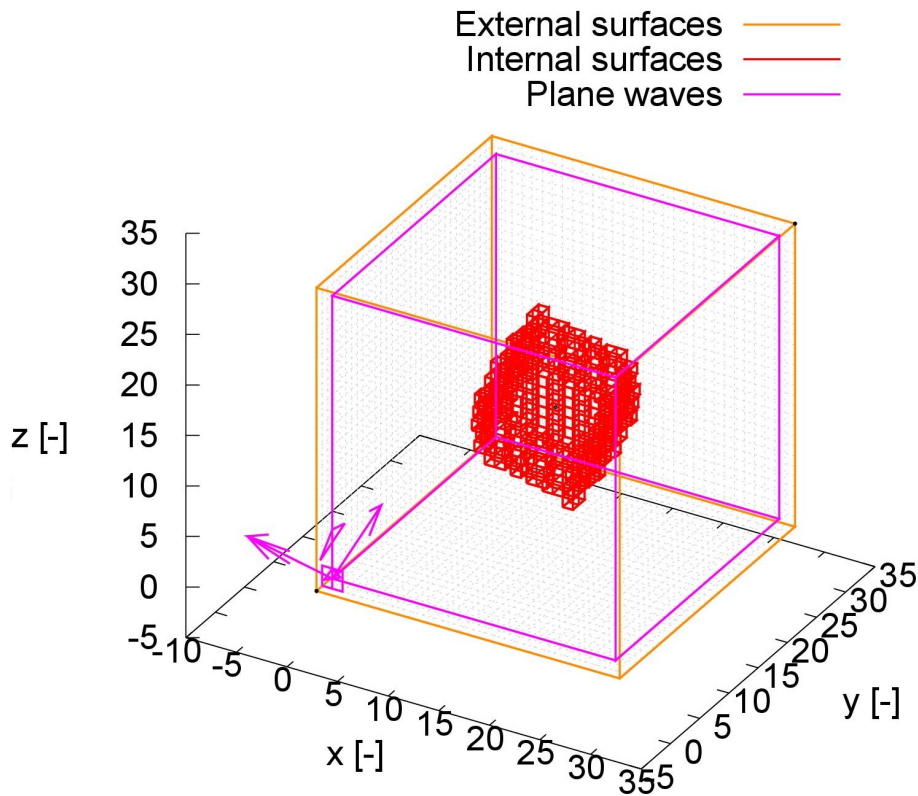


**Figure 4.12:** Set-up of a 1 m hollow cubic shell made from a material with a transmission coefficient of 0.004 and a reflection coefficient of 0.99. The cube has been rotated 45° around the  $z$ -axis and 30° around the  $y$ -axis

Figure 4.13 shows the SE recorded at the centre of the cube. The original stair-case SE is for the two axes rotation. The error in magnitude using the 2 axes correction factor has reduced the error in magnitude of SE significantly from 7dB to less than 1dB. However, when compared to the correction factor result from the single axis of rotation in Figure 4.4 the 2 axes of rotation correction factor has not performed quite as well. This is potentially due to the fact that the mesh has a difficult to predict structure around the edges and corners of the cube. The correction proposed does not account for this aspect of the mesh, but assumes that the effect from edges and corners is small and can be ignored. By reducing the cell size of the mesh the error in edge meshing is also reduced and therefore the effect on the shielding. However, there is a cost associated with this as a smaller mesh required a larger number of nodes and therefore will require longer run times.

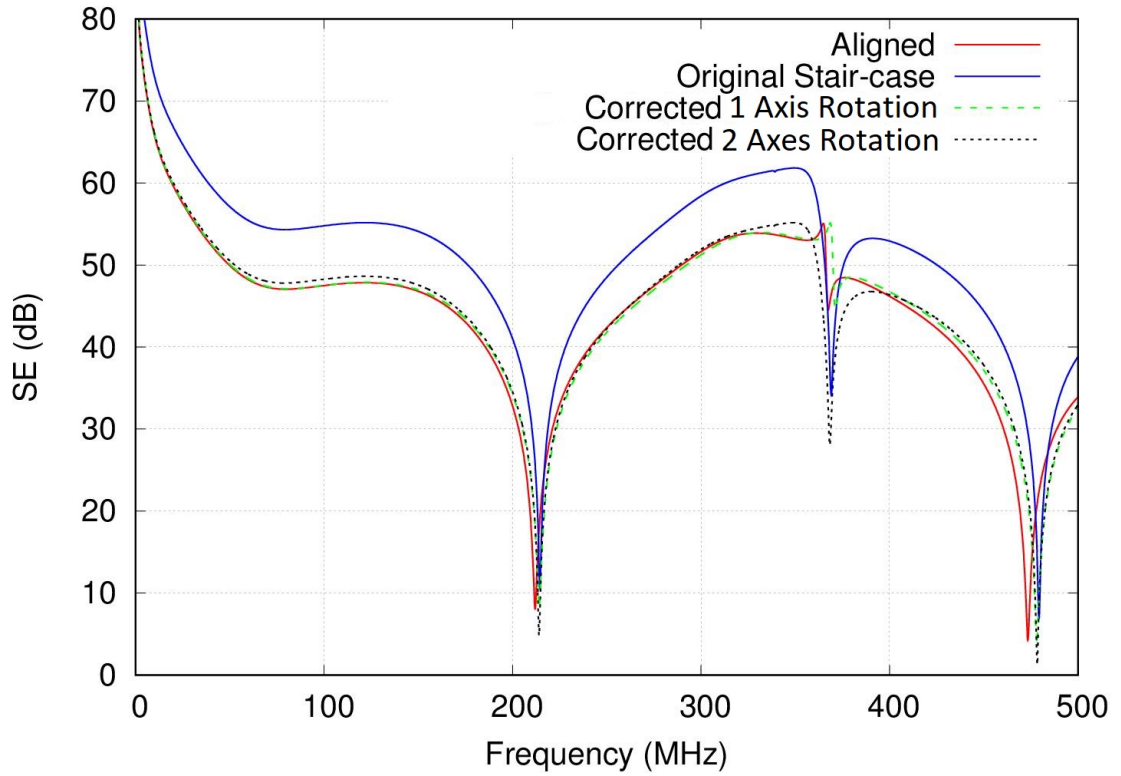


**Figure 4.13:** SE at the centre of a stair-cased cubic shell rotated around two axes with and without a correction factor applied. Comparisons are made with a corrected single axes of rotation stair-cased mesh and a non stair-cased mesh.

It is clear that around the resonance at 365 MHz there is a significant effect due to the high level of stair-casing from rotating around two axes, this effect is less pronounced when the cube was rotated around only one axis. Correcting the transmission and reflection coefficients does not change the structure of the mesh itself and therefore has no effect on the shape of spurious resonances.

#### 4.5.2 Spherical Shell Test Case

The second test case is of a hollow spherical shell. The sphere has a 1m radius and original transmission and reflection coefficients of 0.004 and 0.99. The mesh size for this model is 20mm. The structure is illuminated by a linearly polarised plane-wave and the electric field at the centre of the sphere is recorded in order to determine the SE of the shell. The mesh used in this problem is the same as the one used in Section 3.2.1.

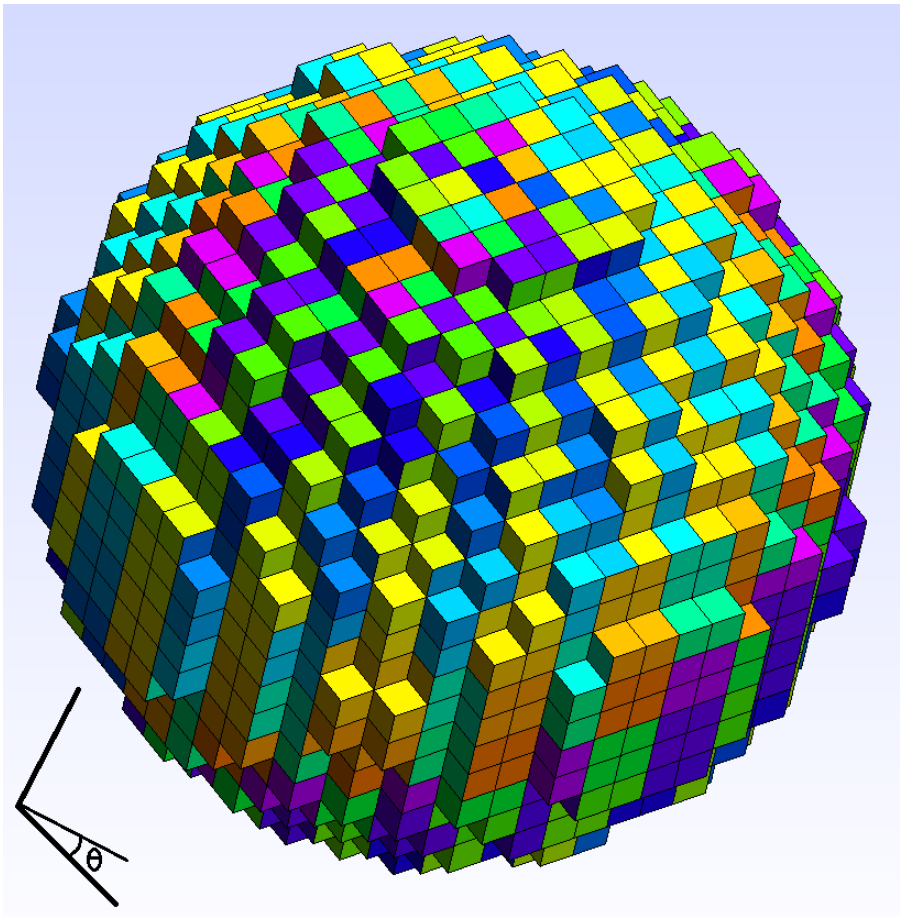


**Figure 4.14:** Diagram of a stair-cased spherical shell. Each colour represents a different correction factor that has been applied.

Using the same principle as the cylindrical shell the mesh of the sphere has had different correction factors applied to different segments of the shell surface based on the angle of the tangent of the surface with respect to the grid. Figure 4.14 shows how the surface has been divided into different sections, each colour represents a different correction factor that has been applied.

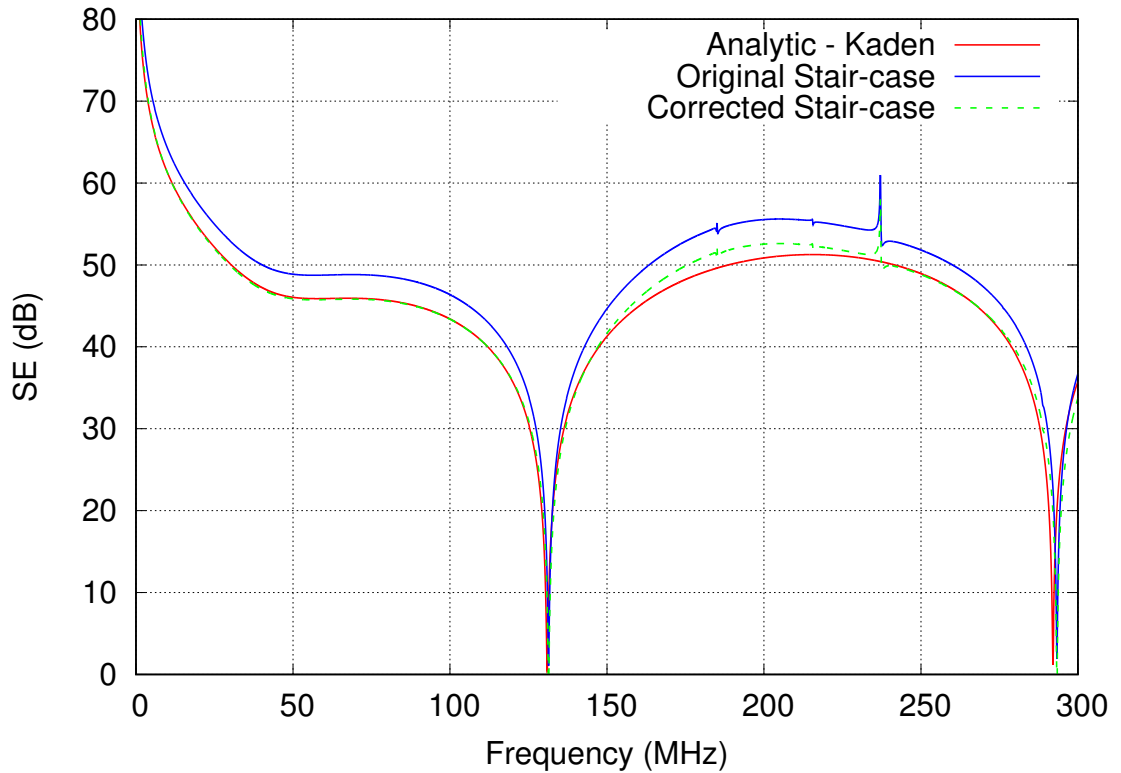


**Figure 4.15:** SE at the centre of a stair-cased spherical shell, with and without a correction factor applied compared to an analytic model[3].

Figure 4.15 shows the SE at the centre of the sphere. It can be seen that the error in magnitude of SE is reduced when using the correction factor from approximately 3 dB to less than 0.2 dB. As discussed previously there are no corrections to those errors caused by the structure of the mesh with regards to resonances and frequency shift. The results presented have been concerned with the shielding of cavities, this is heavily dependent on the initial transmission through the cavity surface and the internal reflections. To test the full capabilities of the correction factor method the scattering from the spherical mesh was also considered. In this case the scattering results are driven primarily by the initial reflection from the spherical surface.

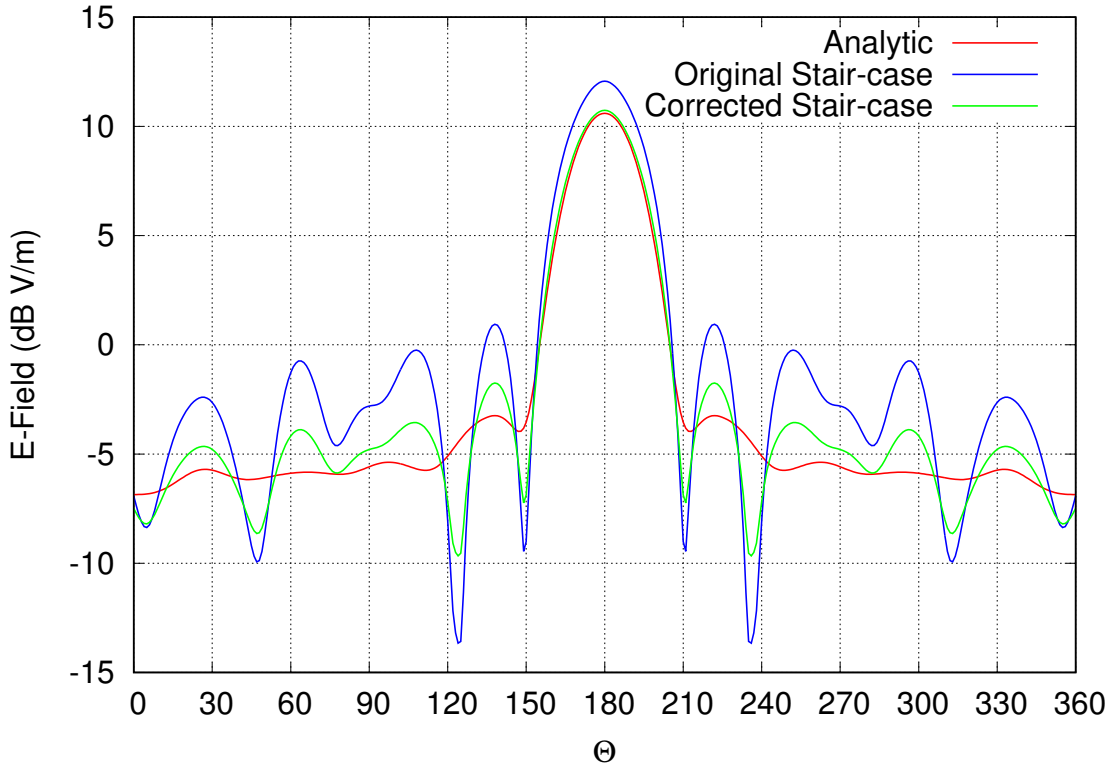


**Figure 4.16:** Scattering from the spherical cavity in the YZ plane, with and without a correction factor applied, compared to an analytic model[3].  $\Theta$  is the angle of scattering.

To measure the scattering from the shell the field was recorded on a cubic surface near the boundaries of the problem space. The data was then imported into CST and a far field transformation was applied to the field to determine the field at a distant point from the cavity. Figure 4.16 shows the recorded far field scattering of the E-field in the YZ plane from the sphere. The angle  $\Theta$  refers to the angle of scattering where  $180^\circ$  is a reflection along the normal to the angle of incidence. It can be seen that the error in the magnitude of the scattered E-Field has been reduced significantly, at  $180^\circ$  the error has been reduced from 2 dB to 0.1 dB. The error in magnitude for the secondary peaks has also been reduced, but in these cases the reduction in error is not as significant and there are still clear errors.

## 4.6 Summary

This chapter has considered a new solution to the issue of stair-cased meshing causing errors in the transmission and reflection of electromagnetic waves incident upon material surfaces. An analytic determination of the errors has been shown and a proposed solution alters the transmission and reflection coefficients to cancel out the predetermined error based on the angle of the modelled surface to the FDTD grid. As the polarisation of

the incident wave affects the amplitude of the errors the proposed correction factor must be applied anisotropically and equations for the correction factor for rotations of surfaces around a single axis have been produced.

Two test cases were presented to validate the single axis correction factor method for the shielding of cavities. The first case was a cubic shell that had four stair-cased faces. Each face is a plane and therefore at a constant angle to the grid, this meant that a single correction factor could be applied to each face. The error in magnitude of the SE at the centre of the cube for this case was shown to be reduced significantly from 7 dB to less than 0.1 dB for a frequency away from a resonant frequency. The Q-factor of the resonances of the SE was also shown to improve significantly.

The second test case was an infinite cylindrical shell. This case demonstrated how the proposed correction factor can be used to represent curved surfaces by applying different correction factors to different sections of the cylinder based on the tangential angle to the grid of the given section. Again the error in SE was reduced, from 0.8 dB to  $<0.1$  dB away from the resonance.

A more complex correction factor has been proposed to apply to situations where a surface is rotated around two axes with respect to the mesh. The proposed correction factor has been determined for each polarisation of E-field based on the rotation angle around each axis. Again two test cases were used to validate the proposed method. The first case was the same cube as before, however it had been rotated around two axes. It was shown that the error in magnitude of SE in this case was reduced significantly as before, but the error was not reduced quite to the level of the single axis case. The second test case was of a spherical shell. This case uses a doubly curved surface and shows how the two axes correction factor can be applied to curved surfaces in a similar manner to the cylindrical test case. It is shown that the error magnitude of the SE is again improved by using the correction factor. It is also shown that the error in the magnitude of the far-field scattering of the E-field is reduced, although not as significantly around subsidiary peaks as the central peak.

In all of the test cases it is clear that application of the proposed correction factors has improved the accuracy of the results. However, it is also clear that there are limitations to this method, as the stair-cased mesh itself is not changed there is no reduction in errors resulting from frequency shift or the appearance of spurious resonances.



## Chapter 5

# Conformal Boundaries for FDTD

The previous chapter proposed a method to correct some of the errors that arise due to stair-cased meshing. However, that method still relies on a stair-cased mesh and there are some inherent issues that cannot be resolved without increasing the resolution of the mesh, which can be computationally prohibitive. An alternative to stair-cased meshing is to use a conformal algorithm. Conformal algorithms are based on the principal of deforming local cells to conform to curved and non-aligned surfaces. The deformed cells will no longer have a regular cuboid shape and the update equations for the fields in and around the deformed cells must be adjusted accordingly.

In this chapter some of the most popular existing conformal algorithms for PEC boundaries and their limitations are presented. A pre-existing conformal bulk material algorithm is discussed. A new conformal algorithm incorporating the face centred thin boundary model from Section 2.4.2 is presented with validation using multiple shielding and scattering test cases.

### 5.1 Conformal Algorithms for PEC Boundaries

The earliest conformal algorithms [63–67] focused on representing boundaries made from perfect electric conductors (PEC). A PEC boundary reflects all of an incident wave and therefore no consideration needs to be made of transmission through the boundary or material loss. The first models had issues with late-time stability [68] and lack of tools for generating meshes [69]. The most popular early conformal algorithm that was consistently stable was developed by Dey and Mittra[70].

### 5.1.1 The Dey-Mitra (DM) Method

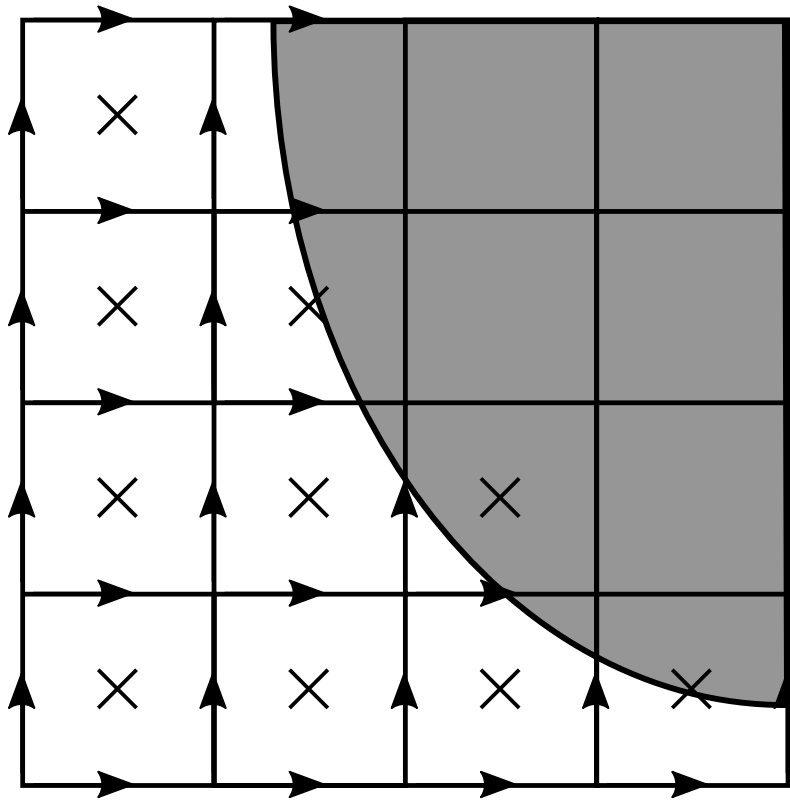


**Figure 5.1:** Two-dimensional diagram of non orthogonal object on a cubic grid. Arrows represent the electric fields, crosses represent magnetic fields.

The example in Figure 5.1 shows an arbitrarily curved object on a Cartesian grid. The object is a PEC and therefore the fields inside the object are zero. However, at the material boundaries the grid does not align with the shape of the object.

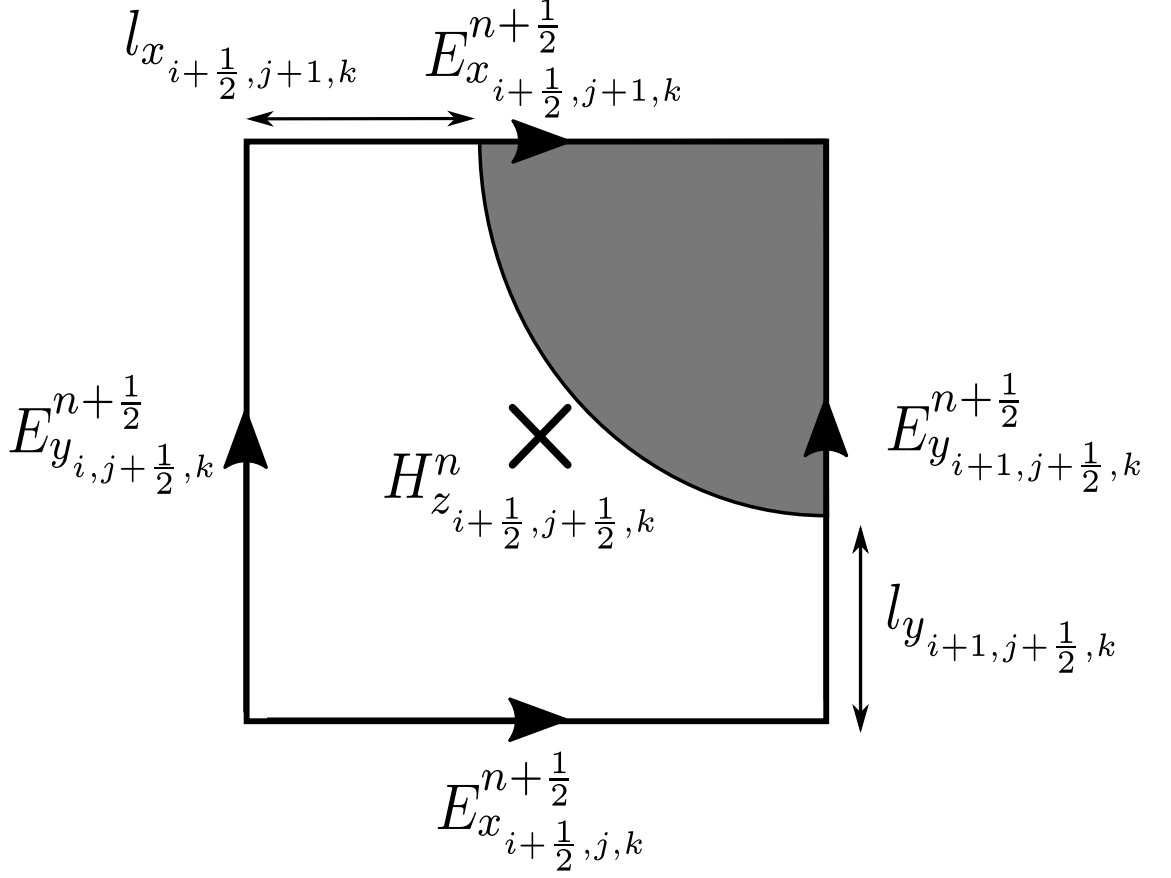


**Figure 5.2:** Single cell of FDTD grid partially filled with PEC object

The DM algorithm works by adjusting the electric and magnetic fields along the surface of the object based on the partial edge lengths  $l_x$  and  $l_y$  as shown in Figure 5.2. Where the partial edge length  $l = 0$  the electric field is also 0 as it is inside the PEC material. However, if  $l > 0$  then the discrete electric field will be non-zero. Calculating E, normally as in (2.10), then scaling proportionally by the appropriate edge length gives:

$$\tilde{E}_{x_{i+\frac{1}{2},j,k}}^{n+\frac{1}{2}} = E_{x_{i+\frac{1}{2},j,k}}^{n+\frac{1}{2}} \delta_{x_{i+\frac{1}{2},j,k}} \quad (5.1)$$

Where  $\delta_x$  is the fractional edge length given by:

$$\delta_{x_{i+\frac{1}{2},j,k}} = \frac{l_{x_{i+\frac{1}{2},j,k}}}{\Delta x} \quad (5.2)$$

Similarly the permeability is scaled proportionally to the fractional area such that:

$$\tilde{\mu}_{x_{i+\frac{1}{2},j+\frac{1}{2},k}} = \mu S_{x_{i+\frac{1}{2},j+\frac{1}{2},k}} \quad (5.3)$$

Where the fraction area  $S_z$  is given by:

$$S_{z_{i+\frac{1}{2},j+\frac{1}{2},k}} = \frac{A_{z_{i+\frac{1}{2},j+\frac{1}{2},k}}}{\Delta x \Delta y} \quad (5.4)$$

Where  $A_z$  is the area of the cell that is *not* PEC. With the scaled electric fields and permeability a new version of (2.9) can be written:

$$H_{z_{i+\frac{1}{2},j+\frac{1}{2},k}}^{n+1} = H_{z_{i+\frac{1}{2},j+\frac{1}{2},k}}^n - \frac{\Delta t}{\tilde{\mu}_{z_{i+\frac{1}{2},j+\frac{1}{2},k}}} \cdot \left( \frac{\tilde{E}_{y_{i+1,j+\frac{1}{2},k}}^{n+\frac{1}{2}} - \tilde{E}_{y_{i,j+\frac{1}{2},k}}^{n+1}}{\Delta x} - \frac{\tilde{E}_{y_{i+\frac{1}{2},j+1,k}}^{n+\frac{1}{2}} - \tilde{E}_{x_{i+\frac{1}{2},j,k}}^{n+1}}{\Delta y} \right) \quad (5.5)$$

And based on (5.5) the final version of the electric update is given by:

$$\tilde{E}_{x_{i+\frac{1}{2},j,k}}^{n+\frac{1}{2}} = \tilde{E}_{x_{i+\frac{1}{2},j,k}}^{n-\frac{1}{2}} + \frac{\Delta t}{\tilde{\epsilon}_{x_{i+\frac{1}{2},j,k}}} \left[ \left( \frac{H_{z_{i+\frac{1}{2},j+\frac{1}{2},k}}^n - H_{z_{i+\frac{1}{2},j-\frac{1}{2},k}}^n}{\Delta y} \right) - \left( \frac{H_{y_{i+\frac{1}{2},j,k+\frac{1}{2}}}^n - H_{y_{i+\frac{1}{2},j,k-\frac{1}{2}}}^n}{\Delta z} \right) \right] \quad (5.6)$$

Where the scaled permittivity  $\tilde{\epsilon}$  is given by:

$$\tilde{\epsilon}_{x_{i+\frac{1}{2},j,k}} = \left[ \frac{\epsilon}{\delta_x} \right]_{i+\frac{1}{2},j,k} \quad (5.7)$$

Similar update equations can be derived for  $H_x$ ,  $H_y$ ,  $E_y$ ,  $E_z$  and their corresponding permeabilities and permittivities.

The above update equations are similar to those of the standard Yee algorithms, however they rely on partial edge lengths and areas, therefore the stability of these equations is dependent on these partial lengths. Applying the time difference stability limit as in (2.40) gives:

$$\Delta t = \frac{1}{\tilde{c}_{max}} \frac{CFLN}{\sqrt{\frac{1}{\Delta x^2} + \frac{1}{\Delta y^2} + \frac{1}{\Delta z^2}}} \quad (5.8)$$

Where:

$$\frac{1}{\tilde{c}_{max}} = \min\left(\sqrt{\frac{S\mu\epsilon}{\delta}}\right) \quad (5.9)$$

And  $S$  and  $\delta$  are the partial areas and lengths of a particular face. This means that the time step of a simulation is determined by the smallest fractional edge length, in the case the fractional edge length is very small ( $\delta \ll 1$ ) the time step can also become very small causing the runtime of the simulation to become unreasonably large. There is also an issue of areas significantly smaller than the undistorted cell face area (<5%) and cells with a high side length to area ratio (>12) caused the scheme to become unstable.

A later paper by the same authors provided a method to overcome these instabilities [60]. When generating a mesh for use with this method each cell was checked to see if it violated the limits of stability (i.e. had area <5% or edge/surface ration >12) and if so marked the discrete E and H fields of that cell with a flag to alert the program that they

should be updated with a special algorithm. The H field would be updated using (5.5) as normal, but then it would be averaged with the previous value such that:

$$H_{z_{i,j,k}}^{n+1} = \frac{H_{z_{i,j,k}}^{n+1} + H_{z_{i,j,k}}^n}{2} \quad (5.10)$$

While applying this method does prevent the instabilities observed, there is also a small performance and accuracy penalty for doing so. Another suggested solution is to ignore lengths that are too small, effectively treating that cell as if the object fills that entire cell. This is an efficient stable solution, however it also has a small accuracy penalty.

### 5.1.2 Variations on the Dey-Mittra Method

There are a number of variations on the DM algorithm that attempt to address the efficiency issues caused by small time steps and to improve the accuracy [71, 72]. While there are countless variations, the most popular ones are detailed below.

#### Yu-Mittra (YM)

Another solution to the issue of unreasonably small time steps was put forth by Yu and Mittra [73]. This method does not require any limitation on  $\Delta t$  save for that imposed by the base Yee algorithm by (2.40). The algorithm is based on the previous algorithm however the fractional area  $S_z$  is always set as one. As such the permeability is not altered and (5.5) becomes:

$$H_{z_{i+\frac{1}{2},j+\frac{1}{2},k}}^{n+1} = H_{z_{i+\frac{1}{2},j+\frac{1}{2},k}}^n - \frac{\Delta t}{\mu} \cdot \left( \frac{\tilde{E}_{y_{i+1,j+\frac{1}{2},k}}^{n+\frac{1}{2}} - \tilde{E}_{y_{i,j+\frac{1}{2},k}}^{n+1}}{\Delta x} - \frac{\tilde{E}_{y_{i+\frac{1}{2},j+1,k}}^{n+\frac{1}{2}} - \tilde{E}_{x_{i+\frac{1}{2},j,k}}^{n+1}}{\Delta y} \right) \quad (5.11)$$

Substituting  $S = 1$  into (5.9) and comparing it to the base Yee algorithm limit gives:

$$\min\left(\sqrt{\frac{\mu\epsilon}{\delta}}\right) \geq \min(\sqrt{\mu\epsilon}) \quad (5.12)$$

And therefore the limit on  $\Delta t$  imposed by the YM algorithm is always equal to or better than the base Yee limit. Therefore there are no time constraints due to YM algorithm. There is however a loss in accuracy due to the lack of correction by the fractional area.

#### Benkler, Chavannes and Kuster (BCK)

The Benkler-Chavannes-Kuster (BCK) algorithm is also a variation on the base DM algorithm [74]. Similarly to the YM method it addresses the issue of the time constraint being proportional to the shortest fractional length by adjusting the fractional area  $S$ . However unlike YM, the fractional area is not simply set to one. The user specifies a desired

CFLN and the algorithm adjusts each fractional area to fit. It does this by calculating the fractional area for each conformal cell, from this it determines the maximum stable CFLN that can be used. If this number is smaller than the specified CFLN the algorithm increases the value of the fractional area until the desired CFLN is met. This means that the time step can be controlled by the user and small local inaccuracies will be introduced to preserve the time step.

The example used by Benkler et al. was a simulation of a PEC sphere with a radius of  $\lambda/5.77$  where  $\lambda$  is the free space wavelength. The error is measured in comparison to the analytic Mie-series solution [75] using the mean square error. A comparison between the BCK, YM and DM methods showed that the BCK method is very accurate for low CFL numbers, but suffers from inaccuracies as the CFLN is increased. The DM is limited in the range of CFLN number that used due to the time step constraints and therefore was not run above  $\text{CFLN} = 0.7$ . The YM method is less accurate than DM but has the advantage of allowing a CFLN of 1.

It would appear that the BCK method is the most useful, however it should be noted that this method involves extra preprocessing and is more complicated to implement than the simpler conformal methods.

## 5.2 A Conformal Algorithm for Bulk Materials

The methods so far described can be used to model conformal PEC boundaries. However, there is also a need to model conformal boundaries that can be penetrated. There have been multiple variations of conformal algorithm to achieve this [76, 77]. This section will describe a method put forward by Yu and Mittra [62].

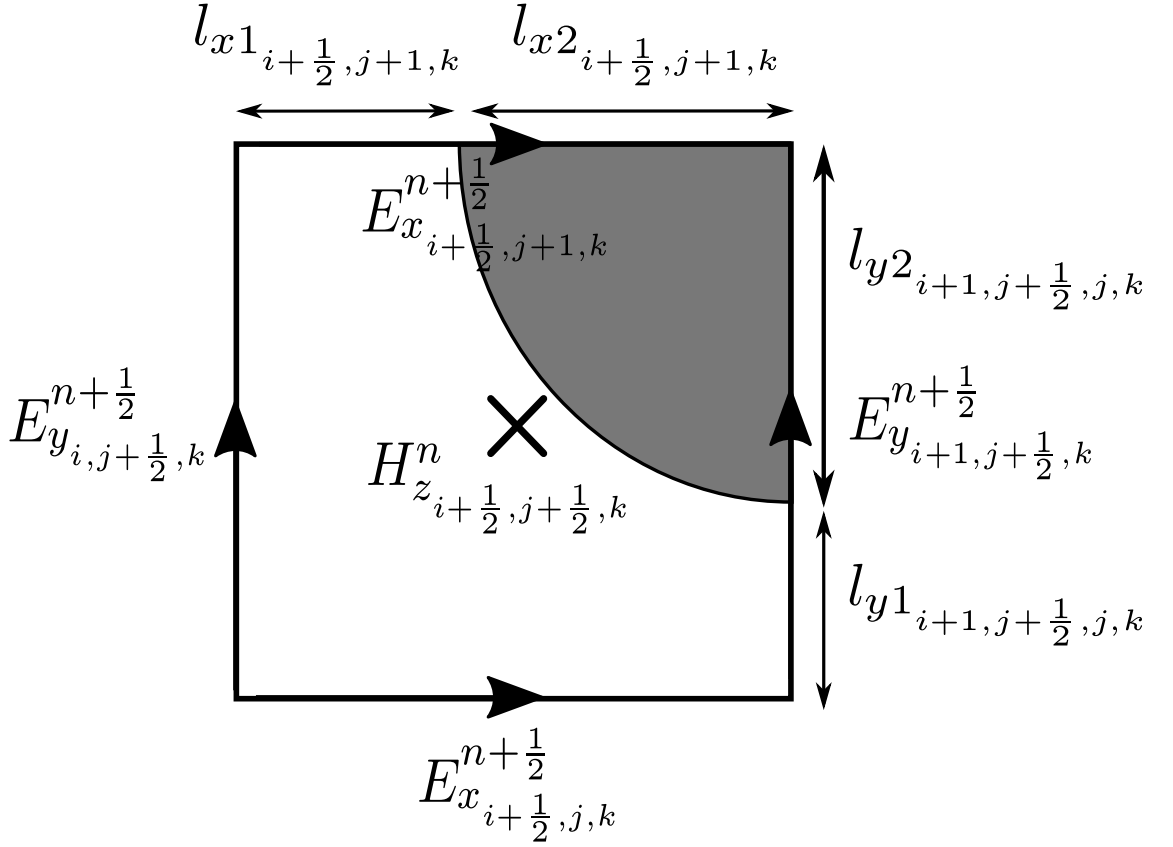


**Figure 5.3:** Single cell of FDTD grid partially filled with material object

Figure 5.3 shows a single cell with a curved material surface. As in the DM method the cell is broken into partial lengths, these are used to determine the local permittivities:

$$\varepsilon_{x_{i+\frac{1}{2},j+1,k}} = \frac{(\varepsilon_1 l_{x1_{i+\frac{1}{2},j+1,k}} + \varepsilon_2 l_{x2_{i+\frac{1}{2},j+1,k}})}{\Delta x} \quad (5.13)$$

$$\varepsilon_{y_{i+1,j+\frac{1}{2},k}} = \frac{(\varepsilon_1 l_{y1_{i+1,j+\frac{1}{2},k}} + \varepsilon_2 l_{y2_{i+1,j+\frac{1}{2},k}})}{\Delta y} \quad (5.14)$$

Where  $\varepsilon_1$  is the permittivity of the empty area of the cell and  $\varepsilon_2$  is the permittivity of the material. These equations can be reformed using (5.2) to give:

$$\varepsilon_{x_{i+\frac{1}{2},j+1,k}} = (\varepsilon_1 \delta_{x1_{i+\frac{1}{2},j+1,k}} + \varepsilon_2 \delta_{x2_{i+\frac{1}{2},j+1,k}}) \quad (5.15)$$

$$\varepsilon_{y_{i+1,j+\frac{1}{2},k}} = (\varepsilon_1 \delta_{y1_{i+1,j+\frac{1}{2},k}} + \varepsilon_2 \delta_{y2_{i+1,j+\frac{1}{2},k}}) \quad (5.16)$$

The magnetic update for  $H_z^n$  is calculated as normal from (2.11). The electric fields are updated using the fractional permittivities such that:

$$E_{x_{i+\frac{1}{2},j+1,k}}^{n+\frac{1}{2}} = E_{x_{i+\frac{1}{2},j+1,k}}^{n-\frac{1}{2}} + \frac{\Delta t}{\varepsilon_{x_{i+\frac{1}{2},j+1,k}}} \left[ \begin{aligned} & \left( \frac{H_{z_{i+\frac{1}{2},j+\frac{1}{2},k}}^n - H_{z_{i+\frac{1}{2},j-\frac{1}{2},k}}^n}{\Delta y} \right) \\ & - \left( \frac{H_{y_{i+\frac{1}{2},j,k+\frac{1}{2}}}^n - H_{y_{i+\frac{1}{2},j,k-\frac{1}{2}}}^n}{\Delta z} \right) \end{aligned} \right] \quad (5.17)$$

A similar update equation is used for  $E_{y_{i+1,j+\frac{1}{2},k}}^{n+\frac{1}{2}}$ . This method can also be used to model lossy materials using the method described in Section 2.3.  $\sigma_1$  and  $\sigma_2$  represent the conductivities outside and inside the material respectively. In the case that outside the material is free space  $\sigma_1$  would be zero.

$$\sigma_{x_{i+\frac{1}{2},j+1,k}} = \left( \sigma_1 \delta_{x1_{i+\frac{1}{2},j+1,k}} + \sigma_2 \delta_{x2_{i+\frac{1}{2},j+1,k}} \right) \quad (5.18)$$

$$\sigma_{y_{i+1,j+\frac{1}{2},k}} = \left( \sigma_1 \delta_{y1_{i+1,j+\frac{1}{2},k}} + \sigma_2 \delta_{y2_{i+1,j+\frac{1}{2},k}} \right) \quad (5.19)$$

Equations (5.18) and (5.19) can be applied to (2.46) to allow conformal conducting materials.

### 5.3 A Conformal Thin Layer Model

Here the face centred SIBC model from Section 2.4.2 is adapted to a conformal mesh. There has been some basic work carried out in this area [78] based on edge centred SIBC, however there is limited validation for such work beyond stability analysis.

Consider the cell in Figure 5.4, the shaded boundary has been positioned away from the  $xy$ -plane face at  $z=k$  towards the centre of the cell to conform with a surface passing through the cell, by directly modifying a stair-cased surface mesh. Where  $l_1, l_2, l_3$  and  $l_4$  are the distance that each corner of the boundary has moved.

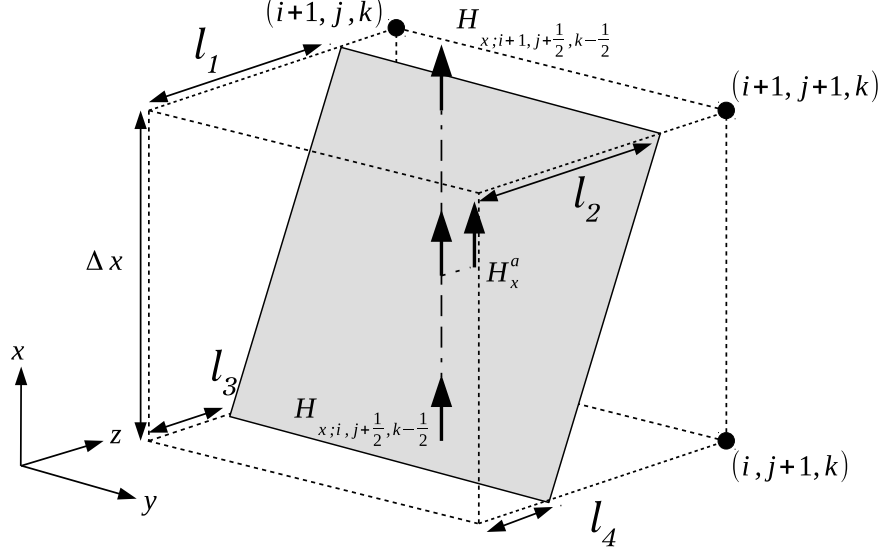


**Figure 5.4:** Conformal algorithm applied to a single cell. The shaded surface is not parallel to any cell face.

The face centred SIBC uses spatial interpolation to approximate the magnetic field at the centre of the SIBC parallel to the face, on the mesh cell surface. This is achieved by averaging the magnetic fields on the surface of the cell:

$$H_x^a = \frac{H_{x;i,j+\frac{1}{2},k-\frac{1}{2}}^{n-\frac{1}{2}} + H_{x;i+1,j+\frac{1}{2},k-\frac{1}{2}}^{n-\frac{1}{2}}}{2} \quad (5.20)$$

To apply a conformal SIBC the magnetic fields are not equidistant to the centre of the cell and must be weighted according to their distances, so (5.20) becomes:

$$H_x^a = \frac{\frac{1}{2}(\delta_1 + \delta_2)H_{x;i,j+\frac{1}{2},k-\frac{1}{2}}^{n-\frac{1}{2}} + \frac{1}{2}(\delta_3 + \delta_4)H_{x;i+1,j+\frac{1}{2},k-\frac{1}{2}}^{n-\frac{1}{2}}}{2} \quad (5.21)$$

Where  $\delta_1, \delta_2, \delta_3$  and  $\delta_4$  are the fractional edge lengths:

$$\delta_s = \frac{l_s}{\Delta z}, s = 1, 2, 3, 4 \quad (5.22)$$

Similar update equations can be derived for determining the  $y$ -polarised magnetic field. The usual FDTD equations are used to update the surrounding magnetic field components using the electric fields on the SIBC surface modified by the average fractional edge length:

$$H_{x;i,j+\frac{1}{2},k-\frac{1}{2}}^{n+1} = H_{x;i,j+\frac{1}{2},k-\frac{1}{2}}^n + C_{hxe} \left[ \frac{1}{\Delta z k} \left\{ \frac{1}{2}(\delta_3 + \delta_4) E_{y;i,j+\frac{1}{2},k}^{a;n+\frac{1}{2}} - E_{y;i,j+\frac{1}{2},k-1}^{n+\frac{1}{2}} \right\} + \frac{1}{\Delta y j} \left\{ E_{z;i,j,k-\frac{1}{2}}^{n+\frac{1}{2}} - E_{z;i,j+1,k-\frac{1}{2}}^{n+\frac{1}{2}} \right\} \right] \quad (5.23)$$

Where  $C_{i,j+\frac{1}{2},k-\frac{1}{2}}^{hxe}$  is the standard magnetic field update coefficient (2.15). Again, similar update equations can be derived for the  $y$ -polarised magnetic fields. Any  $yz$ -plane and  $zx$ -plane faces on the staircase mesh in the cell are dealt with in the same way and the sum of the coincident boundaries gives the correct overall behaviour.

## 5.4 Validation of the Conformal SIBC Algorithm

Presented here is a series of test cases to validate the proposed algorithm. These cases test the performance of the algorithm when modelling the shielding and scattering of different cavities and the shielding of a cavity made using an anisotropic material.

### 5.4.1 Shielding Effectiveness of Cavities

The shielding effectiveness of a cavity is dependent only on the material and geometry of the cavity. As discussed in Section 3.2 the geometry of the cavity affects the resonant structure and small variations in the geometry can shift the resonant structure and this is most apparent at positions that correspond to resonant field nodes, resulting in apparently spurious resonances [79].

In this section four shielding cases are presented to validate the proposed algorithm. Analysis of the results will consider improvements in the SE and reduction or removal of spurious resonances as indicators of the algorithm's performance.

#### 1D Resonator Test Case

The conformal algorithm was initially validated using a 1D resonator test case. This test consists of two thin planar boundaries separated by 3.95m of free space. The boundaries are isotropic and symmetrical with constant transmission and reflection coefficients of 0.004 and -0.99 respectively.

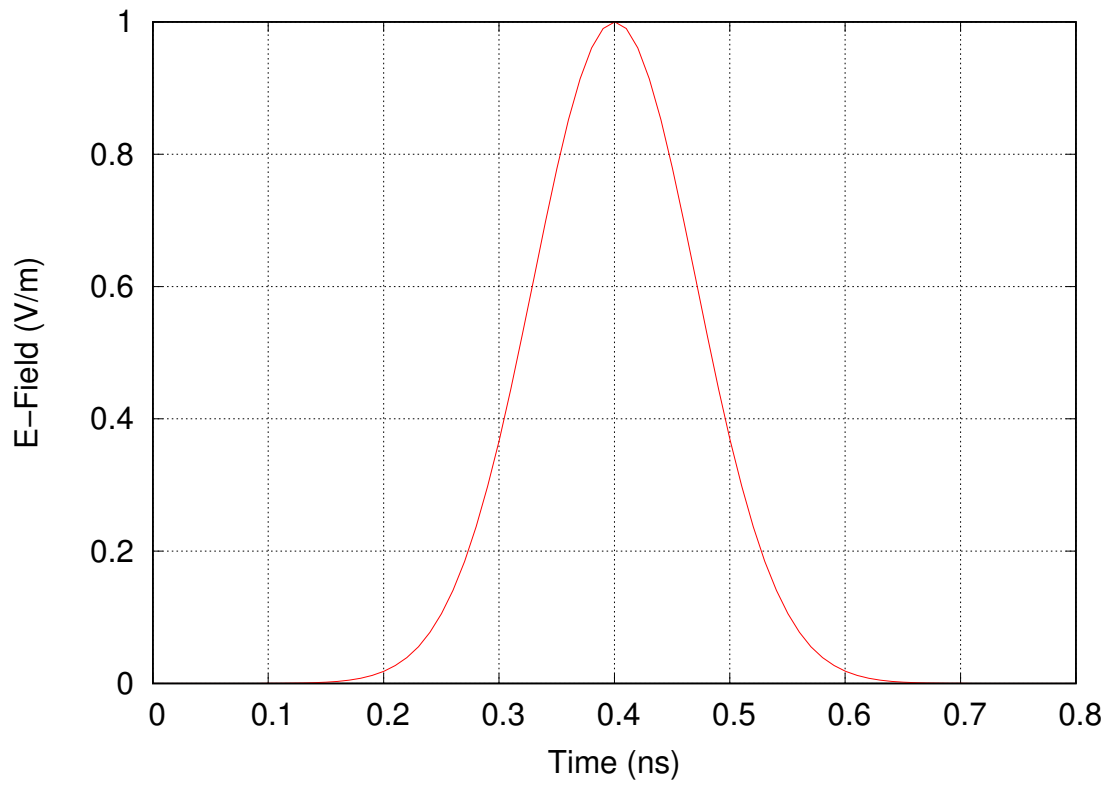


**Figure 5.5:** Gaussian incident wave in the time domain.

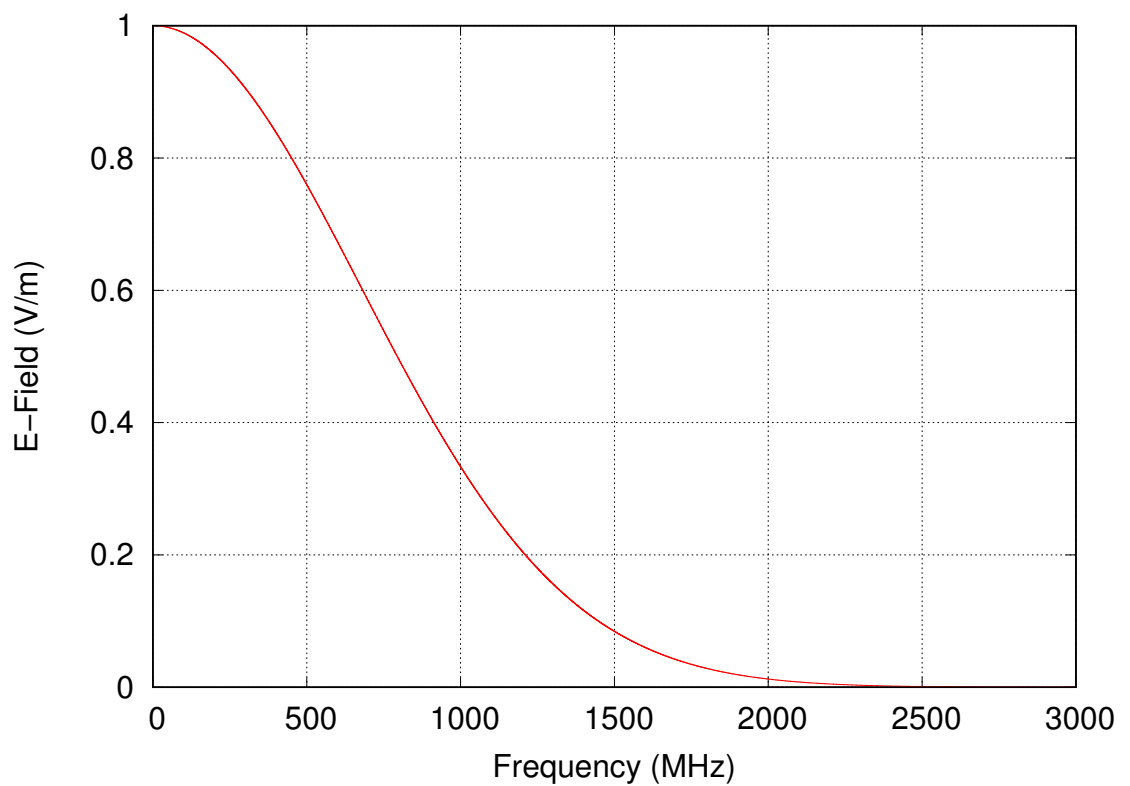


**Figure 5.6:** Gaussian incident wave in the frequency domain.

A Gaussian pulse is used to illuminate the resonator at normal incidence from the left as shown in Figure 5.7. The time domain waveform of the incident pulse is given in Figure

5.5. A fourier transform of the time domain wave gives the frequency response shown in Figure 5.6.

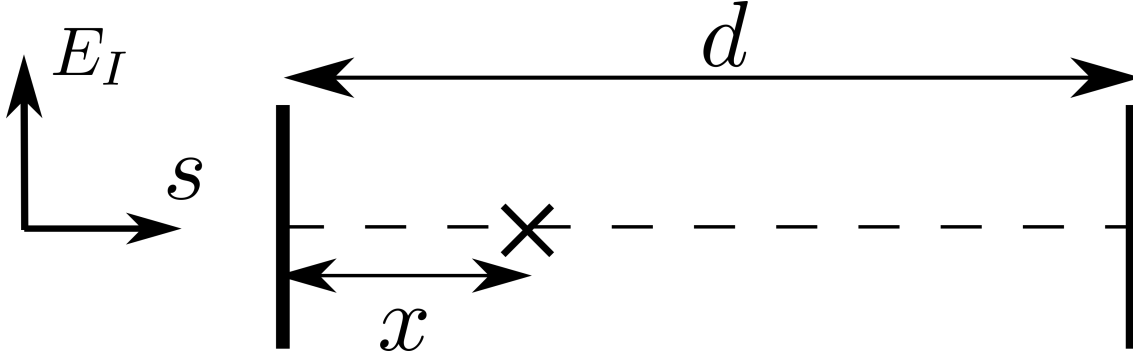


**Figure 5.7:** 1D Resonator Diagram.  $E_I$  is the incident electric field and  $s$  is the direction of propagation.

The frequency response for the electric field at a given point in the cavity can be determined analytically. The electric field at a given frequency is the sum of the amplitude of waves of the frequency travelling in the positive direction and waves travelling in the negative direction:

$$E(x) = \vec{E}(x) + \overleftarrow{E}(x) \quad (5.24)$$

The amplitude of the initially transmitted wave at  $x$  is equal to:

$$E_I \tau e^{-\gamma x} \quad (5.25)$$

where  $E_I$  is the magnitude of the incident electric field,  $x$  is the distance from the left side of the cavity,  $d$  is the length of the cavity,  $\gamma$  is the complex propagation constant and  $\tau$  is the transmission coefficient of the boundaries. The transmitted wave is reflected from the rightmost boundary, propagates back across the cavity in the negative direction and reflected from the leftmost boundary. The wave has now been reflected twice and passes point  $x$  travelling in the positive direction with an amplitude of:

$$E_I \tau \rho^2 e^{-\gamma(2d+x)} \quad (5.26)$$

where  $\rho$  is the reflection coefficient of the boundaries. The wave continues to reflect inside the cavity and the sum of the internal waves travelling in the positive direction is given by:

$$\vec{E}(x) = E_I \tau e^{-\gamma x} + E_I \tau \rho^2 e^{-\gamma(2d+x)} + E_I \tau \rho^4 e^{-\gamma(4d+x)} \dots \quad (5.27)$$

Taking out the common factor of (5.27) gives:

$$\vec{E}(x) = E_I \tau e^{-\gamma x} \left[ 1 + \rho^2 e^{-2\gamma d} + (\rho^2 e^{-2\gamma d})^2 + (\rho^2 e^{-2\gamma d})^3 \dots \right] \quad (5.28)$$

This is a geometric series of the form:

$$\vec{E}(x) = \frac{E_I \tau \rho e^{-\gamma x}}{1 - \rho^2 e^{-2\gamma d}} \quad (5.29)$$

The frequency response of waves travelling in the negative direction is equal to the sum of the reflections from the rightmost boundary:

$$\overleftarrow{E}(x) = E_I \tau \rho e^{-\gamma(2d-x)} + E_I \tau \rho^3 e^{-\gamma(4d-x)} + E_I \tau \rho^5 e^{-\gamma(6d-x)} \dots \quad (5.30)$$

Again this can be re-factored:

$$\overleftarrow{E}(x) = E_I \tau \rho e^{-\gamma(2d-x)} \left[ 1 + \rho^2 e^{-2\gamma d} + (\rho^2 e^{-2\gamma d})^2 + (\rho^2 e^{-2\gamma d})^3 \dots \right] \quad (5.31)$$

Giving the geometric series:

$$\overleftarrow{E}(x) = \frac{E_I \tau \rho e^{-\gamma(2d-x)}}{1 - \rho^2 e^{-2\gamma d}} \quad (5.32)$$

Substituting (5.28) and (5.32) into (5.24) gives the analytic solution for the frequency response at x:

$$E(x) = \frac{E_I \tau (e^{-\gamma x} + \rho e^{-\gamma(2d-x)})}{1 - \rho^2 e^{-2\gamma d}} \quad (5.33)$$

The first simulation for this problem used a cavity length of 3.95m and a mesh size of 0.2m. This meant that, when using a non-conformal mesh, the cavity length must be a multiple of 0.2m and therefore the cavity modelled is effectively 4m long. When using the conformal mesh one cell can be deformed allowing a 3.95m long model while using a 0.2m global mesh size. The electric field along the cavity at 37MHz is shown in Figure 5.8. This frequency was chosen so that it did not correspond to a standing wave.

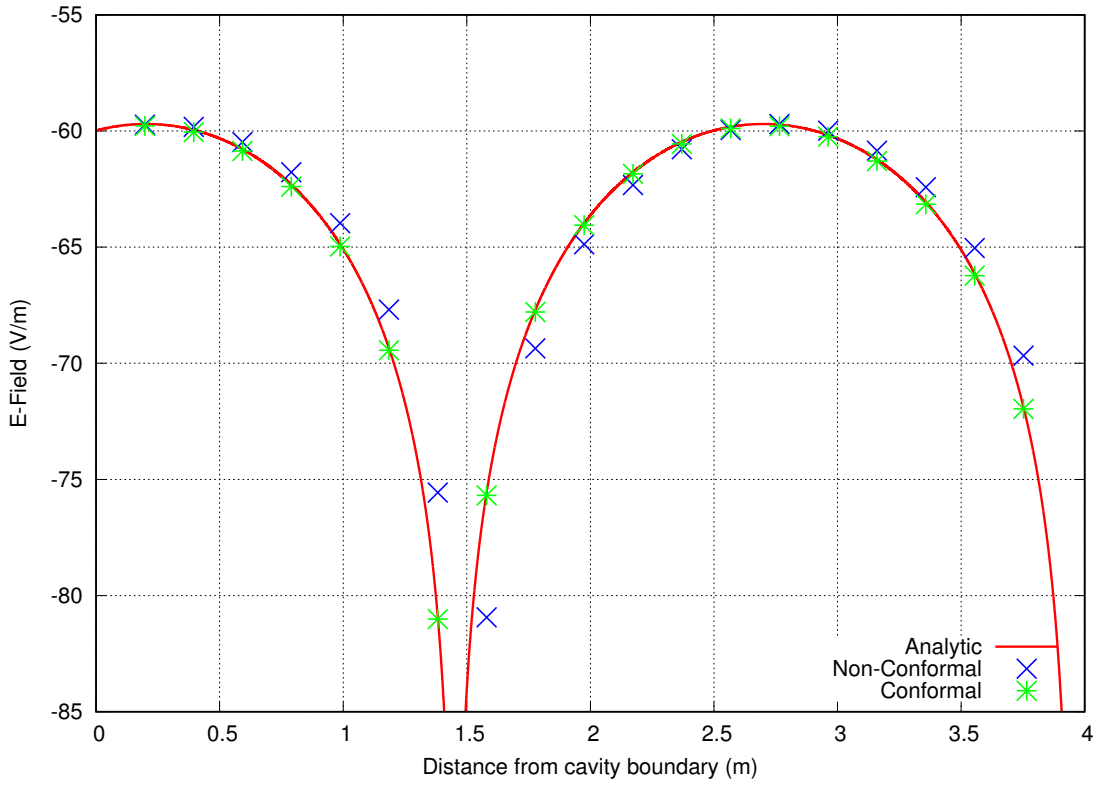


**Figure 5.8:** E-Field along 1D Cavity at 37MHz. Comparison of analytic solution with conformal and non-conformal meshes.

It can be seen that for the non-conformal case the field pattern is shifted slightly in space. However, when using the conformal mesh this has been corrected and the field values lie on the analytic curve.

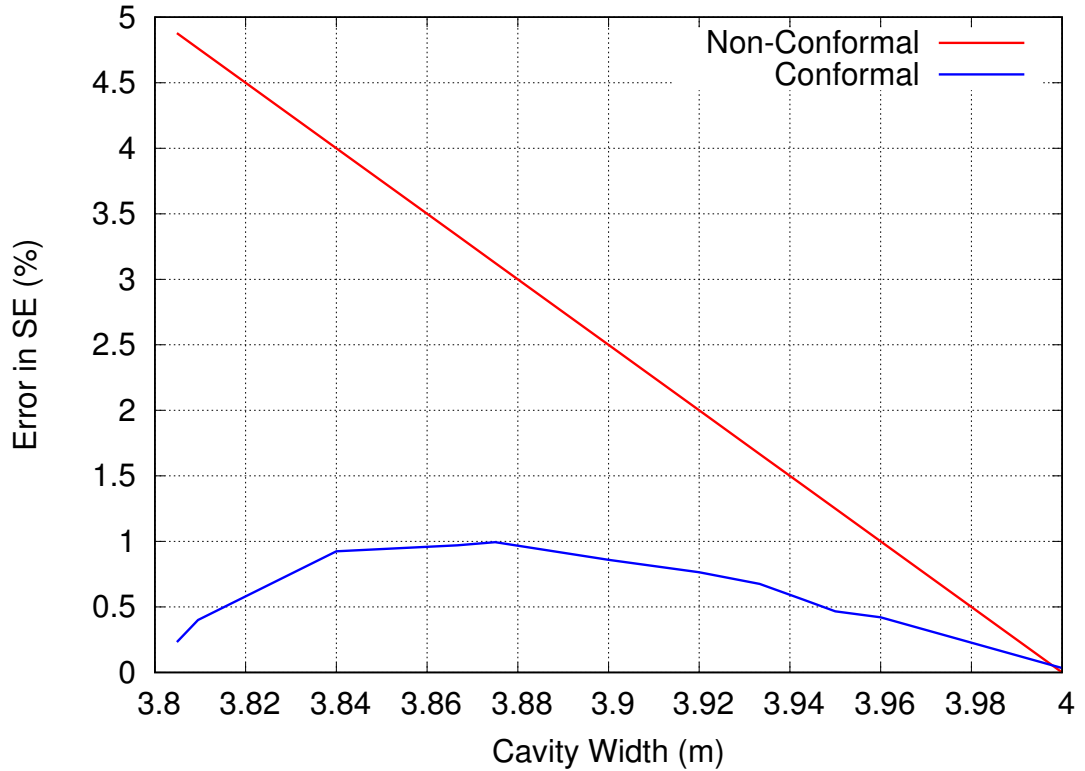


**Figure 5.9:** Error in resonant frequency for 1D cavities of different widths. The number of cells across the cavity and the mesh size remain constant.

The simulation was repeated using the same mesh size and number of cells as before, but the size of the cavity was varied from 3.81m to 4m. The error in the first resonant frequency was measured for each cavity size, the results are shown in Figure 5.9. The conformal mesh is adjusted to match the cavity width.

It can be seen that the error in resonant frequency is better in all cases when using the conformal mesh except when the cavity has a width of 4m and the conformal mesh is identical to the non-conformal mesh. A width of 3.8m does not need to be simulated using the conformal mesh as the boundary would lie exactly on the next surface of the cell, meaning the distance between the electric field nodes and the boundary would be zero. There is also an issue with stability when the cell is highly distorted, this is discussed further in Section 5.6.

### Cubic Shell Test Case

To test the conformal algorithm on a three dimensional problem, a 1m cubic cavity was investigated. It is possible to mesh a cubic shell so that it aligns perfectly with the grid, obviating the need for a conformal mesh. However, if the cube is not aligned with the mesh it may become necessary to use a conformal, or stair-cased, mesh to represent the faces of the cube as shown in Figure 5.10.

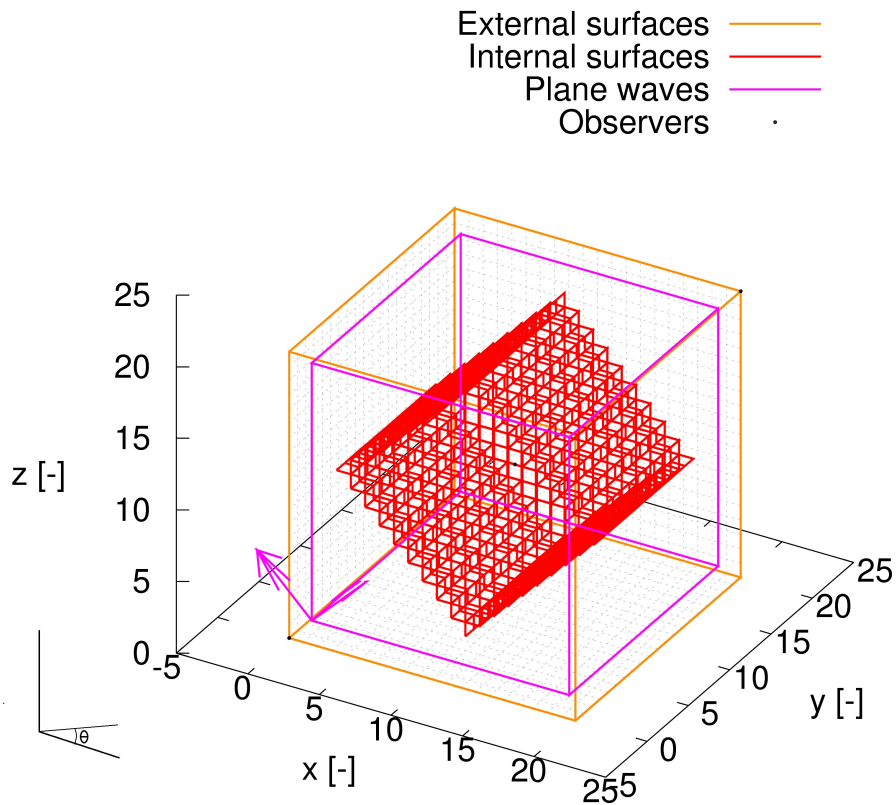


**Figure 5.10:** Stair-cased mesh of cubic shell for FDTD using 100mm grid. PML boundaries are used to terminate the edges of the problem space. The scattering angle  $\Theta$  is shown corresponding to Figure 5.17.

In this case the cube has been rotated  $45^\circ$  around its  $y$ -axis causing four of the faces to become misaligned and require a stair-cased mesh. The boundary properties are the same as those used in Section 5.4.1. The cube is illuminated using a  $y$ -polarised plane wave, at normal incidence to the face of the cube. The electric field at the centre of the cube is monitored. From this the SE at the centre of the cube is determined and shown in Figure 5.11. As there is no analytic solution for a cubic shell, a simulation of the cube that is aligned to the FDTD grid is used for comparison. For the aligned case no stair-casing is needed and the conformal mesh reduces to the standard algorithm.

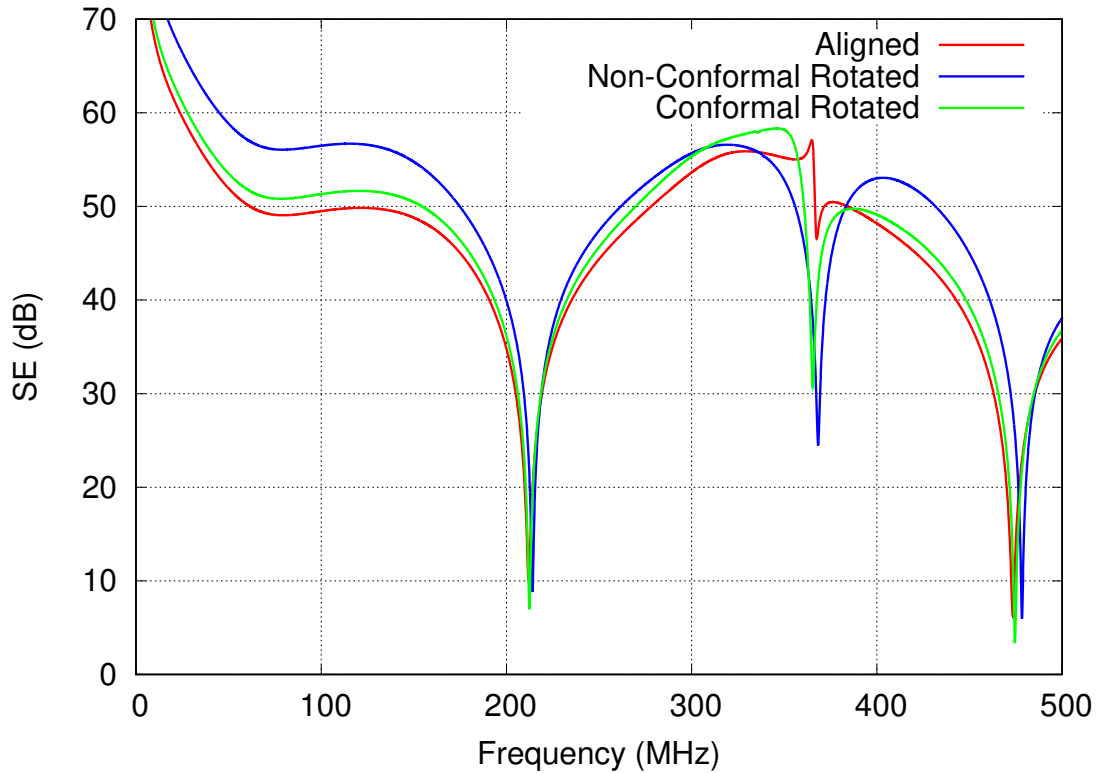


**Figure 5.11:** Shielding effectiveness at the centre of a cubic shell rotated  $45^\circ$  with respect to the FDTD grid. Comparisons are made with an aligned case.

There is a significant improvement in the accuracy of the magnitude of the SE using the conformal mesh when compared to the stair-cased mesh, reducing the difference between the rotated and aligned meshes from 7 dB to approximately 1.5 dB at 100 MHz. This frequency has been chosen to measure the improvement as it is not near a resonance where slight shifts in frequency can result in large changes in the SE. The root mean square deviation (RMSD) error for the non-conformal case in Figure 5.11 is 6.22 dB; in comparison the RMSD for the conformal case is 3.26 dB. A close up of the first resonance in Figure 5.12 shows an error in the resonant frequency for the stair-cased mesh of around 1%; when using the conformal mesh this is reduced to approximately 0.1%. Although the resonant frequency is more accurate with the conformal mesh the amplitude error suggests there is still some inaccuracy in the transmission and reflection coefficients achieved. A potential contribution to the error is the use of a plane-wave that is not aligned to the mesh [6].

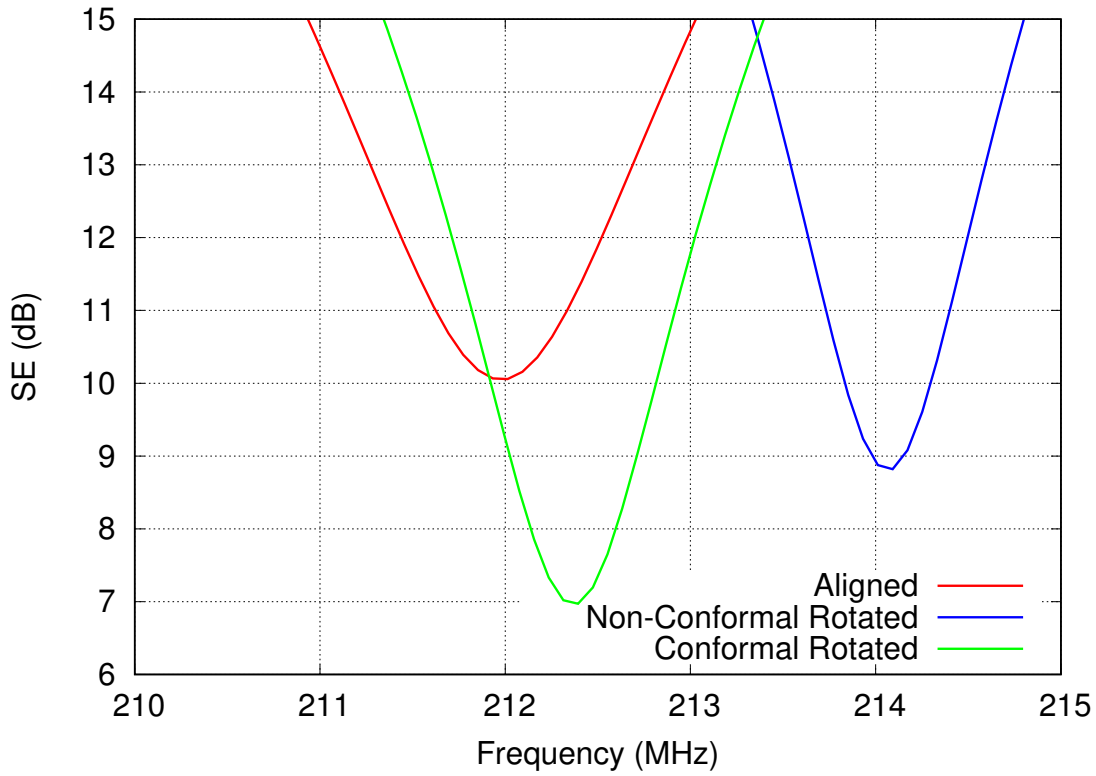


**Figure 5.12:** Shielding effectiveness at the first resonant frequency of the cubic cavity.

### Cylindrical Shell Test Case

A third test case is shown to demonstrate the use of the conformal algorithm when modelling curved surfaces. An infinite cylindrical cavity has been meshed with a radius of 1m using the same boundary conditions as the previous test cases. Again the cavity is illuminated using a linearly polarised plane wave, with the incident electric field being polarised along the  $x$ -axis. Perfect Magnetic Conductor (PMC) boundaries are utilised at each end of the cylinder to simulate an infinitely long structure. The mesh size for this problem is 0.1m.

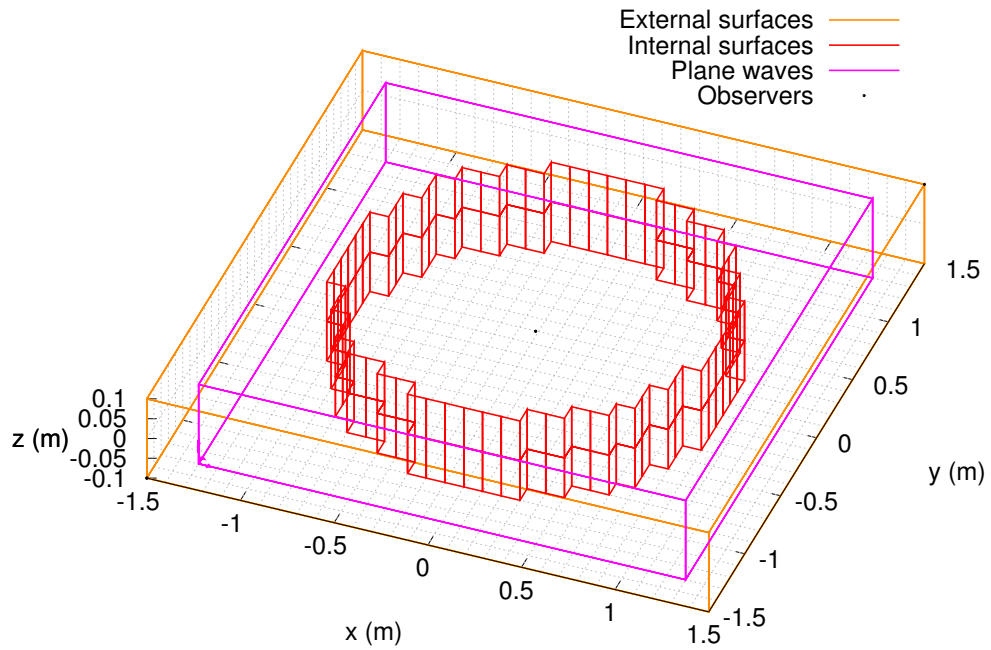


**Figure 5.13:** Stair-cased mesh of an infinite cylinder for FDTD. Only one layer of cells is required in the  $z$ -direction, PMC boundaries emulate an infinite length.

Again the E-field, and subsequently SE, is measured at the centre of the cavity. In this case there is an analytic solution [3] that can be used for comparison. The results are shown in Figure 5.14

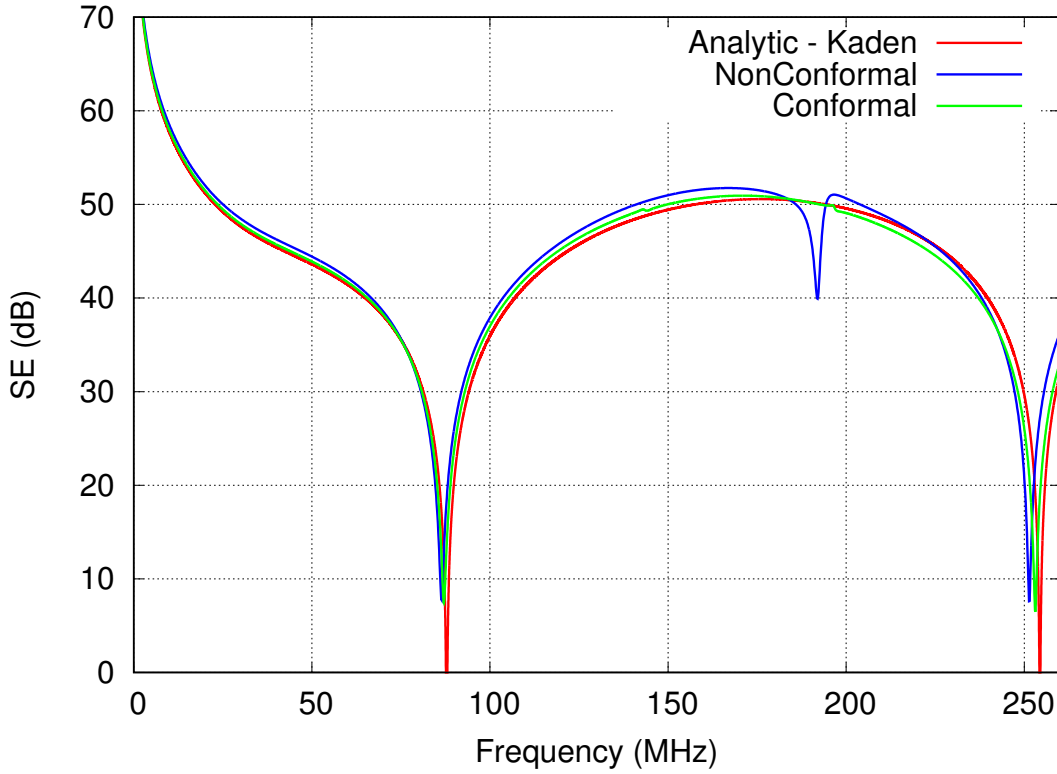


**Figure 5.14:** Shielding effectiveness at the centre of the cylindrical cavity comparing non-conformal and conformal meshes to an analytic solution.

For the non-conformal mesh there is a clear resonance around 180 MHz. This is not a spurious peak, rather it corresponds to a resonant mode that has a node at the centre of the cavity. For points within the cavity that are not exactly at the centre, this resonance would be visible in the SE. The imprecise stair-cased approximation makes the centre of the mesh a slightly ambiguous position causing this resonance to become apparent at the centre as well. Using the conformal mesh has reduced this resonance significantly, making it almost non-existent at the centre of the cylinder. However, it should be noted that there is still a slight variation in the SE around this frequency as the conformal mesh is still an approximation, albeit a more accurate one than the stair-cased mesh.

The error in the first resonant frequency is around 1.9% when using the stair-cased mesh, using the conformal mesh gives an error of approximately 0.4%. The error in magnitude at 50 MHz, again chosen to be minimally affected by resonances, is approximately 0.9 dB using the stair-cased mesh, this error is improved to approximately 0.3 dB using the conformal mesh. The RMSD for the non-conformal mesh in Figure 5.14 is 1.2 dB, for the conformal mesh it is 0.6 dB.

It is worth mentioning that for the stair-cased mesh the extra resonance could be reduced, and the overall accuracy in frequency increased, using a higher resolution mesh. However, to achieve a result comparable to the conformal algorithm a mesh size of 0.025m

was required. The increased number of nodes and subsequent increase in number of iterations increased the runtime of the simulation by a factor of approximately 256. There would also be no improvement in the magnitude of the SE as errors in the boundary transmission and reflection due to stair-casing are independent of mesh size[79].

### Spherical Shell Test Case

A spherical cavity was used to test the performance of the algorithm when dealing with doubly curved surfaces. A stair-cased mesh of a 1m radius spherical cavity, using the previously described boundary conditions, was automatically generated [59]. The stair-cased mesh has been adapted to the conformal mesh by moving the individual cell faces to lie on the surface of the analytic sphere as shown in Figure 5.15.

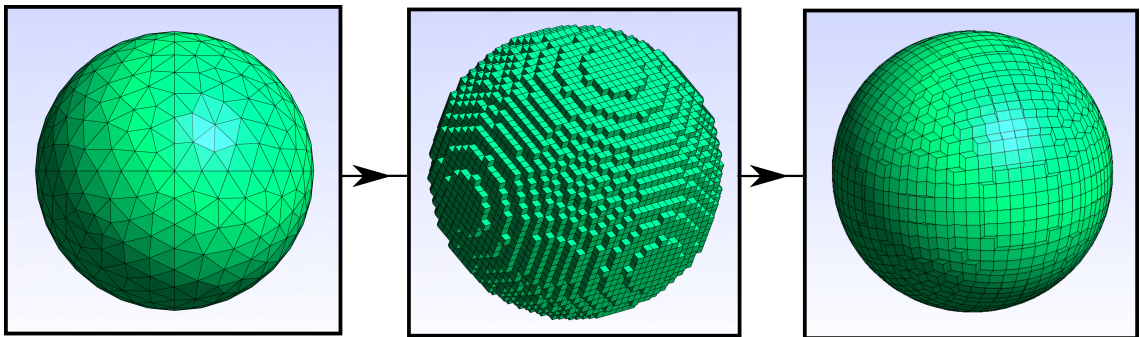


**Figure 5.15:** Example of a stair-cased mesh of a sphere adapted to the conformal algorithm.

As before, the cavity is illuminated using a linearly polarised plane wave with an  $x$ -directed E-field, PML boundaries were used to terminate the problem space. The SE at the centre of the cavity was recorded and is compared to an analytic solution[3] in Figure 5.16.

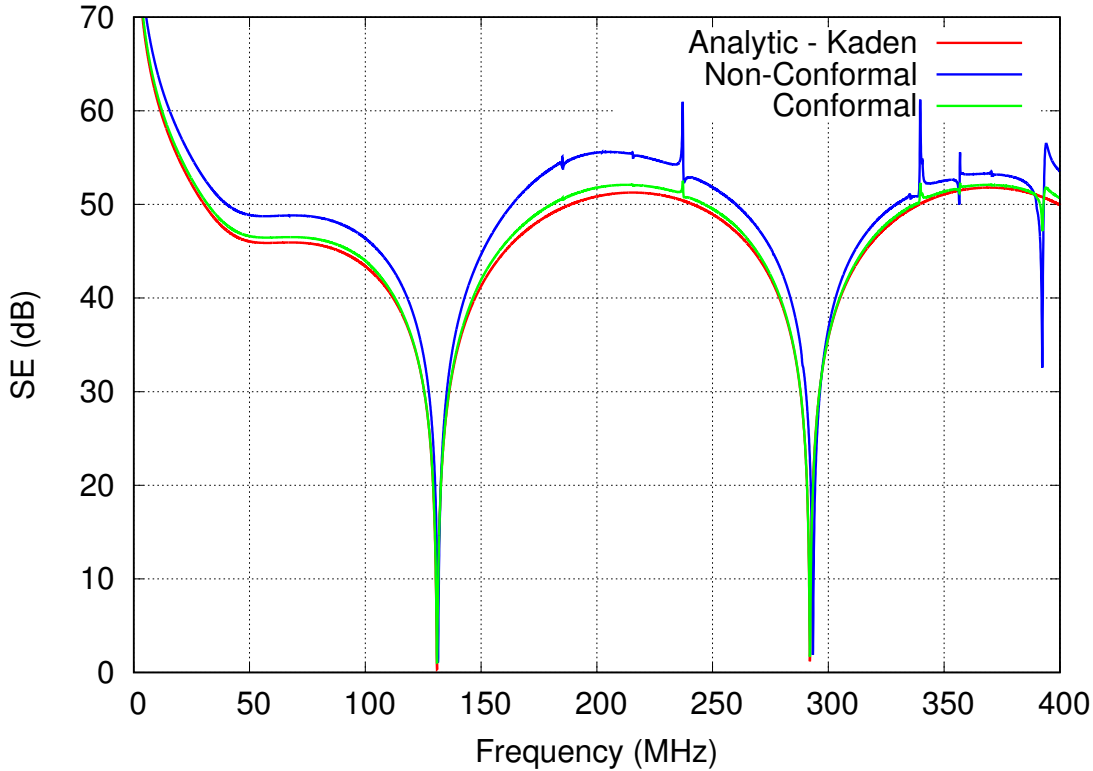


**Figure 5.16:** Shielding at the centre of the spherical cavity comparing non-conformal and conformal meshes to an analytic solution.

Spurious resonances are a significant and common error when using a non-conformal mesh. At these frequencies there is a resonance that has a node at the centre of the cavity. The analytical solution assumes a mathematically perfect sphere, however, for both the non-conformal and conformal meshes a numerical approximation to a sphere is used; the field at the centre of the sphere is highly sensitive to changes in the structure of the sphere [79]. The conformal algorithm shows a significant reduction in the size of these resonances as the approximation is much closer to a perfect sphere.

There are also reductions in the error for both the SE magnitude and resonant frequencies as seen in previous examples. The error in magnitude has been improved from 3 dB to approximately 0.5 dB at 75 MHz with the RMSD being reduced from 3.45 dB to 0.59 dB; the error in frequency of the first resonance has been reduced from around 3% to less than 0.1%.

#### 5.4.2 Scattering from Cavities

While much of the focus of this thesis is upon dealing with the effects of stair-casing on shielding problems, scattering from stair-cased surfaces is also of interest to many FDTD users. This section details two scattering test cases, the first is a cubic shell to demonstrate scattering from planar surfaces and sharp corners. The second case is a spherical shell

with a highly curved symmetrical surface. To measure the scattering from the shells the field is recorded on a cubic surface near the boundaries of the problem space. The surfaces fields are then imported into CST and a far field transformation is then applied to the field to determine the field at a distant point from the cavity.

### **Cubic Shell Test case**

The first scattering test case is a hollow cubic shell. This is identical to the cube shielding test case in Section 5.4.1. In this case the scattering from the shell was recorded and Figure 5.17 shows the far field scattering in the YZ plane centred on the cube, comparisons are made between a cube rotated  $45^\circ$  to the grid using both a stair-cased and conformal mesh with a cube aligned to the grid. For this case there is no analytic solution to the shielding effectiveness of the cube so the result from the aligned case is used for comparison. At  $\Theta = 180$  the angle of scattering is directly back along the direction of propagation for the incident wave. It can be seen that the stair-cased mesh produces a result with significant variation in comparison to the aligned case, this is most apparent near the resonances. The conformal algorithm more closely matches the aligned case, with clear resonances that emulate the aligned case. Away from the resonances the conformal algorithm provides a more accurate magnitude of the scattered field. At  $\Theta = 180$  an error of 2 dB for the stair-cased mesh is reduced to 0.8 dB using the conformal mesh. Similarly at  $\Theta = 0, 360$  an error of -2.6 dB is reduced to -0.4 dB. As the direction of error varies between  $\Theta = 0$  and  $\Theta = 180$  it is apparent that the reduction in error is not caused by a translation of the scattered field, but that the conformal mesh more accurately represents the model.

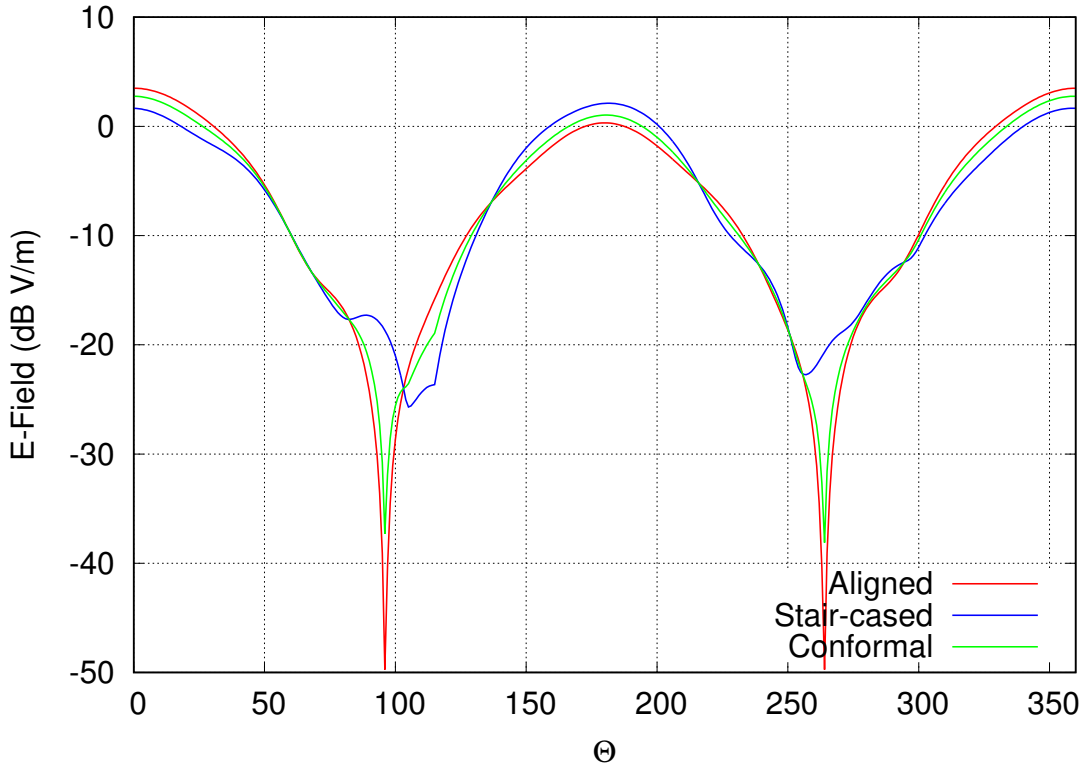


**Figure 5.17:** Scattering from the cubic cavity, rotated  $45^\circ$  with respect to the mesh, in the  $yz$ -plane comparing non-conformal and conformal meshes to an aligned cube solution.

### Spherical Shell Test Case

The spherical test case used for the scattering analysis is the same as the one used for the correction factor validation in Section 4.5.2. Figure 5.18 shows the recorded far field scattering of the E-field in the YZ plane from the sphere. The angle  $\Theta$  refers to the angle of scattering where  $180^\circ$  is a reflection along the normal to the angle of incidence. It can be seen in Figure 5.18 that the magnitude of the scattered field is much closer to the analytic solution when using the conformal algorithm, with a reduction in error from around 2 dB to approximately 0.2 dB for the main peak. There is also significant reduction in the error of the subsidiary peaks, with errors up to 5.5 dB being reduced to less than 1 dB at  $110^\circ$  and  $250^\circ$ .

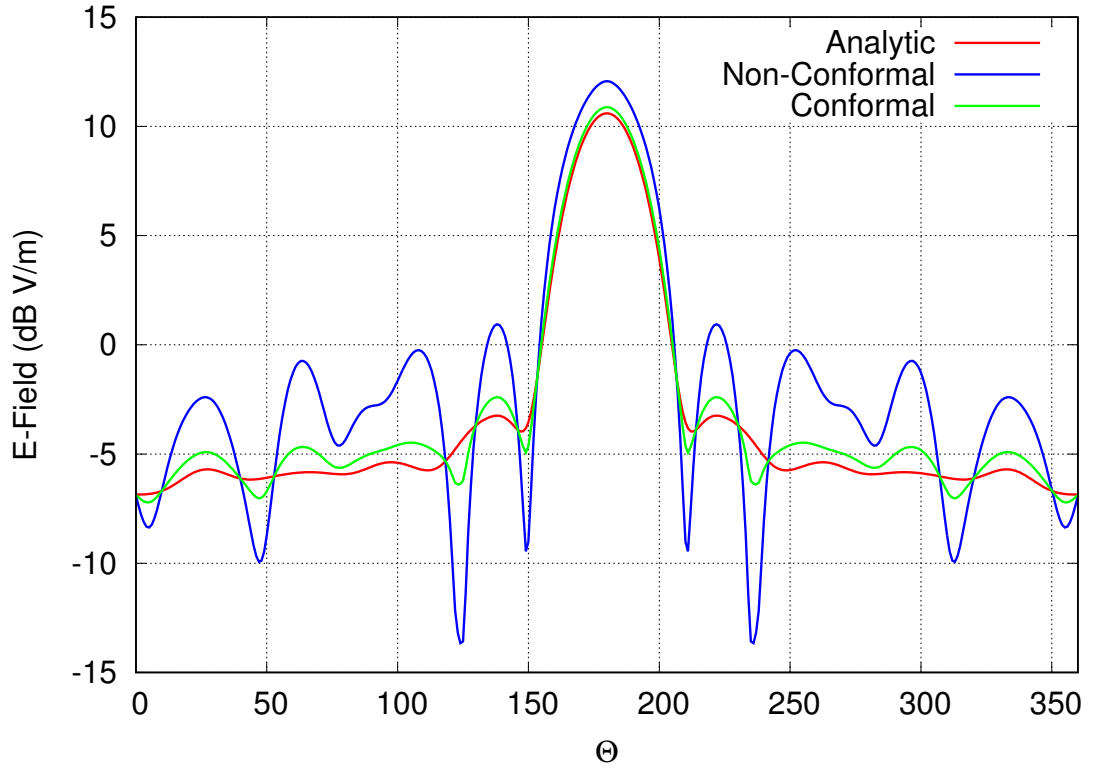


**Figure 5.18:** Scattering from the spherical cavity in the  $yz$ -plane comparing non-conformal and conformal meshes to an analytic solution.

### 5.4.3 Anisotropic Conformal Boundaries

The thin boundary model used as a basis for the conformal algorithm[1] has the ability to represent anisotropic materials such that the behaviour of the material depends on the polarisation of the incident electromagnetic field. The anisotropic properties are simulated by resolving the tangential fields determined by (5.21) into TE and TM components as shown in Figure 2.4 and applying the boundary to the components.

The algorithm that has been proposed inherently incorporates the anisotropic capabilities of the base model. The cube mesh in Section 5.4.1 was used to test the accuracy of the anisotropic behaviour of the conformal mesh. In this case the transmission and reflection coefficients of the material for  $z$ -polarised E-field were set to 0.002 and -0.992 respectively, the transmission and reflection coefficients of the boundary for the E-field perpendicular to the  $z$ -axis and parallel to the boundary were set to 0.006 and -0.988. The stair-cased mesh used for this model is the same as in Figure 5.10.

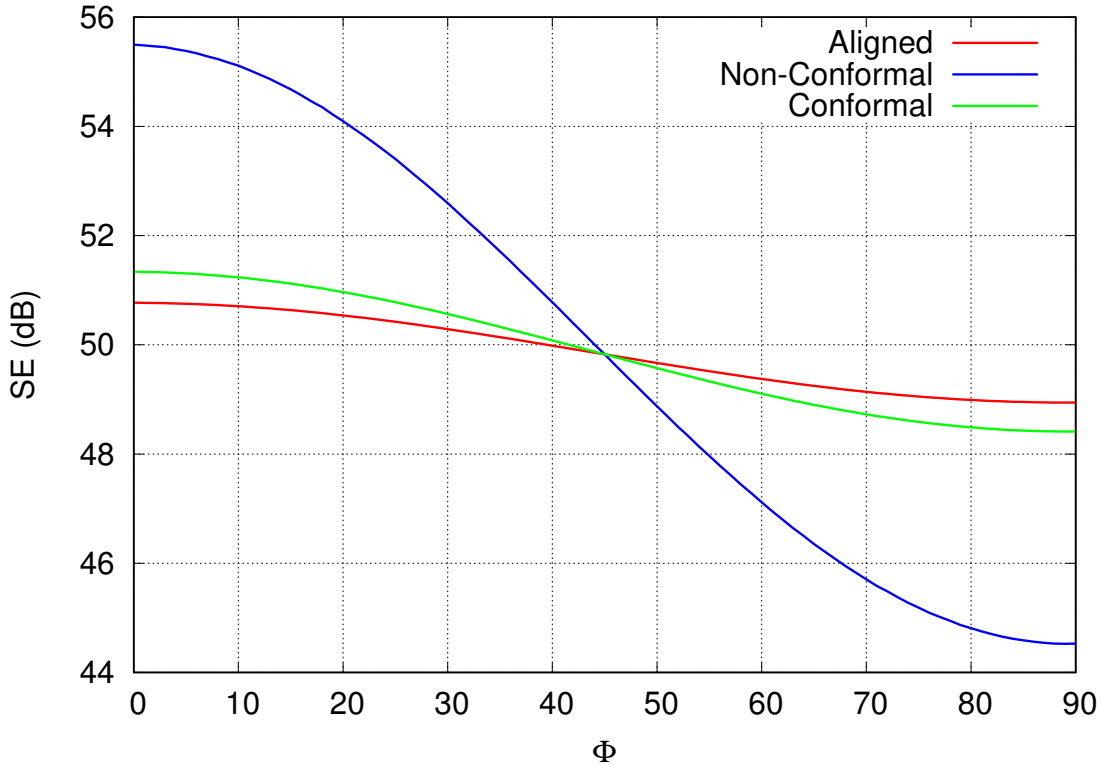


**Figure 5.19:** Shielding effectiveness at the centre of cubic mesh at 100MHz for different E-field polarisations comparing non-conformal and conformal meshes to an aligned mesh. 0 degrees corresponds to a  $z$ -polarised E-Field.

The cube was illuminated using linearly polarised plane waves with the angle of the E-field polarisation varying between  $0^\circ$  ( $z$ -axis) and  $90^\circ$ . The SE was determined and compared to the aligned case as in Section 5.4.1. Figure 5.19 shows the SE at 100MHz for different angles of polarisation. This frequency was chosen as it is not near a resonant frequency and therefore less susceptible to frequency shift from using stair-cased and conformal meshes. The error in SE magnitude is greatest at  $\phi = 0$  and  $\phi = 90$  and at these angles the error has been reduced from over 4 dB to less than 1 dB. The RMSD for the non-conformal mesh is 3.25 dB, this has been reduced to 0.39 dB using the conformal mesh.

## 5.5 Generating Conformal Meshes

The cases used to validate the proposed conformal algorithm are all simple geometric shapes. The reason for this is that it is easy to generate the deformation lengths used by the algorithm for a known, mathematically defined shape by hand or using simple scripts. However, for complicated geometries such as an aircraft fuselage, it is not feasible to create conformal meshes manually. Therefore, for the proposed algorithm to be useful

beyond basic applications, there is a need for a means to automatically generate conformal meshes from unstructured meshes. Conformal mesh generation has been explored for PEC [80, 81] algorithms, however, a new method must be devised to apply to the conformal algorithm. Presented here is a proposed method of adapting stair-cased meshes to the conformal algorithm.

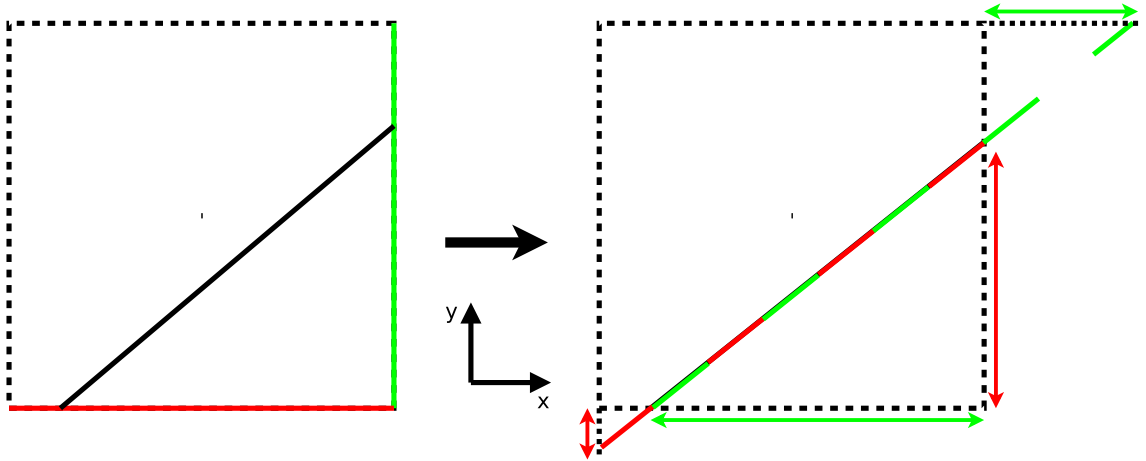


**Figure 5.20:** Adaptation of a stair-cased mesh to the conformal algorithm for a single cell.

Figure 5.20 shows a single FDTD cell. The solid black line is a surface to be meshed that is misaligned to the FDTD grid. The green line represents a face centred SIBC normal to the x direction, the red line represents a face centred SIBC normal to the y direction. The cell on the right shows a cell adapted to the conformal mesh, the edges of the y normal face have been deformed in the y direction to conform to the surface by a distance marked by the red arrows. Similarly, the edges of the x normal face have been deformed in the x direction to conform to the surface by a distance marked by the green arrows. Both faces are required so as to account for all polarisations of E-field.

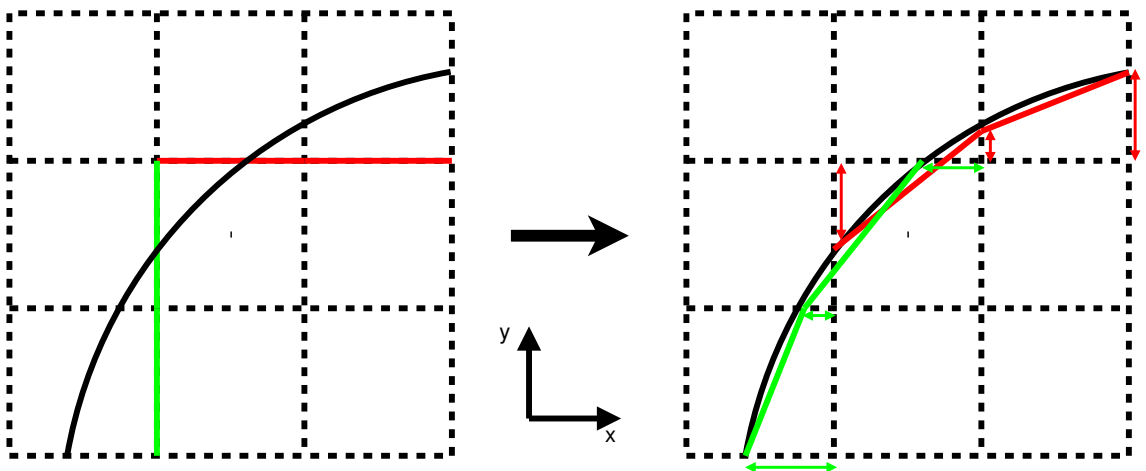


**Figure 5.21:** Adaptation of a stair-cased curve to the conformal algorithm.

To mesh a continuous surface over multiple cells this process must be carried out for

each cell. Figure 5.21 shows a curved surface stair-cased mesh that has been adapted for the conformal algorithm. Again, the deformation lengths are marked by appropriately coloured arrows. The curve being meshed is an arc of a circle, as such there is a clear mathematical definition and it is trivial to determine the values of the deformation lengths as a difference between the edges defined by the stair-cased mesh and the analytic expression for the curve. However, if the surface is not easily mathematically described the meshing becomes more difficult. Figure 5.22 shows an arbitrary surface being meshed. In this case the deformation lengths are again the difference between the stair-cased mesh and the surface, however without an analytic expression to describe the surface each distance must be calculated manually.

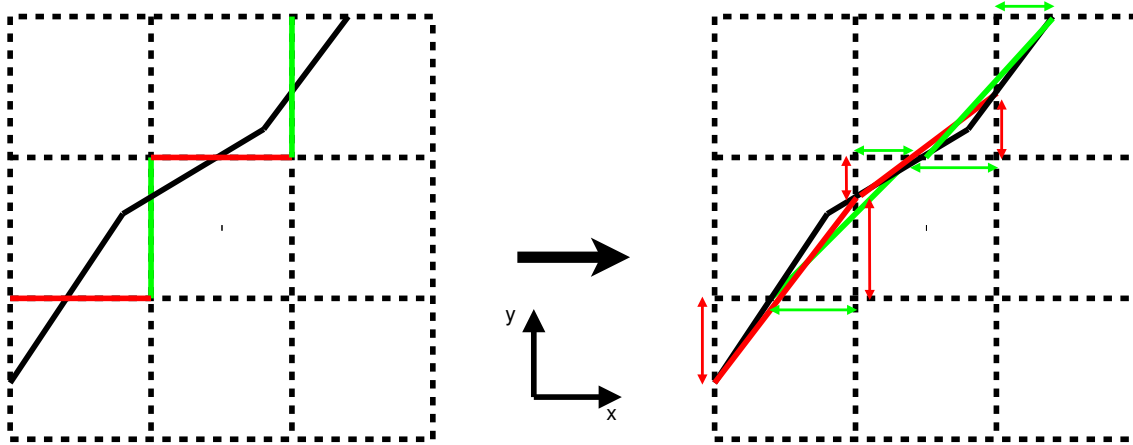


**Figure 5.22:** Adaptation of a stair-cased arbitrary surface to the conformal algorithm.

## 5.6 Instability due to Highly Deformed Cells

As noted in the 1D test case the proposed algorithm can have stability issues when using highly distorted cells. The distortion of cell is a measure of how much the boundary of the cell has been moved, for this algorithm the distortion of a single edge of the cell is given by:

$$D_s = 1 - \delta_s \quad (5.34)$$

Where  $\delta_s$  is the fractional edge length from (5.22).

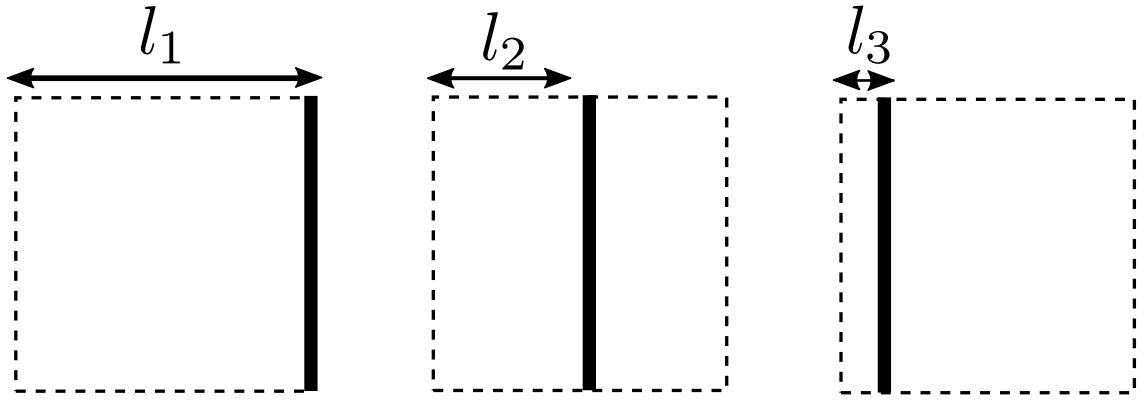


**Figure 5.23:** 3 FDTD cells with SIBC faces,  $l_1$ ,  $l_2$  and  $l_3$  are the deformed cell widths with values of  $\Delta$ ,  $0.5\Delta$  and  $0.025\Delta$  respectively.

Fig. 5.23 shows 3 different FDTD cells with an SIBC face, the first has a SIBC that lies on the cell boundary, in this case the deformation is 0 and the algorithm reduces to the non-conformal version. In the second case the deformation is 0.5 and for the final case the deformation is 0.975. Empirical testing using the 1D test case from Section 5.4.1 showed that for deformation values higher than 0.95 the algorithm would become unstable, causing exponential growth in energy. Further testing using the 3D cube and sphere models suggested that the limit of cell distortion along a given edge can be no higher than 0.9.

Problems with highly distorted cells has been identified, usually related to limits imposed on the time step [74, 82, 83]. To address the issues with stability for the proposed algorithm limits have been applied that cap the deformation of a given cell to 0.9, this method is similar to an approach that has been applied to the DM method [84].

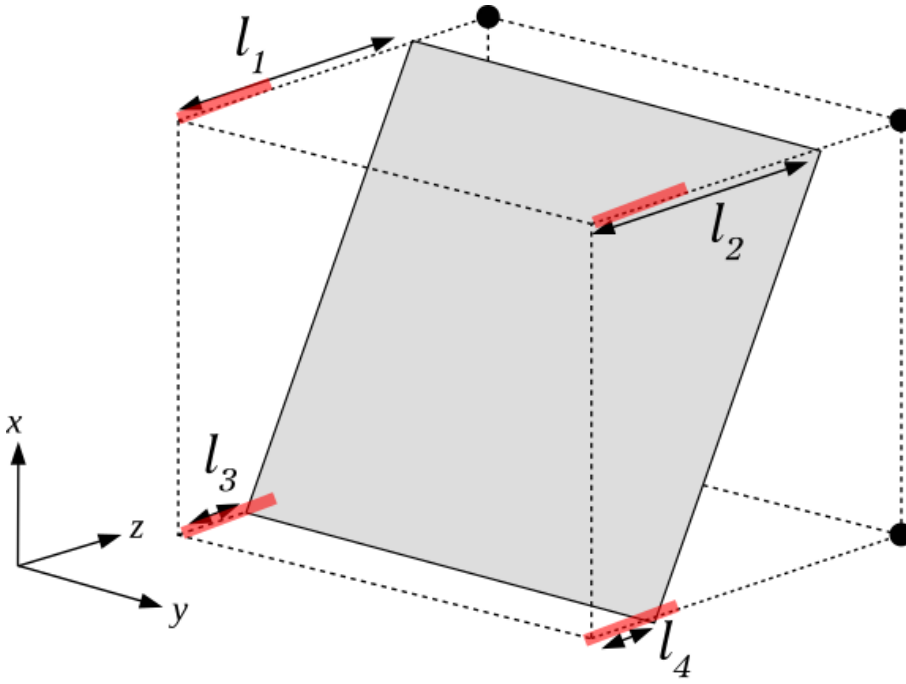


**Figure 5.24:** Conformal algorithm applied to a single cell. The shaded surface violates the 'forbidden zones' that could lead to instability.

Figure 5.24 shows a 3D deformed cell. The sections highlighted in red are *forbidden zones* where the deformation would be greater than 0.9. It can be seen that the deformations along the bottom two  $z$ -directed axes denoted by  $l_3$  and  $l_4$  are in the forbidden zones and therefore at risk of instability. The suggested correction would be to adjust the cell deformation as shown in Figure 5.25. The lengths  $l_3$  and  $l_4$  have been changed to be equal to the length of the forbidden zone, capping the deformation at 0.9, this does mean that the conformal mesh does not fully align with the surface being meshed, but this should a small accuracy penalty as the difference is small compared to the width of the cell. It may be possible in this case to adjust the mesh size of the global grid, doing so could allow a conformal mesh without the adjusting the surface to avoid forbidden zones. However, this could cause issues when meshing other conformal cells and so a mesh size must be chosen that minimises the number of conformal cells that have conflicts with forbidden zones.

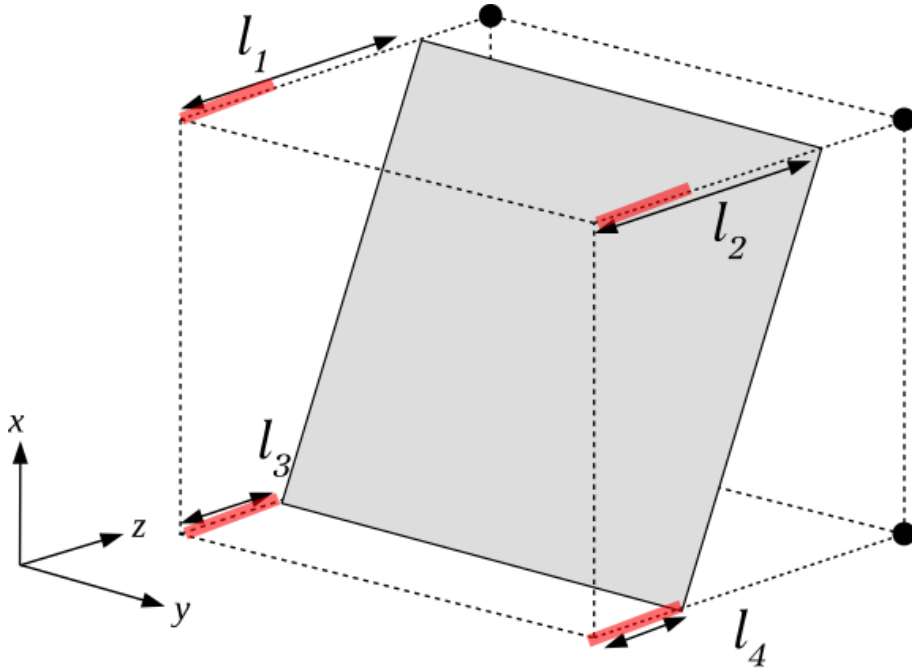


**Figure 5.25:** Conformal algorithm applied to a single cell. The shaded surface has been moved so that it no longer violates the 'forbidden zones' to avoid potential instability.

## 5.7 Summary

This chapter has discussed multiple pre-existing conformal algorithms for FDTD. These algorithms are based on the popular Dey-Mittra algorithm for PEC surfaces and most of the algorithms referenced are solely PEC materials. A conformal algorithm for penetrable materials by Yu and Mittra has also been presented, however this algorithm can only be applied to bulk materials, requiring multiple cells across each dimension of the material being modelled. A new conformal algorithm has been proposed that utilises a SIBC to obviate the need for cells within the material being modelled. This is appropriate for modelling curved and non-aligned surfaces that are much thinner than the desired cell size and allows for much more efficient simulations when compared to bulk material algorithms.

Multiple test cases have been presented to show the reduction in error due to the proposed algorithm when compared to stair-cased equivalents. Four test cases were used to demonstrate the improvements for shielding problems. The first case was a 1D resonator used to demonstrate a simple case, the results from this showed that for different points across the entire width of the cavity the magnitude of E-field for a given frequency was more accurate using the conformal algorithm except for the case that the 1D cavity boundaries lay on the FDTD grid, in this case there was no difference in result as the conformal algorithm reverts to the base SIBC algorithm. Three 3-D cavity models were used to show the performance of the algorithm on the shielding of cavities. The cube, cylinder,

and spherical cavities utilise planar, singly curved and doubly curved surfaces respectively. In each of these cases the error in resonant frequency, magnitude of the SE and magnitude of spurious resonances was reduced significantly. The cube and sphere cases were also used to measure the performance of the algorithm for scattering problems, for these cases error in magnitude of the scattering was improved.

The limitations of the algorithm has been discussed. It has been identified that there is a risk of instability for problems with high amounts of distortion for individual cells and it has been proposed that the distortion of the cell be capped to prevent instabilities at the risk of minor accuracy penalties. This instability has also been observed in the popular Dey-Mitra method [70] and variations limiting the instability [73] have been shown to have accuracy penalties. As existing methods deal with bulk materials and the proposed method uses thin boundary models there is no direct comparison between the existing and proposed methods. The generation of conformal meshes from stair-cased models has been discussed. Without an automated mesh generation tool the usable potential of the algorithm is limited to simple geometries. It has been suggested that an existing stair-cased mesher could be adapted to generate conformal meshes, however this is further work that is yet to be carried out.

# Chapter 6

## Conclusions and Further Work

The work in this thesis is focused on identifying the errors that arise when meshing curved and non-aligned for FDTD simulations and developing methods to mitigate those errors.

### 6.1 Original Contributions

#### 6.1.1 Corrections to a Face Centred SIBC Algorithm

A pre-existing anisotropic face centred thin boundary model has been presented. Modifications have been made to the pre-existing algorithm to account for field contributions from the SIBC at edges and corners that previously were not included. These corrections have been shown to further improve on the accuracy of the spherical shell test case and a generic algorithm for dealing with different edge cases has been presented to allow for easy implementation.

#### 6.1.2 Investigations into Stair-cased Cavities

The errors that arise in FDTD simulations of stair-cased cavities has been investigated. These investigations have focused on areas that are not sufficiently covered in pre-existing literature, specifically the effect of stair-casing on shielding and the transmission/reflection of stair-cased conductive boundaries. There is a shift in the frequency of resonances of shielding cavities as result of the inaccuracies in the physical position of boundary nodes relative to the surface. The difference in boundary node position also results in the appearance of spurious resonances at those positions and frequencies that are resonant nodes. It has been shown that the surface area of a stair-cased surface is higher than the surface being modelled. The increase in surface area alters the transmission and reflection coefficients of the surface by a calculable amount. Investigations into the scattering from stair-cased boundaries have shown significant errors in the magnitude of scattered field

and errors in the angle of scattering.

### **6.1.3 A Correction Factor for Stair-cased Boundaries**

A corrective method has been developed to adjust the transmission and reflection coefficients of boundaries to counteract the errors in the sheet resistance of thin material sheets due to stair-cased meshing. A simple correction has been determined for planar sheets that are rotated around a single axis relative to the FDTD grid and a more complex correction has been determined for planar sheets that have been rotated around two axes relative to the FDTD grid. A cubic shell test case has been used to demonstrate the improved effect that both corrections have on shielding problems with stair-cased planar surfaces. A method has also been demonstrated for applying the corrections to curved surfaces using segmented areas with different correction factors applied. The value of this method has been shown using singly curved and doubly curved test cases. The method has also been shown to have a positive effect in reducing the errors in scattering from stair-cased surfaces.

### **6.1.4 A Conformal Algorithm Incorporating a Thin Boundary Model**

A conformal algorithm has been developed that incorporates a face centred SIBC model. Unlike pre-existing conformal algorithms, the new method allows for the modelling of material sheets that are thinner than the cell size of the FDTD grid, this means that a much coarser mesh can be used compared to bulk conformal methods significantly reducing computational costs, making otherwise prohibitively expensive problems feasible to model. The proposed algorithm has been validated for shielding problems using planar, singly curved and doubly curved surfaces and there is a significant reduction of the errors in resonant frequency, magnitude of SE, magnitude of scattered field and magnitude of spurious resonances for these cases when compared to a stair-cased equivalent. The underlying SIBC model for this algorithm incorporates anisotropic functionality, the conformal algorithm presented can also represent anisotropic materials and this has been validated using a cubic shielding test case rotated relative to the FDTD grid with anisotropic boundaries.

### **6.1.5 Potential Applications**

Methods currently exist for the simulation of conformal bulk materials and stair-cased sub-cell materials. The new methods presented in this thesis have sought to combine the accuracy of conformal methods with the efficiency of sub-cell methods. This is especially valuable in multi-scale simulations such as modelling a cavity with a shell much thinner than the dimensions of the cavity. As such the work presented here can be useful for

modelling scenarios such as antennas, cables, electronic equipment enclosures and vehicles such as aircraft.

## **6.2 Recommendations for Further Work**

This section suggests areas of further work to expand on the areas explored in this thesis. The recommendations mainly focus on making the new methods presented viable for problems more complex than basic geometric shapes.

### **6.2.1 Incorporating the Correction Factor Method into the Meshing Process**

Currently the correction factor suggested in Chapter 4 must be manually applied by the user. To improve the usability of this method the correction factor can be incorporated into the meshing process. The mesher[59] used to generate the stair-cased models used throughout this thesis works from an unstructured mesh created using computer aided design (CAD) software [85]. The surface of an unstructured mesh is comprised of a series of triangular faces. When the mesher places the stair-cased faces it can determine the angle of the unstructured mesh at that point relative to the FDTD grid, this information can be extracted and used to calculate the appropriate correction factor for that surface. This could easily be applicable to curved surfaces using the segmented surface method described in Chapter 4.

### **6.2.2 Applying the Correction Factor to Frequency Dependent Media**

All of the correction factor test cases in this thesis have used frequency independent media, this is due to the fact it is easier to apply the correction factor in these cases. For frequency dependent materials there are two suggested options for applying the correction factor:

- The face centred thin boundary model can represent frequency dependent materials using an impedance matrix that is fitted to a partial fraction expansion. By adjusting the impedance matrix to incorporate the correction factor, the fitted partial fraction expansion applied to the SIBC would counter the stair-casing errors as for the frequency independent case. This would be a more complicated process and may be difficult for users who are not experienced in the area.
- The correction factor, instead of being applied to the transmission and reflection coefficients, could be applied to the E-field calculated on the surface of the SIBC. The advantage of this option is that it would be very user friendly as all the user

would have to input is the angle of the surface to the FDTD grid, if combined with the automated meshing process suggested above the entire process would become automatic with no special action required by the user. However, altering the FDTD would be more work for a developer and would increase computational costs in a way that adjusting material values does not.

### **6.2.3 Adapting a Pre-existing Stair-cased Mesher to Produce Conformal Meshes**

It was noted in Section 5.3 that for complex problems it is currently necessary to manually determine deformation lengths to create a conformal mesh. For a problem covering hundreds or more cells it is infeasible to do this by hand. It is proposed that the stair-cased mesher can be adapted so that, while generating the stair-cased mesh, a list of deformation lengths is also produced. As the mesher is already required to determine the position of the surface being meshed relative to the grid so as to correctly place the SIBC face, all of the necessary information is available to calculate the deformation lengths allowing for complex problems to be modelled using the conformal algorithm.

# Appendix I.

## List of Abbreviations

<b>Abbreviation</b>	<b>Meaning</b>
<i>BCK</i>	Benkler-Chavennes-Kuster
<i>CAD</i>	Computer Aided Design
<i>CEM</i>	Computational Electromagnetics
<i>CFC</i>	Carbon Fiber Composite
<i>CFL</i>	Courant Friedrichs Lewy
<i>CFLN</i>	Courant Friedrichs Lewy Number
<i>DM</i>	Dey-Mittra
<i>FDTD</i>	Finite-Difference Time-Domain
<i>MoM</i>	Method of Moments (MoM)
<i>PEC</i>	Perfect Electric Conductor
<i>PMC</i>	Perfect Magnetic Conductor
<i>RCS</i>	Radar Cross Section
<i>RMSD</i>	Root-Mean-Square Deviation
<i>SE</i>	Shielding Effectiveness
<i>SIBC</i>	Surface Impedance Boundary Condition
<i>TLM</i>	Transmission Line Matrix
<i>YM</i>	Yu-Mittra



# Bibliography

- [1] I. D. Flintoft, S. A. Bourke, J. F. Dawson, J. Alvarez, M. R. Cabello, M. P. Robinson, and S. G. Garcia, “Face-centered anisotropic surface impedance boundary conditions in FDTD,” *IEEE Transactions on Microwave Theory and Techniques*, vol. PP, no. 99, pp. 1–8, 2017.
- [2] “Technische Universität Hamburg-Harburg. the CONCEPT-II website (2016). [online]. available: <http://www.tet.tuhh.de/concept..>”
- [3] H. Kaden, *Wirbelströme und Schirmung in der Nachrichtentechnik*. Technische Physik in Einzeldarstellungen, Springer, 1959.
- [4] J. Haggblad and O. Runborg, “Accuracy of staircase approximations in finite-difference methods for wave propagation,” *Numerische Mathematik*, vol. 128, no. 4, pp. 741–771, 2014.
- [5] J. B. Schneider, *Understanding the Finite-Difference Time-Domain Method*. Online (<http://www.eecs.wsu.edu/~schneidj/ufdtd/>), 2011.
- [6] S. D. Gedney, *Introduction to the finite-difference time-domain (FDTD) method for electromagnetics*. Morgan & Claypool, 2011.
- [7] S. J. Orfanidis, *Electromagnetic Waves and Antennas*. 2014.
- [8] J. Maloney and G. Smith, “The use of surface impedance concepts in the finite-difference time-domain method,” *Antennas and Propagation, IEEE Transactions on*, vol. 40, pp. 38–48, Jan 1992.
- [9] K. Yee, “Numerical solution of initial boundary value problems involving Maxwell’s equations in isotropic media,” *IEEE Transactions on Antennas and Propagation*, vol. 14, pp. 302–307, May 1966.
- [10] A. Taflove and M. E. Brodwin, “Numerical solution of steady-state electromagnetic scattering problems using the time-dependent Maxwell’s equations,” *IEEE transactions on microwave theory and techniques*, vol. 23, no. 8, pp. 623–630, 1975.

- [11] R. Courant, K. Friedrichs, and H. Lewy, "On the partial difference equations of mathematical physics," *IBM journal*, vol. 11, no. 2, pp. 215–234, 1967.
- [12] S. D. Gedney and J. A. Roden, "Numerical stability of nonorthogonal FDTD methods," *IEEE Transactions on Antennas and Propagation*, vol. 48, no. 2, pp. 231–239, 2000.
- [13] G. Strang, *Introduction to Linear Algebra*. Wellesley, MA: Wellesley-Cambridge Press, fourth ed., 2009.
- [14] M. Karkkainen and P. M. Ikonen, "Finite-difference time-domain modeling of frequency selective surfaces using impedance sheet conditions," *IEEE transactions on antennas and propagation*, vol. 53, no. 9, pp. 2928–2937, 2005.
- [15] M. Apra, M. D'Amore, K. Gigliotti, M. S. Sarto, and V. Volpi, "Lightning indirect effects certification of a transport aircraft by numerical simulation," *IEEE Transactions on Electromagnetic Compatibility*, vol. 50, no. 3, pp. 513–523, 2008.
- [16] X. Meng, P. Sewell, S. Phang, A. Vukovic, and T. Benson, "Modeling curved carbon fiber composite (CFC) structures in the transmission-line modeling (TLM) method," *Electromagnetic Compatibility, IEEE Transactions on*, vol. 57, pp. 384–390, June 2015.
- [17] M. Sarto, "A new model for the FDTD analysis of the shielding performances of thin composite structures," *Electromagnetic Compatibility, IEEE Transactions on*, vol. 41, pp. 298–306, Nov 1999.
- [18] M. S. Sarto, S. Greco, and A. Tamburrano, "Shielding effectiveness of protective metallic wire meshes: Em modeling and validation," *IEEE Transactions on Electromagnetic Compatibility*, vol. 56, no. 3, pp. 615–621, 2014.
- [19] V. Nayyeri, M. Soleimani, and O. M. Ramahi, "Modeling graphene in the finite-difference time-domain method using a surface boundary condition," *IEEE transactions on antennas and propagation*, vol. 61, no. 8, pp. 4176–4182, 2013.
- [20] J. Dawson, "Representing ferrite absorbing tiles as frequency dependent boundaries in TLM," *Electronics Letters*, vol. 29, pp. 791–792, April 1993.
- [21] J. F. Dawson, J. A. Cole, and S. J. Porter, "Modelling of transmission and reflection of thin layers for EMC applications in TLM," in *IEE 10th Int. Conf on Electromagnetic Compatibility*, (Warwick), pp. 65–70, September 1997. IEE conf pub 445.

- [22] P. A. Tirkas and K. R. Demarest, "Modeling of thin dielectric structures using the finite-difference time-domain technique," *IEEE transactions on antennas and propagation*, vol. 39, no. 9, pp. 1338–1344, 1991.
- [23] T. B. A. Senior, "Approximate boundary conditions," *IEEE Transactions on Antennas and Propagation*, vol. 29, pp. 826–829, Sept. 1981.
- [24] L. K. Wu and L. T. Han, "Implementation and application of resistive sheet boundary condition in the finite-difference time-domain method [EM scattering]," *IEEE Transactions on Antennas and Propagation*, vol. 40, pp. 628–633, Jun 1992.
- [25] I. D. Flintoft, J. F. Dawson, A. C. Marvin, and S. J. Porter, "Development of time-domain surface macromodels from material measurements," *23rd Annual Review of Progress in Applied Computational Electromagnetics*, 2007.
- [26] R. J. Luebbers and K. Kunz, "FDTD modeling of thin impedance sheets," *IEEE transactions on antennas and propagation*, vol. 40, pp. 349–351, 1992.
- [27] K. S. Oh and J. E. Schutt-Aine, "An efficient implementation of surface impedance boundary conditions for the finite-difference time-domain method," *IEEE Transactions on antennas and propagation*, vol. 43, no. 7, pp. 660–666, 1995.
- [28] J. A. Cole, J. F. Dawson, and S. J. Porter, "Efficient modelling of thin conducting sheets within the TLM method," in *1996 Third International Conference on Computation in Electromagnetics (Conf. Publ. No. 420)*, pp. 45–50, April 1996.
- [29] C. W. Penney, R. J. Luebbers, and J. W. Schuster, "Scattering from coated targets using a frequency-dependent, surface impedance boundary condition in FDTD," *IEEE Transactions on Antennas and Propagation*, vol. 44, no. 4, pp. 434–443, 1996.
- [30] J. H. Beggs, "A FDTD surface impedance boundary condition using Z-transforms," *Applied Computational Electromagnetics Society Journal*, vol. 13, pp. 14–24, 1998.
- [31] S. V. den Berghe, F. Olyslager, and D. D. Zutter, "Accurate modeling of thin conducting layers in FDTD," *IEEE Microwave and Guided Wave Letters*, vol. 8, pp. 75–77, Feb 1998.
- [32] M. Karkkainen, "FDTD surface impedance models for electrically thick dispersive material coatings," *Radio Science*, vol. 38, no. 3, 2003.
- [33] Y. Wang and S. Langdon, "FDTD simulation of thin resistive sheets," in *Antennas and Propagation Society International Symposium (APSURSI), 2014 IEEE*, pp. 504–505, IEEE, 2014.

- [34] A. Lauer and I. Wolff, “A conducting sheet model for efficient wide band FDTD analysis of planar waveguides and circuits,” in *Microwave Symposium Digest, 1999 IEEE MTT-S International*, vol. 4, pp. 1589–1592 vol.4, June 1999.
- [35] R. Makinen, “An efficient surface-impedance boundary condition for thin wires of finite conductivity,” *IEEE transactions on antennas and propagation*, vol. 52, no. 12, pp. 3364–3372, 2004.
- [36] M. Feliziani, “Subcell FDTD modeling of field penetration through lossy shields,” *Electromagnetic Compatibility, IEEE Transactions on*, vol. 54, pp. 299–307, April 2012.
- [37] V. Nayyeri, M. Soleimani, and O. Ramahi, “A method to model thin conductive layers in the finite-difference time-domain method,” *Electromagnetic Compatibility, IEEE Transactions on*, vol. 56, pp. 385–392, April 2014.
- [38] Q. Si, L. Shi, Y. Zhou, T. Wang, L. Xiang, and H. Zhengyu, “Application of Z model in FDTD analysis of multi-layer conductivity slabs,” in *Environmental Electromagnetics (CEEM), 2015 7th Asia-Pacific Conference on*, pp. 180–183, Nov 2015.
- [39] M. R. Cabello, L. D. Angulo, J. Alvarez, I. D. Flintoft, S. Bourke, J. F. Dawson, R. G. Martín, and S. G. Garcia, “A hybrid Crank-Nicolson FDTD subgridding boundary condition for lossy thin-layer modeling,” *IEEE Transactions on Microwave Theory and Techniques*, vol. PP, no. 99, pp. 1–10, 2017.
- [40] E. A. Navarro, J. Segura, A. Soriano, and V. Such, “Modeling of thin curved sheets with the curvilinear FDTD,” *IEEE Transactions on Antennas and Propagation*, vol. 52, pp. 342–346, Jan 2004.
- [41] X.-J. Hu and D.-B. Ge, “Study on conformal FDTD for electromagnetic scattering by targets with thin coating,” *Progress In Electromagnetics Research*, vol. 79, pp. 305–319, 2008.
- [42] Y. Xiong, W. Che, and Y. Han, “SIBC incorporated in conformal FDTD to efficiently simulate the thin conductive layer of periodic structure,” *IET Microwaves, Antennas & Propagation*, vol. 10, no. 4, pp. 353–361, 2016.
- [43] C. L. Holloway, M. S. Sarto, and M. Johansson, “Analyzing carbon-fiber composite materials with equivalent-layer models,” *IEEE Transactions on Electromagnetic Compatibility*, vol. 47, pp. 833–844, Nov 2005.

- [44] W. Jianqing, T. Tsuchikawa, and O. Fujiwara, “FDTD simulation of shielding effectiveness of metal-coated plastics for pulsed electromagnetic fields,” *IEICE transactions on communications*, vol. 88, no. 1, pp. 358–363, 2005.
- [45] X. Meng, P. Sewell, A. Vukovic, H. Nasser, and T. Benson, “Embedded carbon fibre composite (CFC) model for arbitrary contour surfaces,” in *Computation in Electromagnetics (CEM 2014), 9th IET International Conference on*, pp. 1–2, March 2014.
- [46] X. Meng, A. Vukovic, T. M. Benson, and P. Sewell, “Extended capability models for carbon fiber composite (CFC) panels in the unstructured transmission line modeling (UTLM) method,” *IEEE Transactions on Electromagnetic Compatibility*, vol. 58, pp. 811–819, June 2016.
- [47] J. G. Maloney and G. S. Smith, “The efficient modeling of thin material sheets in the finite-difference time-domain (FDTD) method,” *IEEE Transactions on Antennas and Propagation*, vol. 40, pp. 323–330, Mar 1992.
- [48] J. G. Maloney and G. S. Smith, “A comparison of methods for modeling electrically thin dielectric and conducting sheets in the finite-difference time-domain (FDTD) method,” *IEEE Transactions on Antennas and Propagation*, vol. 41, pp. 690–694, May 1993.
- [49] G. Kobidze, “Implementation of collocated surface impedance boundary conditions in FDTD,” *IEEE Transactions on Antennas and Propagation*, vol. 58, pp. 2394–2403, July 2010.
- [50] “IEEE recommended practice for validation of computational electromagnetics computer modeling and simulations,” *IEEE Std 1597.2-2010*, pp. 1–124, Feb 2011.
- [51] M. Gaffar and D. Jiao, “On the low-frequency breakdown of FDTD,” in *2015 IEEE International Symposium on Antennas and Propagation USNC/URSI National Radio Science Meeting*, pp. 338–339, July 2015.
- [52] A. C. Cangellaris and D. B. Wright, “Analysis of the numerical error caused by the stair-stepped approximation of a conducting boundary in FDTD simulations of electromagnetic phenomena,” *IEEE Transactions on Antennas and Propagation*, vol. 39, pp. 1518–1525, Oct 1991.
- [53] A. Akyurtlu, D. H. Werner, V. Veremey, D. J. Steich, and K. Aydin, “Staircasing errors in FDTD at an air-dielectric interface,” *IEEE Microwave and Guided Wave Letters*, vol. 9, pp. 444–446, Nov 1999.

- [54] R. Holland, "Pitfalls of staircase meshing," *IEEE Transactions on Electromagnetic Compatibility*, vol. 35, pp. 434–439, Nov 1993.
- [55] P. H. Harms, J. F. Lee, and R. Mittra, "A study of the nonorthogonal FDTD method versus the conventional FDTD technique for computing resonant frequencies of cylindrical cavities," *IEEE Transactions on Microwave Theory and Techniques*, vol. 40, pp. 741–746, Apr 1992.
- [56] K. L. Shlager and J. Maloney, "Limitations on using the staircased FDTD method when modeling narrow-angled TEM horn antennas," in *Antennas and Propagation Society International Symposium, 1996. AP-S. Digest*, vol. 2, pp. 1280–1283, IEEE, 1996.
- [57] J. B. Schneider and K. L. Shlager, "FDTD simulations of TEM horns and the implications for staircased representations," *IEEE Transactions on Antennas and Propagation*, vol. 45, pp. 1830–1838, Dec 1997.
- [58] S. Schild, N. Chavannes, and N. Kuster, "A robust method to accurately treat arbitrarily curved 3-D thin conductive sheets in FDTD," *IEEE Transactions on Antennas and Propagation*, vol. 55, no. 12, pp. 3587–3594, 2007.
- [59] M. K. Berens, I. D. Flintoft, and J. F. Dawson, "Structured mesh generation: Open-source automatic nonuniform mesh generation for FDTD simulation.," *IEEE Antennas and Propagation Magazine*, vol. 58, pp. 45–55, June 2016.
- [60] S. Dey and R. Mittra, "A modified locally conformal finite-difference time-domain algorithm for modeling three-dimensional perfectly conducting objects," *Microwave and Optical Technology Letters*, vol. 17, no. 6, pp. 349–352, 1998.
- [61] S. Dey and R. Mittra, "A conformal finite-difference time-domain technique for modeling cylindrical dielectric resonators," *IEEE Transactions on Microwave Theory and Techniques*, vol. 47, pp. 1737–1739, Sept 1999.
- [62] W. Yu and R. Mittra, "A conformal finite difference time domain technique for modeling curved dielectric surfaces," *IEEE Microwave and Wireless Components Letters*, vol. 11, pp. 25–27, Jan 2001.
- [63] T. G. Jurgens, A. Taflove, K. Umashankar, and T. G. Moore, "Finite-difference time-domain modeling of curved surfaces," *IEEE Transactions on Antennas and Propagation*, vol. 40, pp. 357–366, Apr 1992.

- [64] N. Kaneda, B. Houshmand, and T. Itoh, "FDTD analysis of dielectric resonators with curved surfaces," *IEEE Transactions on Microwave Theory and Techniques*, vol. 45, pp. 1645–1649, Sept 1997.
- [65] K. Naishadham and Z. Lin, "FDTD method with a conformal polygonal mesh and perfectly matched layer absorbing boundary condition," in *Microwave Symposium Digest, 1997., IEEE MTT-S International*, vol. 3, pp. 1543–1546 vol.3, June 1997.
- [66] T. I. Kosmanis and T. D. Tsiboukis, "A systematic conformal finite-difference time-domain (FDTD) technique for the simulation of arbitrarily curved interfaces between dielectrics," *IEEE Transactions on Magnetics*, vol. 38, pp. 645–648, Mar 2002.
- [67] R. M. Makinen, H. D. Gersem, T. Weiland, and M. A. Kivikoski, "Modeling of lossy curved surfaces in 3-D FIT/FDTD techniques," *IEEE Transactions on Antennas and Propagation*, vol. 54, pp. 3490–3498, Nov 2006.
- [68] T. G. Jurgens and A. Taflove, "Three-dimensional contour FDTD modeling of scattering from single and multiple bodies," *IEEE Transactions on Antennas and Propagation*, vol. 41, pp. 1703–1708, Dec 1993.
- [69] T. Su, Y. Liu, W. Yu, and R. Mittra, "A conformal mesh-generating technique for the conformal finite-difference time-domain (cfddd) method," *IEEE Antennas and Propagation Magazine*, vol. 46, pp. 37–49, Feb 2004.
- [70] S. Dey and R. Mittra, "A locally conformal finite-difference time-domain (FDTD) algorithm for modeling three-dimensional perfectly conducting objects," *IEEE Microwave and Guided Wave Letters*, vol. 7, pp. 273–275, Sep 1997.
- [71] T. Xiao and Q. H. Liu, "A 3-D enlarged cell technique (ECT) for the conformal FDTD method," *IEEE Transactions on Antennas and Propagation*, vol. 56, no. 3, pp. 765–773, 2008.
- [72] G. Junkin, "Conformal FDTD modeling of imperfect conductors at millimeter wave bands," *IEEE Transactions on Antennas and Propagation*, vol. 59, pp. 199–205, Jan 2011.
- [73] W. Yu and R. Mittra, "A conformal FDTD software package modeling antennas and microstrip circuit components," *IEEE Antennas and Propagation Magazine*, vol. 42, pp. 28–39, Oct 2000.

- [74] S. Benkler, N. Chavannes, and N. Kuster, “A new 3-D conformal PEC FDTD scheme with user-defined geometric precision and derived stability criterion,” *IEEE Transactions on Antennas and Propagation*, vol. 54, pp. 1843–1849, June 2006.
- [75] J. A. Stratton, *Electromagnetic Theory*. New York: McGraw-Hill, 1941.
- [76] S. Benkler, N. Chavannes, and N. Kuster, “Mastering conformal meshing for complex CAD-based C-FDTD simulations,” *IEEE Antennas and Propagation Magazine*, vol. 50, pp. 45–57, April 2008.
- [77] X. Ai, Y. Tian, Z. Cui, Y. Han, and X.-W. Shi, “A dispersive conformal FDTD technique for accurate modeling electromagnetic scattering of THz waves by inhomogeneous plasma cylinder array,” *Progress In Electromagnetics Research*, vol. 142, pp. 353–368, 2013.
- [78] Y. Wang and S. Langdon, “A conformal scheme for simulation of thin good conducting objects in FDTD,” in *Antennas and Propagation Society International Symposium, 2009. APSURSI’09. IEEE*, pp. 1–4, IEEE, 2009.
- [79] S. A. Bourke, J. F. Dawson, I. D. Flintoft, and M. P. Robinson, “Errors in the shielding effectiveness of cavities due to stair-cased meshing in FDTD: Application of empirical correction factors,” in *2017 International Symposium on Electromagnetic Compatibility - EMC EUROPE*, pp. 1–6, Sept 2017.
- [80] G. Waldschmidt and A. Taflove, “Three-dimensional CAD-based mesh generator for the Dey-Mittra conformal FDTD algorithm,” *IEEE Transactions on Antennas and Propagation*, vol. 52, no. 7, pp. 1658–1664, 2004.
- [81] G. Junkin and J. Parron, “A robust 3D mesh generator for the Dey-Mittra conformal FDTD algorithm,” in *The Second European Conference on Antennas and Propagation, EuCAP 2007*, pp. 1–6, Nov 2007.
- [82] I. Zagorodnov, R. Schuhmann, and T. Weiland, “A uniformly stable conformal FDTD-method in Cartesian grids,” *International Journal of Numerical Modelling: Electronic Networks, Devices and Fields*, vol. 16, no. 2, pp. 127–141, 2003.
- [83] I. Zagorodnov, R. Schuhmann, and T. Weiland, “Conformal FDTD-methods to avoid time step reduction with and without cell enlargement,” *Journal of Computational Physics*, vol. 225, no. 2, pp. 1493–1507, 2007.
- [84] M. R. Cabello, L. D. Angulo, J. Alvarez, A. R. Bretones, G. G. Gutierrez, and S. G.

Garcia, “A new efficient and stable 3D conformal FDTD,” *IEEE Microwave and Wireless Components Letters*, vol. 26, pp. 553–555, Aug 2016.

- [85] C. Geuzaine and J.-F. Remacle, “Gmsh: A 3-D finite element mesh generator with built-in pre- and post-processing facilities,” *International Journal for Numerical Methods in Engineering*, vol. 79, pp. 1309–1331, Sep 2009.